E.O. Paton Electric Welding Institute of the National Academy of Sciences of Ukraine

International Scientific-Technical and Production Journal

The Paton WELDING JOURNAL

March 2014
No.3

Published since 2000

English translation of the monthly «Avtomaticheskaya Svarka» (Automatic Welding) journal published in Russian since 1948

Editor-in-Chief B.E.Paton

EDITORIAL BOARD

Yu.S. Borisov,
B.V. Khitrovskaya (*exec. secretary*),
V.F. Khorunov, V.V. Knysh, I.V. Krivtsun,
S.I. Kuchuk-Yatsenko (*vice-chief editor*),
Yu.N. Lankin, V.N. Lipodaev (*vice-chief editor*),
L.M. Lobanov, A.A. Mazur,
O.K. Nazarenko, I.K. Pokhodnya,
V.D. Poznyakov, I.A. Ryabtsev,
K.A. Yushchenko,
A.T. Zelnichenko (*exec. director*)
(*Editorial Board Includes PWI Scientists*)

INTERNATIONAL EDITORIAL COUNCIL

N.P. Alyoshin
N.E. Bauman MSTU, Moscow, Russia
V.G. Fartushny
Welding Society of Ukraine, Kiev, Ukraine
Guan Qiao
Beijing Aeronautical Institute, China
V.I. Lysak
Volgograd State Technical University, Russia
B.E. Paton
PWI, Kiev, Ukraine
Ya. Pilarczyk
Weiding Institute, Gliwice, Poland
U. Reisgen
Welding and Joining Institute, Aachen, Germany
O.I. Steklov
Welding Society, Moscow, Russia
G.A. Turichin
St.-Petersburg State Polytechn. Univ., Russia
M. Zinigrad
College of Judea & Samaria, Ariel, Israel
A.S. Zubchenko
OKB «Gidropress», Podolsk, Russia

Founders
E.O. Paton Electric Welding Institute
of the NAS of Ukraine,
International Association «Welding»

Publisher
International Association «Welding»

Translators
A.A. Fomin, O.S. Kurochko,
I.N. Kutianova
Editor
N.A. Dmitrieva
Electron galley
D.I. Sereda, T.Yu. Snegiryova

Address
E.O. Paton Electric Welding Institute,
International Association «Welding»
11, Bozhenko Str., 03680, Kyiv, Ukraine
Tel.: (38044) 200 60 16, 200 82 77
Fax: (38044) 200 82 77, 200 81 45
E-mail: journal@paton.kiev.ua
www.patonpublishinghouse.com

State Registration Certificate
KV 4790 of 09.01.2001
ISSN 0957-798X

Subscriptions
$348, 12 issues per year,
air postage and packaging included.
Back issues available.

All rights reserved.
This publication and each of the articles contained herein are protected by copyright.
Permission to reproduce material contained in this journal must be obtained in writing from the Publisher.

CONTENTS

SCIENTIFIC AND TECHNICAL

Ermolenko D.Yu. and *Golovko V.V.* Numerical modeling and prediction of weld microstructure in high-strength steel welding (Review) 2

Polishko A.A., Saenko V.Ya., Tunik A.Yu. and *Stepanyuk S.N.* Structure of surface-melted zone of cast high-nickel alloy KhN56MBYuDSh after laser surface treatment 11

Bondarev A.A. and *Nesterenkov V.M.* Technological peculiarities of welding of wrought magnesium alloys by electron beam in vacuum 16

Bachmann M., Avilov V., Gumenyuk A. and *Rethmeier M.* High-power laser welding of austenitic stainless steel with electromagnetic control of weld pool 21

Borisov Yu.S., Borisova A.L., Astakhov E.A., Burlachenko A.N., Ipatova Z.G. and *Gorban V.F.* Detonation coatings of composite powder of ferromolybdenum–silicon carbide produced using method of mechanical-and-chemical synthesis 25

INDUSTRIAL

Makhnenko O.V., Saprykina G.Yu., Mirzov I.V. and *Pustovoj A.D.* Prospects for development of load-carrying elements of freight car bogie 33

Antipov Yu.N., Dmitrenko E.V., Kovalenko A.V., Goryanoj S.A., Rybakov A.A., Semyonov S.E. and *Filipchuk T.N.* Technology for manufacture of gas-and-oil line pipes using high-frequency method of welding at Company «Interpipe NMPP» 39

Chvertko P.N., Goronkov N.D., Vinogradov N.A., Samotryasov S.M. and *Sysoev V.Yu.* Resistance butt welding of concrete reinforcement in construction site 45

Rybakov A.A., Goncharenko L.V., Filipchuk T.N., Lokhman I.V. and *Burak I.Z.* Reasons of stress corrosion failure of erection girth joint of main gas pipeline 49

© PWI, International Association «Welding», 2014

NUMERICAL MODELING AND PREDICTION OF WELD MICROSTRUCTURE IN HIGH-STRENGTH STEEL WELDING (REVIEW)

D.Yu. ERMOLENKO and **V.V. GOLOVKO**
E.O. Paton Electric Welding Institute, NASU
11 Bozhenko Str., 03680, Kiev, Ukraine. E-mail: office@paton.kiev.ua

Analysis of state-of-the-art of problems of numerical modeling and prediction of weld metal microstructure in high-strength low-alloyed steels was performed. Modern approaches to computer modeling of weld microstructure are analyzed from the viewpoint of prediction of weld metal microstructure and properties, taking into account the influence of nonmetallic inclusions on them. General principles of the problem of modeling the process of formation and evolution of nonmetallic inclusions in the weld metal are considered. Thermodynamic approach to prediction of weld metal microstructure and its drawbacks are presented. Features of modeling the process of metal solidification in the weld pool have been analyzed. Theoretical models of dendrite growth by Ivantsov and KGT-theory are noted; limitations of analytical modeling are described. Critical analysis of numerical models of dendrite solidification has been performed. A conclusion was made that the most adequate and experimentally substantiated results of dendrite growth modeling, allowing for nonmetallic inclusion influence, are to be expected from the method of cellular automation, which should be modified allowing for the capabilities of analytical and numerical models. Such an approach is based to computational simplicity and no need for determination of a number of physical constants for real materials. 53 Ref., 3 Figures.

Keywords: *weld, microstructure, primary structure, dendrites, nonmetallic inclusions, numerical modeling, microstructure prediction*

The main objective in selection of welding technology and welding consumables is the ability to influence weld metal microstructure formation through selection of the welding process, variation of its parameters and weld metal composition [1, 2].

Process of formation of weld metal microstructure is of a pronounced hereditary nature. Secondary microstructure which ensures higher values of weld performance, inherits certain parameters of primary structure, forming as a result of epitaxial growth of dendrites.

Let us consider a schematic (Figure 1), which generalizes modern trends in modeling weld metal structure formation [3, 4]. Modeling of the process of formation of welded joint metal structure is divided into two main groups — macro- and micromodeling.

Let us briefly consider currently available models, describing the influence of each of these factors on structure formation on microlevel.

Models of nonmetallic inclusion formation. Inclusions form in welds as a result of interaction of dissolved aluminium, titanium, silicon and manganese with oxygen, nitrogen, carbon and sulphur. Inclusions are characterized by the volume fraction, size, composition, morphology and type of compounds on the surface that affects further solid-phase transformation. For instance, inclusions, containing a large amount of titanium in the surface layer, promote formation of acicular ferrite [5, 6].

In work [7] K.C. Hseih described the thermodynamics of nonmetallic inclusion formation in the temperature range from 2300 to 1800 K and showed that both simple and complex oxides form at different temperatures. A similar approach was used also in [8] by T. Koseki. The model describing the kinetics of reaction of simultaneous formation of oxides, according to which the oxide content, their morphology and formation temperature change, depending on the composition of molten weld metal, is given in [9, 10].

These data allow for the features of nonmetallic inclusion formation, but do not in any way take into account their influence, either on solidification front movement in the weld pool, or on the morphology and dimensions of weld metal components.

Thermodynamic and kinetic models based on phase diagrams. Such models are based on the method of CALculation of PHAse Diagrams (CALPHAD) [11]. CALPHAD technique allows using an extensive base of accessible thermochemical data (thermodynamic and phase equilibrium data) to select model parameters and de-

© D.Yu. ERMOLENKO and V.V. GOLOVKO, 2014

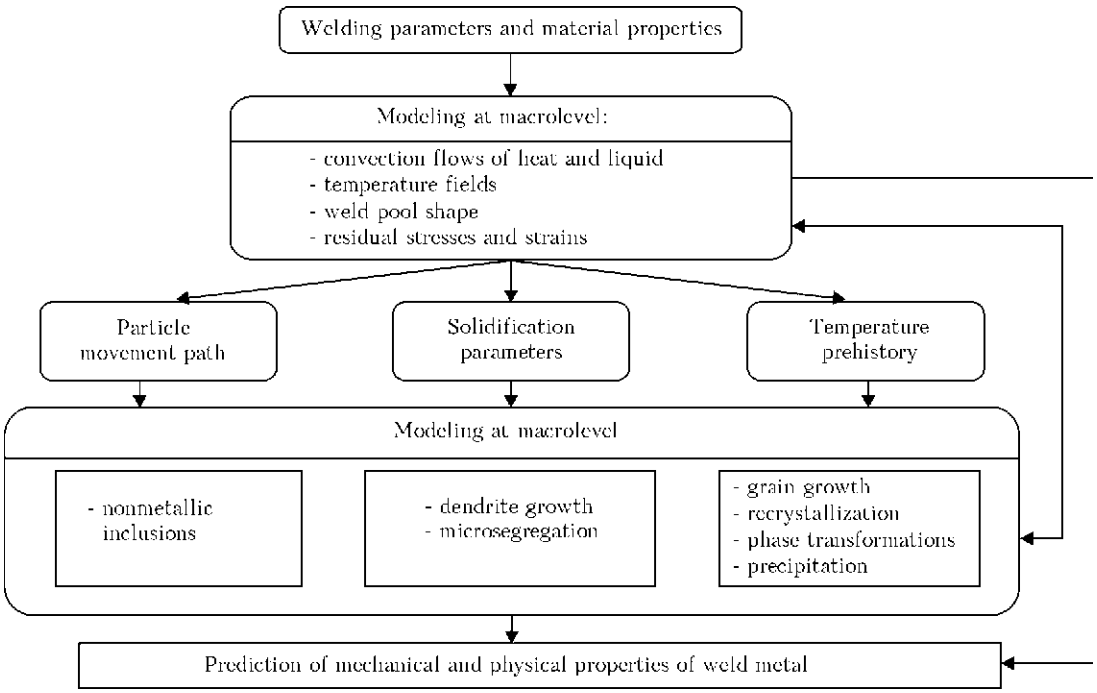

Figure 1. Schematic of weld metal structure modeling

scribe Gibbs energy of individual crystallographic phases. Gibbs energy of each phase is described by the respective thermodynamic model and depends on physical and chemical properties of the phase. These Gibbs energy functions, allowing for composition and temperature dependence, were derived by critical assessment of binary and ternary diagrams, and then were precised, using Thermo-Calc software [12]. The main disadvantage of thermodynamic models is the impossibility of allowing for process kinetics that is quite urgent in the case of weld solidification.

Kinetic models, based on diffusion-controlled growth, can be integrated with thermodynamic models to obtain valuable data on microstructural evolution [13]. They can be used to calculate the influence of cooling rate on final weld microstructure.

Models of this type can be used only in the case of availability of certain phase diagrams in the data base. Construction of new diagrams requires a large scope of experimental work. Moreover, these models cannot allow for the influence of nonmetallic inclusions on formation of microstructural components.

Modeling solid-phase transformations during cooling. Final weld microstructure forms as a result of solid-phase transformations at metal cooling from solidus to room temperature.

The best known tools were developed by A. Schaeffler and modified in the form of WRC-1992-diagrams. In the following years new methods were developed. One of them [14] is based on comparison of thermodynamic stability of ferrite and austenite and is comparable to WRC-1992-diagrams in terms of accuracy, although it can be applied to a broader alloy range. 40 % more accurate results that those of WRC-1992-diagrams are given by an approach based on neural network [15].

In the case of low-alloyed steels, weld microstructure can be predicted using Bhadeshia models, considered in [16]. They, however, do not take into account the hereditary nature of formation of final weld microstructure, as they consider only austenite grain transformation. HAZ metal structure can be modeled using Ashby model [17], complementing the classical works by N. Yurioka [18].

These models are capable of prediction of quantitative ratio of phases in the weld metal final structure, proceeding from the composition and cooling rate of weld metal, but do not provide any information on the influence of nonmetallic inclusions on the process of its formation. In order to exactly understand weld metal structure evolution during cooling and determine the influence of inclusions on primary solidification front movement, it is necessary to consider weld pool metal solidification as a process of liquid phase transition into solid phase.

Metal solidification in the weld pool. Conditions of metal solidification determine the structure, homogeneity and strength of cast products as a whole. Knowledge of solidification processes in regular metal casting is directly related to fusion welding processes, which can be regarded as «casting in miniature» [19].

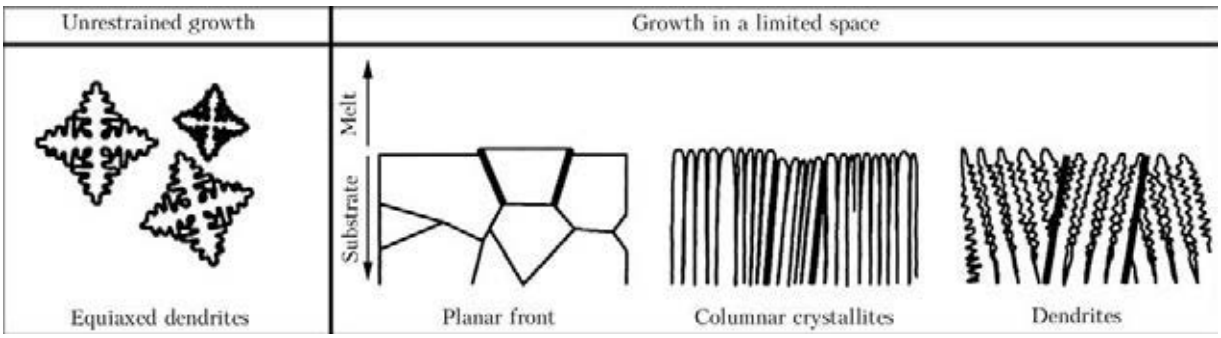

Figure 2. Possible solidification morphologies of weld metal [20]

Process of metal solidification in the weld pool controls grain size and shape, weld defectiveness (porosity and hot cracks). There is some similarity between ingot crystallization and weld pool solidification, but modeling melt solidification in the weld zone is made more complicated by such factors as [1]:

- dynamic nature of the welding process;
- indeterminateness of weld pool shape;
- epitaxial growth (crystal growth on the substrate and, consequently, inheriting the substrate crystallographic orientation);
- change of temperature gradient and rate in different portions of weld pool.

At alloy solidification, two variants of solidification are possible depending on cooling rate, which differ by the method of heat removal from solidification surface [20]:

- unrestrained growth in overcooled melt; in such a case equiaxed dendrites mostly form;
- directional solidification or growth in a limited space; in such a case, flat, columnar or dendritic structures mostly form (Figure 2).

In the weld pool solidification proceeds from the already existing solid substrate and, therefore, formation of new nuclei is minor and negligible. Modifiers and dynamic methods, such as melt mixing in the weld pool and welding arc oscillations, are used to control nucleus growth. To describe the influence of these factors, heat and mass transfer models should be related to probabilistic models, such as cell automation or deterministic models with application of fundamental nucleation equations [9].

Microstructure formation during nucleus growth is controlled by the processes on the solid and liquid interface. Stability of this interface is determined by thermal conditions and chemical composition in the immediate vicinity of the interface. Depending on these conditions, linear, cellular (honeycomb) or dendritic crystal growth can proceed. Crystal growth in the heat flow direction is beneficial in terms of energy, that should be taken into account at prediction of weld metal microstructure [21].

As dendrite growth in the heat flow direction is the main mechanism of solidification in steel welding [20], it is rational to consider the models, describing exactly this process and possibilities of these models.

Dendrite growth simulation. Solidification process modeling is important for understanding phase transition phenomena that is why theoretical analysis and modeling of these processes have attracted scientists' attention for many decades. Considerable progress has been achieved in theoretical analysis of dendrite growth, as shown in the work by R. Trivedi and W. Kurz [22].

Most analytical models consider stationary growth of an isolated dendrite in the assumption that all the dendrites preserve the same shape. In this case the dendrite tip is considered to be a paraboloid of revolution [23].

At application of numerical methods to solve the problem of diffusion around the dendrites or a cellular dendrite tip, the assumption of a needle-like shape can be omitted, and it is also possible to take into account surface tension anisotropy on the liquid and solid interface [24].

At application of modern modeling methods, such as cell automation [25, 26] and phase fields [27], solidification morphologies can be modeled without any special assumptions of dendrite or cell shape.

Let us consider this subject in greater detail.

Dendrite stability. In [28] T. Koseki, based on theoretical analysis, showed that dendrites or cells form during solidification in a broad range of fusion welding conditions.

Dendrite structures form as a result of planar interface instability during solidification. Earlier, this phenomenon was explained by overcooling theory of W.A. Tiller and co-authors [29] and disturbance theory of W.W. Mullins and R.F. Sekerka [30]. At alloy solidification in planar interface mode, the region of overcooled melt ahead of this interface forms due to solute tran-

sition from the solid state into the liquid phase. With increase of solute content, alloy melting temperature drops. Thus, if a disturbance appears on the solid and liquid interface, it can develop into a dendrite, the tip of which repulses the solute not only normal to solidification front, but also to the sides. In this connection, overcooling becomes smaller, compared to overcooling for planar interface. Theory of disturbances yields the lower and upper thresholds for solidification rate:

$$v_s^{min} = \frac{GD_l}{\Delta T_0}, \quad (1)$$

$$v_s^{max} = \frac{\Delta T_0 D_l}{k\Gamma_k}, \quad (2)$$

where G is the temperature gradient in liquid on the interface; D_l is the coefficient of diffusion of the dissolved component in the melt; ΔT_0 is the equilibrium cooling range; k is the equilibrium coefficient of solute distribution; Γ_k is the Gibbs–Thomson coefficient.

For interstitial solutions such as alloys of Fe–C system, at temperature gradient $G = 2 \cdot 10^4$ °C/m typical for welding, threshold values of solidification rate can be calculated, proceeding from equations (1) and (2), being equal to $v_s^{min} = 10^{-5}$ and $v_s^{max} = 20$ m/s for steels. Thus, planar solidification mode is possible in welding, if the solidification rate is extremely low (of the order of μm/s), or extremely high (of the order of m/s). In most of the cases in practice, however, solidification rate is in the range of $v_s^{min} - v_s^{max}$. Initial solidification zone, located on the surface of weld pool contact with base metal, where solidification rate starts from zero, is an exception. Upper threshold of solidification rate is not achieved at regular fusion welding, as at increase of welding speed the weld pool takes the shape of a drop, and maximum solidification rate becomes close to a limited value, which is always smaller than the welding speed.

The above theoretical analysis of stability of planar solidification front shows that in welding of steels, solidification proceeds in the weld pool in the form of dendrites or cells. This emphasizes the importance of investigation and modeling of this kind of structures for understanding the welding phenomena.

Analytical models. *Ivantsov's solution*. The first sequential solution of the problem of diffusion around an isolated needle tip as that of crystal growth in an overcooled melt was published in [31] by G.P. Ivantsov. Isothermal surface around the dendrite tip was presented as joint paraboloid of revolution. Dendrite tip has the shape of paraboloid of revolution, as this corresponds to solid–liquid interface, which is considered to be isothermal. Analytical expression, connecting the radius of dendrite rounding-off R_t and growth rate v_t with dendrite tip temperature T_t presented in [31], is given in the following equation:

$$T_t - T_\infty = \frac{\Delta H}{C_m} Iv(\mathrm{Pe}_t);$$
$$Iv(\mathrm{Pe}_t) = \mathrm{Pe}_t \exp(\mathrm{Pe}_t) Ei(\mathrm{Pe}_t); \quad \mathrm{Pe}_t = \frac{v_t R_t}{2\alpha}, \quad (3)$$

where T_∞ is the melt temperature in the infinity; ΔH is the melting enthalpy; C_m is the melt heat capacity; Iv is the Ivantsov's function; Pe_t is the Peclet heat number; Ei is the integral exponential function; α is the thermodiffusion coefficient.

Having applied the analogy between thermal diffusion and solute diffusion, provided the dendrite tip composition is constant, a similar expression can be derived for concentrational dendrites:

$$C_t - C_0 = C_t(1 - k)Iv(\mathrm{Pe}); \quad \mathrm{Pe} = \frac{v_t R_t}{2D_l}, \quad (4)$$

where C_0 is the nominal composition of binary alloy; Pe is the Peclet concentration number.

For the specified temperature of the tip or its composition, the model predicts only the value of Peclet number or $v_t R_t$ product. It means that several variants of solution are possible for dendrites with tip radius inversely proportional to solidification rate.

In the case of limited directional solidification, the dendrite tip temperature is controlled by solute diffusion. Assuming that the phase diagram is linear, overcooling in the tip can be expressed by the formula

$$\Delta T_t = -m(C_t - C_0), \quad (5)$$

where m is the inclination of liquidus line.

Substituting value C_t from equation (4) and allowing for the following relationship for equilibrium melting range $\Delta T_0 = T_t - T_s = mC_0 (1 - k)/k$, overcooling at dendrite tip can be written as

$$\Delta T_t = \frac{k\Delta T_0 Iv(\mathrm{Pe})}{1 - (1 - k)Iv(\mathrm{Pe})}. \quad (6)$$

If the solidification rate is determined by the process (for instance, type of heat source in welding), several solutions are available to determine overcooling at the dendrite tip. Thus, additional

limitation is required to select a unique rounding-off radius of the dendrite from the multitude of possible solutions, predicted by Ivantsov's model.

Taking into account the influence of interphacial energy, equation (6) is modified into (7), which connects Ivantsov's model and stabilizing capillarity effect:

$$\Delta T_t = \frac{k\Delta T_0 Iv(\mathrm{Pe})}{1-(1-k)Iv(\mathrm{Pe})} + \frac{2\Gamma_k}{R_t}. \quad (7)$$

As Ivantsov's model is valid only for isothermal surfaces, and the capillarity effect is manifested only along nonisothermal surface, modifications of this model are only approximate. More detailed solutions for nonisothermal interfaces were suggested in [32, 33]. Addition of the capillarity term makes unstable only a very small area of solutions, but it does not eliminate the multiplicity of results predicted by Ivantsov's model. An additional limitation is required to allow the system to select a unique value of dendrite tip radius. As the ratio of rate and radii is of extreme nature, it was proved that selection of dendrite tip radius occurs at extreme value, which corresponds to maximum growth rate at a given overcooling or minimum overcooling at a given growth rate. It should be noted that experimental results, given in [34] by H.C. Huang and M.E. Glicksman, cast doubt on this assumption.

KGT-theory. Authors of work [35] J.S. Langer and H. Muller-Krumbhaar suggested replacing the maximum rate principle by form stability criterion $v_t R_t^2 = \text{const}$. They found that massive dendrites have an unstable tip, while those which are too narrow and rapidly growing, are, as a rule, slowed down, because of side branching instability. At present this is the most popular criterion of selection, called «limit stability». Proceeding from this concept, authors of [23, 36] developed a theoretical model for directional solidification, known as KGT-model. Assuming that dendrite tip radius in the stationary state is equal to critical wave length of unstable solid-liquid interface ($R_t = \lambda_s$) and using Ivantsov's solution for transportation problem, equations (8)–(11) were derived for the criterion of selection of dendrite tip parameters:

$$Av_t^2 - Bv_t + G = 0, \quad (8)$$

$$A = \frac{\Gamma_k}{4\sigma^* \mathrm{Pe}^2 D_l^2}, \quad (9)$$

$$B = \frac{k\Delta T_0}{1-(1-k)Iv(\mathrm{Pe})}\frac{\xi}{D_l}, \quad (10)$$

$$\xi = 1 - \frac{2k}{\left(1+\frac{1}{\sigma^* \mathrm{Pe}^2}\right)^{0.5} - 1 + 2k}, \quad (11)$$

where σ^* is the stability constant, which is determined experimentally.

If we consider the critical wave length of unstable interface at dendrite tip λ_s, then for it to correspond to planar interface, theoretical value of σ^* should be equal to $1/4\pi^2 = 0.0253$. Experimental values for different binary systems, which vary about value 0.02 [26], are in good agreement with this value.

For the specified value of solidification rate v_t, Peclet number Pe can be found by numerical solution of equation (8). Value of rounding-off radius R_t is derived from the expression for Pe (4). Using values Pe and R_t, overcooling at dendrite tip and, therefore, temperature T_t can be calculated from equation (7), and composition at dendrite tip can be given by equation (4). Thus, the data, provided by KGT-model, can be used for comparison with predictions from other models, including variants of direct modeling of solidification.

KGT-model can be also used for calculation of dendrite growth kinetics through cell automation and virtual grain models, developed for direct modeling of grain structure formation in castings [37] and in welding [38].

Analytical modeling limitations. Above-described and similar [36] analytical models were focused on isolated dendrites, which grow either in overcooled melt, or in the melt with positive temperature gradient in constrained conditions of solidification. Problem of solidification with a free interface is extremely complex, and above-described models are just an approximation to physical interpretation of the problem, in order to obtain a stable analytical solution. Their limitations consist in growth of dendrite bulk, in which diffusion fields of adjacent dendrites interact with each other. This is particularly evident in the impossibility of prediction of dendrite trunk spacing [39]. In addition, the above-considered analytical models do not describe the instability of dendrite tip, and, therefore, the development of dendrite secondary branches.

Numerical models. *McCartney and Hunt models*. Authors of work [24, 39] developed a theoretical model of stable growth of cell or dendrite bulk at positive temperature gradient using finite element methods. They proceeded from the

fact that the problem with free interface and solid–liquid interface implies both phases being in equilibrium, as well as fulfillment of an additional condition of equilibrium on solid–liquid interface. This condition pertains to interface temperature T_i and its composition C_l, and curvature and kinetic mobility:

$$T_i = T_M + m(C_l - C_0) - \Gamma_k k - \frac{v}{\mu_v}, \qquad (12)$$

where v is the normal speed of interface movement; μ_v is the kinetic coefficient.

This numerical model eliminates the needle shape assumption. Moreover, diffusion of heat and solute are considered simultaneously. Thus, the model is capable of realistic predictions.

Derived numerical results point to a minimum of tip overcooling, depending on the half-width of an elementary cell. Form self-consistency can be found only under certain growth conditions [24], and only up to a certain maximum value of half-width. Assuming that the growth proceeds between minimum overcooling at the tip and point of instability, numerical results are in agreement with the respective experimental data. Here, no self-consistent form exists above a certain growth rate that makes application of this method impossible at transition from cellular to dendritic morphology with well-developed side branching, which cannot be modeled by this method.

Analysis by Hunt and Lu, interdentritic spacing and structure prediction. Using a modified variant of the above numerical model, J.D. Hunt and S.L. Lu [40] studied the mechanisms of spacing adjustment in the growing bulk of cells or dendrites. In order to make the analysis simpler and faster, they eliminated solution of heat conductivity equation. Instead, heat flow was described by introducing a moving linear temperature field, which varies only in the axial direction. In addition, a very simple model was developed for several cells, which studies the interactions of a central cell with six surrounding cells. This model was the basis to propose a criterion of selection of minimum distance to a stable cell. One of the most important model results is that it predicts a small range of distances to a stable cell and a separate range for dendrites.

The above results are generalized in [41], where numerical data in a dimensionless form were provided with analytical expressions for determination of concentratal overcooling and overcooling due to surface curvature («curvature under cooling») on the interface both for cellular solidification mechanism and for the dendritic one. Formulas, given in this work, are in good agreement with experiments and other models, as they represent dependencies of primary dendrite spacing, as well as overcooling at the tips for cells and dendrites bulk, depending on solidification parameters (rate, temperature gradient and material properties).

Spatial (direct) modeling methods. Direct modeling methods imply modeling of the entire dendrite structure or its significant part. For this purpose the solid and liquid phase evolution should be calculated in space and time. This can be implemented by explicit tracing of the interface, or implicitly, both in cell automation or in phase field model, which are described below.

Cellular automation. Brown model. Over the last two decades cellular automation was used for modeling various phase transformations in materials [42, 43]. This simulation method uses a regular grid, which is divided into cells of equal size, as a rule these are square in 2D and cubes in 3D. Each cell is characterized by its state, for instance, liquid phase, solid phase, phase 1, phase 2, etc. A cell can also contain one or several variables, for instance, values of temperature and/or composition. Applying the transition rules, a cell can change its state iteratively in time («stepping»). Transition rules allow for the state of the cell proper, its neighbours and their variables. This is a very simple method to study system evolutions in response to process parameters and variables. Theoretical and practical importance of application of cellular automation model for simulation of solidification phenomenon was considered in the works by S.G.R. Brown and J.A. Spittle [42], and Ch.-A. Gandin and M. Rappaz [37].

Illustration of application of cellurar automation modeling to simulate dendrite morphologies and growth kinetics was presented in [25]. The authors calculate unrestrained growth of non-isothermal dendrites in overcooled melts for single-component systems. The model includes rules to allow for thermal diffusion, curvature impact on equilibrium solidification temperature and latent heat evolution. Predicted growth kinetics is in good agreement with the known experimental and theoretical results. However, as quantitative physics of the process is practically not included into the model, this model allows only a qualitative study of the factors determining dendrite development in overcooled melts.

Sasikumar–Sreenivasan model. Work [26] presents a 2D-model of dendrite growth in a single-component system with elements of cell automation method, similar to S.G.R. Brown model

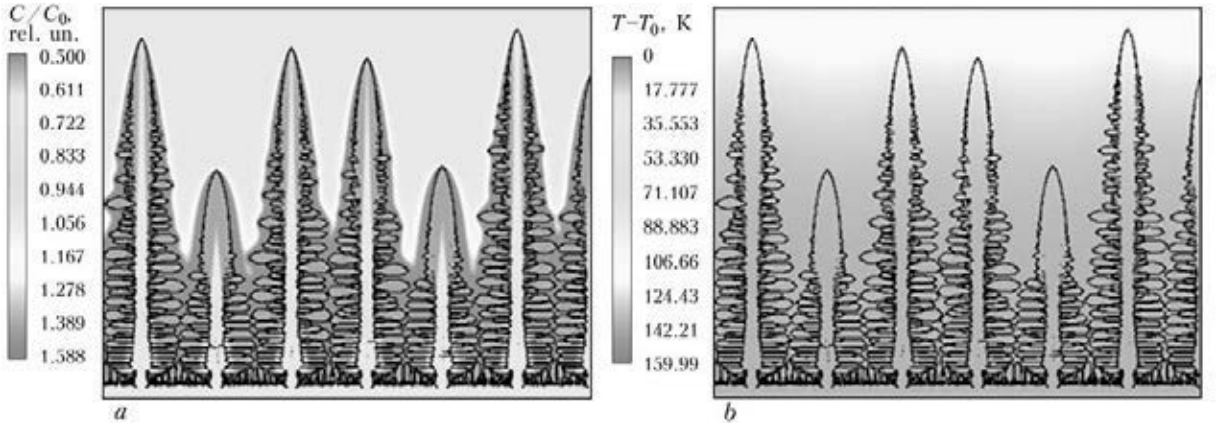

Figure 3. Result of modeling oriented dendrite growth in overcooled Fe–C melt [49]: *a* — concentration distribution C/C_0; *b* — temperature distribution $T–T_0$

described above, but expanded with finite element method to solve heat conductivity equations. Thus, Sasikumar–Sreenivasan model is a combination of physical and empirical approaches, i.e. moving force of dendrite growth is calculated on the basis of realistic physical model, whereas empirical rules, introduced into this method, are used to allow for surface curvature, growth anisotropy and noise. One cannot expect that the model will yield quantitatively correct results, but it can be used to study the tendencies in dendrite morphology variation, depending on material properties and process parameters.

In more recent studies this model was modified to illustrate particle influence on dendrite morphology [44] and for modeling in binary alloys [45].

Results of Galenko and Krivilev. This approach was used in [46–49] and showed adequate results in modeling dendrite growth (Figure 3) both at low rates of crystal growth (diffusion-limited solidification), and for high-rate growth (diffusion-limited and kinetically controlled solidification). Moreover, work [46] gives a number of results for various alloys (Fe–C, Cu–Ni, Ni–B, Ag–Cu).

Phase field method. Over the last years, the popularity of phase field method has been rapidly rising [27, 50, 51]. The method is based on fundamental physical principles from thermodynamics and kinetics, and is widely applied for modeling a wide range of phase transition problem. The main principles of the method and its application to solidification problem can be described on the basis of [27], in which Steinbach model [52] was adapted for phase transformations in steels, in particular, for growth of dendrites with peritectic reaction, grain growth and allotriomorphous formation of ferrite.

Phase field method rejects the paradigm of a clear-cut interface, introducing parameter φ, which points to the presence (φ = 1) or absence (φ = 0) of a certain phase [27]. On the interface parameter φ changes abruptly, but not continuously in several points of the grid. Real position of the interface is assumed to be in the point where φ = 0.5. Physical values are order parameter functions. Proceeding from minimizing system free energy functional, evolution equations are derived for various phases. In these equations overcooling for each phase pair is included as functions of solute local concentration. In the considered model [27], concentration is treated as an external filed, and diffusion equations are reduced to φ. Thus, modeling of microstructural evolution at phase transformations associated with a set of non-linear differential equations for phase φ and concentration fields has a numerical solution.

As phase field models deal with numerical solution of differential equations, they can be easily configured both in 2D and in 3D [53]. Calculations, however, are very intensive.

Despite the fact that they should yield quantitative results, their application for modeling the processes in currently available materials requires knowledge of material physical properties, which are difficult to determine. This method, however, is becoming one of the most powerful and promising in the field of modeling phase transitions in different systems.

In conclusion it should be noted that solidification in the weld pool is the first stage of microstructure formation in fusion welding, which influences the final microstructure and, therefore, mechanical and technological properties of the weld. The main parameters governing this process are alloy composition, solidification rate and temperature gradient ahead of solidification front.

In order to allow for the influence of nonmetallic inclusions on the primary structure, and, hence, on the secondary one, dendrite growth in the weld pool during cooling should be modeled.

Considerable success has been achieved in the field of analytical modeling of dendritic structures, which, in principle, is applicable to welding. Analytical models, however, are limited to consideration of isolated dendrite tips. Interaction between diffusion fields of adjacent dendrites is ignored. Moreover, interdendrite spacing can be very roughly predicted and with a number of empirical assumptions that does not allow making qualitative predictions of metal dendrite structure in a situation, when the weld pool contains various nonmetallic inclusions.

Numerical methods of modeling concentration field propagation around the tip of a dendrite or cell allow more accurate description of needle shape, overcooling and concentration as functions of growth conditions and material properties.

Analytical and numerical models of dendrite growth do not allow for the possibility of branching, structure coarsening and microsegregation in the entire two-phase zone, as they assume complete symmetry and describe only the interface.

Direct modeling methods, such as cell automation and phase field method, potentially do not need any limitations, and are capable of simulating the entire structure during solidification. Their application allows obtaining temperature or concentration fields ahead of solidification front, dendrite tip geometry, primary and secondary spacing between dendrite branches, as well as microsegregations in partially melted zone. However, as these methods are based on numerical solutions of the main equations and/or transition rules, dimensional effect should be studied and minimized.

Positive result of application of these models to solve practical problems can be achieved in the case, when direct modeling methods are based on the results derived using analytical and numerical models.

The above-said leads to the conclusion that the most adequate and characteristic results of dendrite growth modeling, allowing for the influence of nonmetallic inclusions, can be expected from cell automation method, which should be modified to allow for the capabilities of analytical and numerical models. The advantage of this method, compared to phase field method, consists in its computational simplicity and no need for determination of some physical properties of real materials, such as mobility or anisotropy.

1. David, S.A., Babu, S.S., Vitek, J.M. (2001) Recent advances in modeling and characterization of weld microstructure. *Sci. and Techn. of Welding and Joining*, 6(**6**), 341–346.
2. Santella, M.L., Babu, S.S., Riemir, B. et al. (1999) Trends in welding research. In: *Proc. of 5th Int. Conf.* Materials Park: ASM Int., 605–609.
3. Grong, O. (1997) *Metallurgical modeling of welding*. London: TIM.
4. Joensson, P.G., Szekely, J., Choo, R.T.T. et al. (1994) Mathematical models of transport phenomena associated with arc-welding processes: A survey. *Modeling and Simulation in Material Sci. and Eng.*, **2**, 995–1016.
5. Evans, G.M., Bailey, N. (1997) *Metallurgy of basic weld metal*. Abington: Woodhead Publ.
6. Kluken, A.O., Grong, O. (1989) Mechanisms of inclusion formation in Al–Ti–Si–Mn deoxidized steel weld metals. *Metallurg. Transact. A*, **20**, 1335–1349.
7. Hseih, K.C., Babu, S.S., Vitek, J.M. et al. (1996) Calculation of inclusion formation in low alloy steel welds. *Mat. Sci. Eng. A*, **215**, 84–91.
8. Koseki, T., Ohkita, S., Yurioka, N. (1997) Thermodynamic study of inclusion formation in low alloy steel weld metals. *Sci. and Techn. of Welding and Joining*, **2**, 65–69.
9. Babu, S.S., David, S.A., Vitek, J.M. et al. (1995) Development of macro- and microstructures of C–Mn low alloy steel welds — inclusion formation. *Mat. Sci. and Techn.*, **11**, 186–199.
10. Babu, S.S., Raidebach, F., David, S.A. et al. (1999) Effect of high-energy-density welding processes on inclusion and microstructure formation in steel welds. *Sci. and Techn. of Welding and Joining*, **4**, 63–73.
11. Manson, P. (2012) Program AIDS in modeling welding thermodynamics. *Welding J.*, **12**, 28–30.
12. Andersson, J.O., Helander, T., Hoeglund, L. et al. (2002) Thermo-calc and DICTRA, computational tools for materials science. *CALPHAD.*, **26**, 273–312.
13. Babu, S.S. (2009) Thermodynamic and kinetic models for describing microstructure evolution during joining of metals and alloys. *Int. Mat. Rev.*, 54(**6**), 333–367.
14. Babu, S.S., Vitek, J.M., Iskander, Y.S. et al. (1997) New model for prediction of ferrite number of stainless steel welds. *Sci. and Techn. of Welding and Joining*, 2(**6**), 279–285.
15. Vitek, J.M., Iskander, Y.S., Oblow, E.M. (2000) Improved ferrite number prediction in stainless steel arc welds using artificial neural networks. Pt 1: Neural network development. *Welding J.*, 79(**2**), 33–46.
16. Bhadeshia, H.K.D.H., Svensson, L.E., Gretoff, B.A. (1985) A model for the development of microstructure in low-alloy steel (Fe–Mn–Si–C) weld deposits. *Acta Metall.*, **33**, 1271–1283.
17. Ion, J.C., Easterling, K.E., Ashby, M.F. (1984) A second report on diagrams of microstructure and hardness for heat-affected zones in welds. *Ibid.*, 32(**11**), 1949–1962.
18. Kasuya, T., Yurioka, N. (1993) Carbon equivalent and multiplying factor for hardenability of steel. *Welding J.*, **72**, 263–268.
19. Smallman, R.E., Bishop, R.J. (1999) *Modern physical metallurgy and materials engineering*. Oxford: Butterworth–Heinemann Publ.
20. Pavlyk, V. (2004) *Modeling and direct numerical simulation of dendritic structures under solidification conditions during fusion welding*. Aachen: Shaker.
21. David, S.A., Babu, S.S., Vitek, J.M. (2003) Welding: Solidification and microstructure. *http://www.tms.org/pubs/journals/JOM/0306/David-0306.html*
22. Trivedi, R., Kurz, W. (1994) Dendritic growth. *Int. Mat. Rev.*, 39(**2**), 47–74.
23. Kurz, W., Giovanola, B., Trivedi, R. (1986) Theory of microstructure development during rapid solidification. *Acta Metall.*, 34(**5**), 823–830.
24. McCartney, D.G., Hunt, J.D. (1984) A numerical finite difference model of steady state cellular and dendritic growth. *Metallurg. Transact. A*, **15**, 983–994.

25. Brown, S.G.R., Williams, T., Spittle, J.A. (1994) A cellular automaton model of the steady-state «free» growth of a non-isothermal dendrite. *Acta Metall. et Mat.*, 42(**8**), 2893–2898.
26. Sasikumar, R., Sreenivasan, R. (1994) 2-dimensional simulation of dendrite morphology. *Ibid.*, 2(**7**), 2381–2386.
27. Tiaden, J., Grafe, U. (1999) A phase-field model for diffusion and curvature controlled phase transformations in steels. In: *Proc. of Int. Conf. on Solid-Solid Phase Transformations* (Kyoto, Japan, 1999), 737–740.
28. Koseki, T. (2001) Solidification and solidification structure control of weld metals. *Welding Int.*, 16(**5**), 347–365.
29. Tiller, W.A., Jackson, K.A., Rutter, J.W. et al. (1953) The redistribution of solute atoms during the solidification of metals. *Acta Metall.*, **1**, 428–437.
30. Mullins, W.W., Sekerka, R.F. (1964) Stability of a planar interface during solidification of a dilute binary alloy. *J. Appl. Phys.*, 35(**2**), 444–451.
31. Ivantsov, G.P. (1947) Temperature field around spherical, cylindrical and needle-like crystal growing in supercooled melt. *Doklady AN SSSR*, 58(**4**), 567–569.
32. Temkin, D.E. (1960) On rate of crystal needle growing in supercooled melt. *Ibid.*, 132(**6**), 1307–1310.
33. Trivedi, R. (1970) Growth of dendritic needles from a supercooled melt. *Acta Metall.*, 18(**3**), 287–296.
34. Huang, H.C., Glicksman, M.E. (1981) Fundamentals of dendritic solidification: Steady-state tip growth. *Ibid.*, **29**, 701–715.
35. Langer, J.S., Mueller-Krumbhaar, H. (1977) Stability effects in dendritic crystal growth. *J. Crystal Growth*, **42**, 11–14.
36. Kurz, W., Fisher, D.J. (1992) *Fundementals of solidification*. TransTech Publ.
37. Gandin, Ch.-A., Rappaz, M. (1994) A coupled finite element-cellular automaton model for the prediction of dendritic grain structures in solidification processes. *Acta Metall.*, 42(**7**), 2233–2246.
38. Ploshikhin, V.V., Bergmann, H.W. (2001) Correlation between the welding parameters and the grain structure for the fast moving high power line heat source in a thin plate. In: *Mathematical modeling of weld phenomena 5*. London: IOM Commun., 269–281.
39. Hunt, J.D., McCartney, D.G. (1987) Numerical finite difference model for steady state cellular array growth. *Acta Metall.*, **35**, 89–99.
40. Lu, S.L., Hunt, J.D. (1992) A numerical analysis of dendritic and cellular array growth: The spacing adjustment mechanisms. *J. Crystal Growth*, **123**, 17–34.
41. Hunt, J.D., Lu, S.L. (1996) Numerical modeling of cellular/dendritic array growth: Spacing and structure predictions. *Metallurg. and Mat. Transact. A*, 27(**3**), 611–623.
42. Spittle, J.A., Brown, S.G.R. (1994) A 3D cellular automaton model of coupled growth in two component systems. *Acta Metall. et Mat.*, 42(**6**), 1811–1815.
43. Dilthey, U., Reichel, T., Pavlik, V. (1997) A modified cellular automaton model for grain growth simulation. In: *Mathematical modeling of weld phenomena 3*. London: Maney Publ., 106–113.
44. Kurien, L., Sasikumar, R. (1996) Simulation of dendrite morphology in the presence of particles. *Acta Metall.*, 44(**8**), 3385–3395.
45. Sasikumar, R., Jacob, E., George, B. (1998) Simulation of dendrite growth in binary alloys. *Scripta Mat.*, 38(**4**), 693–701.
46. Galenko, P.K., Krivilev, M.D. (2000) Isothermal growth of crystals in supercooled binary alloys. *Mat. Modelirovanie*, 12(**11**), 17–37.
47. Galenko, P.K., Krivilev, M.D. (2000) Finite-difference scheme for modeling of crystal structure formation in supercooled binary alloys. *Ibid.*, 12(**12**), 11–23.
48. Krivilev, M.D., Galenko, P.K. (2008) Modeling of transition to diffusionless solidification in high-speed crystallization of binary alloys. *Vestnik UdmurtGU*, **1**, 129–140.
49. Krivilev, M.D., Galenko, P.K. (1999) *Software complex for modeling of crystal structure formation in supercooled binary alloys*: Manual. Izhevsk: UdmurtGU.
50. Zhang, Y. (2012) Phase field modeling of dendritic growth and coarsening supercooling. *http://*www.intechopen.com/ books/supercoo-ling/phase-field-modeling-of-dendritegrowth
51. Lebedev, V.G., Danilov, D.A., Galenko, P.K. (2010) On equations of phase field model for non-isothermal kinetics of transformations in multicomponent and multiphase system. *Vestnik UdmurtGU*, **1**, 26–33.
52. Steinbach, I., Pezzolla, F., Nestler, B. et al. (1996) Phase field concept for multiphase systems. *Physica D: Nonlinear Phenomena*, 94(**3**), 135–147.
53. Kobayashi, R.A. (1994) A numerical approach to three-dimensional dendritic solidification. *Exp. Mathematics,* **3**, 410–423.

Received 22.11.2013

STRUCTURE OF SURFACE-MELTED ZONE OF CAST HIGH-NICKEL ALLOY KhN56MBYuDSh AFTER LASER SURFACE TREATMENT

A.A. POLISHKO, V.Ya. SAENKO, A.Yu. TUNIK and **S.N. STEPANYUK**
E.O. Paton Electric Welding Institute, NASU
11 Bozhenko Str., 03680, Kiev, Ukraine. E-mail: office@paton.kiev.ua

The laser surface treatment influences greatly the structure and service properties of products. The effect of this treatment on high-nickel alloys used in critical structures represents the interest. The effect of laser surface treatment on structure and properties of cast high-nickel alloy KhN56MBYuDSh was evaluated. Presented are the results of investigations of dispersity of dendrtitic structure obtained by the method of electroslag remelting (ESR) of hollow ingot of this alloy and surface-melted zone after its laser surface treatment in the nitrogen and helium atmosphere. It is shown that in the surface-melted zone the distance between the branches of dendrites is by 2 orders smaller than in cast metal in the state after ESR without the laser treatment. The results of durometric investigations are given. It was found that after the laser treatment the characteristics of microhardness are averaged within the whole volume of the melted layer. In addition, the increase in level of microhardness of the melted layer in nitrogen is observed. Generally, the positive effect of this treatment on structure and microhardness of the surface-melted zone was found. 6 Ref., 4 Tables, 8 Figures.

Keywords: *laser surface treatment, high-nickel alloy, surface-melted zone, metallographic examinations, dendritic structure, distance between the primary branches of dendrites, distance between the secondary branches of dendrites, durometric investigations, microhardness*

The laser treatment of surface is one of the challenging methods of solution of problems of the nowadays materials science in the formation of a surface working layer with preset structure and properties. During laser treatment of steels and alloys using surface melting, the surface layers can be heated for a very short time up to high temperatures and melted. In the overheated metal the impurities can be redistributed if they were previously in the form of inclusions. As the time of heating and thickness of molten layer are very small, the cooling in crystallization of the molten layer occurs at a high rate. As a result, the high-rate crystallization of the surface layer, melted by a laser beam, opens up the new opportunities for producing the radically new structural state in the surface-melted zone of cast alloys as compared with traditional welding and metallurgical processes.

Many researchers showed [1, 2] that the significant strengthening effect of the surface layer can be obtained in laser treatment with surface melting, which allows regulating easily the thickness of the strengthened layer, and also the degree of its strengthening in the presence of phase transformations. The possibility of laser surface alloying from a gas phase, in particular with nitrogen, is also important [3]. The strengthening in this case is connected with the formation of oversaturated solid solutions and new phases. The undoubted advantage of application of laser method is the possibility of surface treatment of thin-walled parts with regulated thickness and properties of strengthened layer at their minimum shrinkages, as well as developed, including inner, surfaces.

The aim of the present work is the investigation of effect of laser surface treatment on structure and hardness of surface-melted zone of ingot of high-nickel alloy of KhN56MBYuDSh grade (TU-14-1-4025–85), produced by ESR method.

As an object of investigation the specimens of cast metal cut out from a hollow ingot, produced by ESR method, of 350/230 mm diameter and 1600 mm height of alloy KhN56MBYuDSh, were used.

Technology of producing thick-walled hollow billets of alloy KhN56MBYuDSh using the ESR method was developed for the first time in 1988–1990 at the E.O. Paton Electric Welding Institute of the NAS of Ukraine under the supervision of Prof. B.I. Medovar in collaboration with N.A. Dollezhal Research and Development Institute of Power Engineering of the RAS as applied to highly-loaded elements of structures of nuclear power units with gas heat carriers [4–6].

© A.A. POLISHKO, V.Ya. SAENKO, A.Yu. TUNIK and S.N. STEPANYUK, 2014

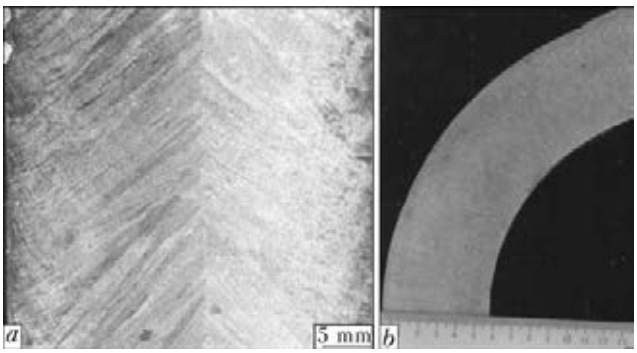

Figure 1. Macrostructure of fragments of longitudinal (*a*) and transverse (*b*) templates of 350/230 mm diameter and 1600 mm height hollow ingot of alloy KhN56MBYuDSh produced by ESR

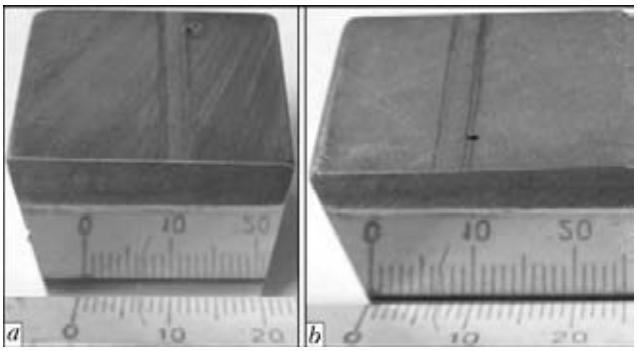

Figure 2. Appearance of specimens after laser surface melting in nitrogen (*a*) and helium (*b*)

Chemical composition of alloy KhN56MBYuDSh (TU-14-1-4025–85) is the following, wt.%: 0.041 C; 1.65 Al; 0.4 Si; 0.48 Ti; 0.4 V; 19 Cr; 10 Fe; 5.3 Mo; 4.8 Nb; 0.04 Mn; 0.002 S; 0.006 P; Ni — base.

As consumable electrodes the 55 mm diameter rods of KhN56MBYuDSh alloy, produced by vacuum-arc remelting, were used. After melting the ingot is subjected to heat treatment under the following conditions: homogenization (1150 °C, 1 h); hardening (980 °C, 1 h); ageing (730 °C, 15 h) with repeated ageing (650 °C, 10 h).

The longitudinal and transverse macrosections were cut out from the ingot to evaluate the structural homogeneity. Macrostructure, given in Figure 1, is characterized by homogeneous dense structure. Defects of shrinkage origin, pores, cracks, slag inclusions were not observed.

Table 1. Technological parameters of laser treatment with surface melting (I = 17 A, P_{em} ≈ 3 kW, 1.2–1.5 mm beam diameter, 630 mm/min speed of linear movement)

Shielding atmosphere	Width of surface-melted layer, μm	Depth of penetration, μm
Nitrogen	2050	270
Helium	1850	240

The laser surface treatment of specimens was carried out using continuous CO_2-laser in atmosphere of shielding gas of nitrogen and helium (Table 1).

Figure 2 shows specimens after laser surface melting in nitrogen and helium. Structure of the surface-melted zone is given in Figure 3.

Using the JEOL scanning electron microscope JSM-35CF (Japan) and «Oxford Instruments» X-ray spectrometer with dispersion at energy of X-ray quanta INCA Energy-350 (Great Britain), and metallographic microscope «Neophot-32» equipped with attachment for digital photography, the structure of cast high-nickel alloy KhN56MBYuDSh before and after its laser treatment with surface melting in nitrogen and helium was evaluated. Taking into account the specifics of imaging the microstructure of cast alloy for electron microscope, the back-scattered electron imaging mode was used (Figure 3).

Investigations of cast metal in as-melted state showed that the structure contains phase inclusions (eutectics), i.e. light regions, having the increased amount of molybdenum, niobium and silicon (spectra 3, 4, Figure 4, Table 2), as compared to matrix metal (spectrum 5, Figure 4, Table 2). The dark inclusions of titanium carbonitride were also revealed in matrix structure, which contain the increased amount of carbon,

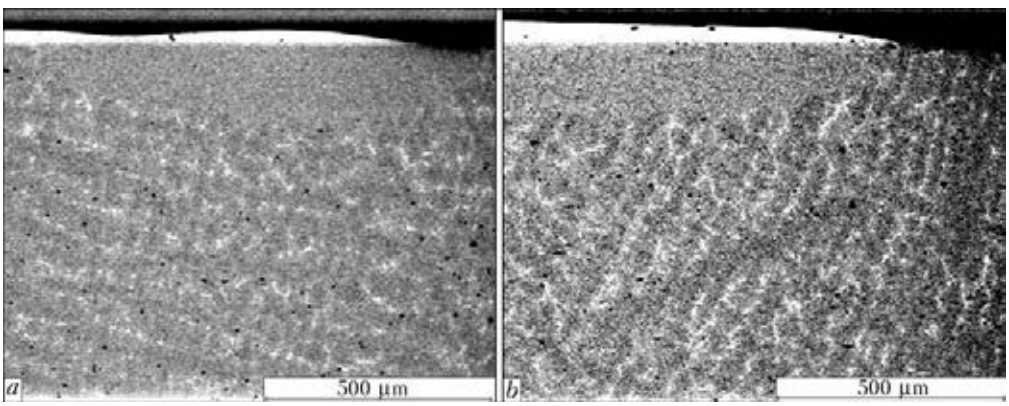

Figure 3. Microstructure of surface-melted zone in atmosphere of nitrogen (*a*) and helium (*b*), obtained by application of SEM BEI mode

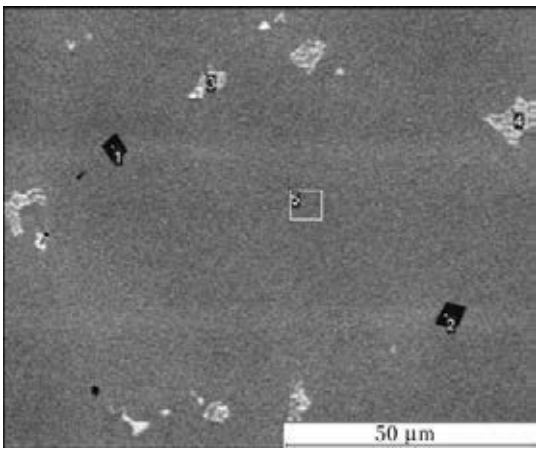

Figure 4. Microstructure of cast metal of alloy KhN56MBYuDSh without laser treatment

nitrogen, titanium and niobium (spectra 1, 2, Figure 4, Table 2).

Examination of metal after laser treatment in nitrogen showed that the surface melting results in dispersion of eutectics, i.e. light regions in matrix structure, containing increased amount of niobium and molybdenum. Refining of inclusions of carbonitrides (dark inclusions in matrix structure) is occurred (Figure 5, *a*; Table 3). The external surface of remelted metal has a golden tint, typical of the titanium nitride.

Investigation of metal after laser treatment with surface melting in helium showed that as a result of laser surface melting the dispersion of eutectics (light regions in matrix structure), containing the increased amount of niobium and molybdenum, refining of titanium carbonitrides (dark inclusions in matrix structure) is also occurred in HAZ. However, in the surface-melted zone the almost complete absence of inclusions of titanium carbonitrides is observed (Figure 5, *b*; Table 4).

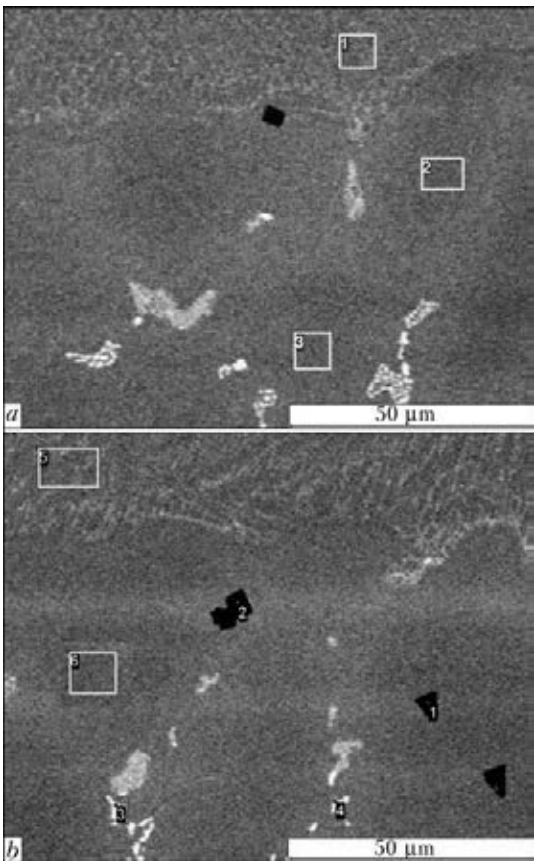

Figure 5. Microstructure of surface-melted zone (*upper area*) and cast metal (*lower*) of alloy KhN56MBYuDSh after laser treatment in nitrogen (*a*) and helium (*b*)

Optical metallographic examinations of cast metal of high-nickel alloy KhN56MBYuDSh were carried out on etched sections (in reagent of 5 mg $CuCl_2$ + 100 ml HCl + 100 ml ethanol), using microscope «Neophot-32» with attachment for digital photography.

The clearly expressed dendritic structure, typical of cast metal, was revealed in base metal

Table 2. Chemical composition (wt.%) of local regions (see Figure 4)

Number of spectrum	C	N	Al	Si	Ti	V	Cr	Fe	Ni	Nb	Mo
1	6.87	17.77	0	0	49.28	2.58	2.16	0.35	1.31	19.09	0.59
2	6.99	17.97	1.03	0.27	50.74	0.34	1.66	1.77	3.44	14.68	0.91
3	2.94	0	0.59	1.23	0.31	0.20	13.11	10.51	40.28	15.30	13.55
4	4.14	0	0.75	0.92	0.47	0.25	13.28	10.15	42.24	17.31	10.48
5	0	0	1.19	0.22	0.15	0.36	17.78	15.62	55.53	2.47	5.01

Table 3. Chemical composition (wt.%) of local regions (see Figure 5, *a*)

Number of spectrum	C	N	O	Al	Ti	V	Cr	Fe	Ni	Nb	Mo
1	3.68	0	0	1.18	0.36	0.30	16.82	14.02	54.02	3.94	5.67
2	2.60	0	1.01	1.20	0.19	0.40	17.67	15.33	53.76	2.68	5.16
3	2.82	0	0	1.26	0.25	0.43	17.58	13.98	54.45	3.56	5.67

Table 2. Chemical composition (wt.%) of local regions (see Figure 5, *b*)

Number of spectrum	C	N	O	Al	Si	Ti	V	Cr	Fe	Ni	Nb	Mo
1	5.58	18.70	3.94	0	0	48.79	1.78	1.64	0.27	1.34	17.12	0.83
2	6.56	15.23	5.04	0.11	0	49.19	1.65	1.23	0.43	1.33	18.53	0.70
3	5.51	0	0	1.22	0.14	0.30	0.30	15.66	12.21	53.96	5.35	5.35
4	5.91	0	1.72	0.54	1.26	0.23	0.20	13.42	9.79	38.28	14.81	13.83
5	2.68	0	0	1.25	0.17	0.28	0.50	17.12	14.14	54.16	3.92	5.79
6	0	0	0	1.23	0.14	0	0.45	18.14	15.84	57.33	2.07	4.80

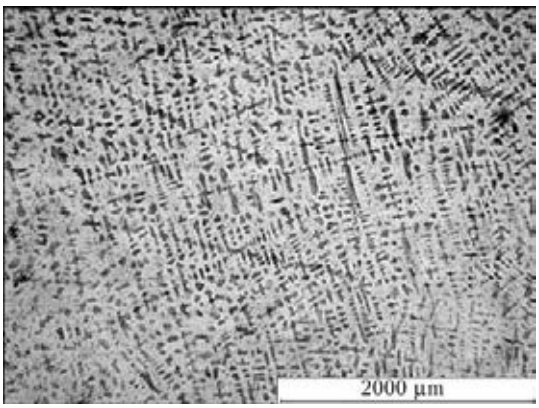

Figure 6. Microstructure of as-melted cast metal of alloy KhN56MBYuDSh

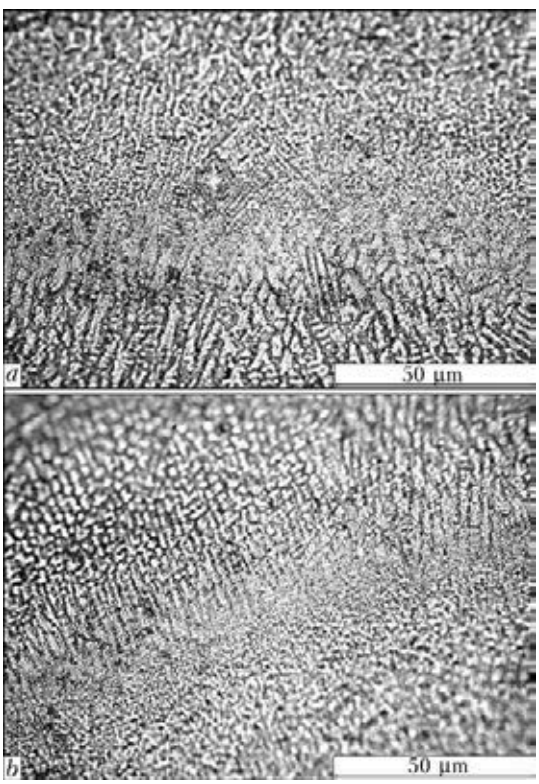

Figure 7. Microstructure of surface-melted zone of cast metal of alloy KhN56MBYuDSh after laser surface treatment in nitrogen (*a*) and helium (*b*)

even after its laser surface treatment in nitrogen and helium (Figures 6 and 7).

For comparison and quantitative description of dendritic structure the parameter was selected in the form of distance between the primary branches of dendrites. The distance between the secondary branches of dendrites was selected as a characteristic of dispersity of the dendritic structures. This distance was evaluated by using the metallographic investigations with application of computer program Tescan.

It was found that in as-melted cast metal the distance between the primary branches of dendrites is varied from 224 up to 862 μm, and it is 60–245 μm between the secondary ones, i.e. the distance between the primary branches is almost 3 times longer than that between the secondary ones.

In the surface-melted zone in nitrogen atmosphere the distance between the primary branches of dendrites is 1.8–5.0 μm, between the secondary ones — 1.6–4.2 μm; in helium the distance between the primary branches is 1.9–4.5 μm and between the secondary ones — 1.5–4.2 μm. The distances between the primary and secondary branches of dendrites in the surface-melted zone

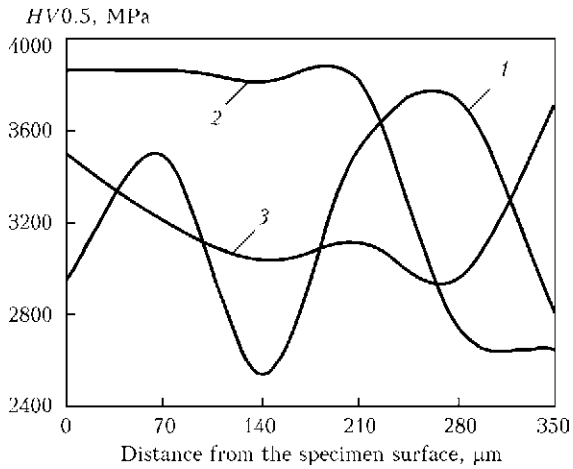

Figure 8. Distribution of microhardness in cast metal of alloy KhN56MBYuDSh: *1* — in as-melted state; *2*, *3* — in surface-melted zone after laser treatment, respectively, in nitrogen and helium

in atmosphere of nitrogen and helium are almost similar, moreover, they are by 2 orders shorter than in as-melted cast metal without laser treatment.

Durometric investigations were carried out in the LECO hardness meter M400 at 0.05 kg load. The results of analysis of distribution of microhardness in the surface-melted zone of surface layer, produced as a result of laser treatment in atmosphere of nitrogen and helium, as well as cast metal without laser treatment, are presented in Figure 8. In the surface-melted zone the more uniform distribution of microhardness is observed as compared with cast metal without laser treatment. In addition, it was found that the level of microhardness of the surface-melted zone after laser treatment in nitrogen is higher than that of surface layer of surface-melted zone in helium.

Conclusions

As result of laser surface treatment with surface melting of cast high-nickel alloy KhN56MBYuDSh a homogeneous layer of 240–270 μm thickness is formed on its surface, in which the dispersion of eutectics, enriched with molybdenum and niobium, and refining of carbonitride inclusions of titanium are occurred.

Durometric investigations showed that the microhardness is averaged in the whole volume of surface-melted layer, as compared with cast metal without the laser treatment, moreover, the microhardness of cast metal matrix is at the level of 2600–2900 MPa, of surface-melted layer in helium — 3100–35000 MPa, and of surface-melted layer in nitrogen — 3800–3900 MPa. The increase in level of microhardness of surface-melted layer in use of nitrogen as a shielding gas can be predetermined by some level of metal nitriding, that is proved by a golden tint of the external surface, characterizing the presence of titanium nitrides on the surface.

It was found as a result of metallographic investigations that in cast metal without laser treatment the distance between the primary branches of dendrites is approximately 3 times longer than that between the secondary ones, while in the surface-melted zone the distance between the primary and secondary branches of dendrites is almost similar. In addition, in the surface-melted zone the distance between the branches of dendrites by 2 orders shorter than in as-melted cast metal without laser treatment.

In general, the laser treatment with surface melting favorably influences the structure and properties of cast high-nickel alloy KhN56MBYuDSh, providing the formation of quality homogeneous surface working layer.

1. Sadovsky, V.D., Schastlivtsev, V.D., Tabatnikova, T.M. et al. (1989) *Laser heating and structure of steel*: Atlas of microstructures. Sverdlovsk: UrO AN SSSR.
2. Brover, A.V., Diachenko, L.D. (2009) Peculiarities of structure formation in zones of laser surface melting of metals and alloys. *Metallovedenie i Termich. Obrab. Metallov*, **1**, 29–33.
3. Chudina, O.V., Aleksandrov, V.A., Brezhnev, A.A. (2010) Combined surface strengthening of carbon steels by laser alloying with subsequent nitriding. *Uprochn. Tekhnologii i Pokrytiya*, **4**, 33–37.
4. Tikhonov, V.A., Medovar, B.I., Saenko, V.Ya. et al. (1990) Producing of hollow ingot of high-nickel alloy by ESC method. *Problemy Spets. Elektrometallurgii*, **2**, 39–42.
5. Bashnin, Yu.A., Korostylyov, A.B. (1993) Selection of conditions for quenching of electroslag remelted alloy KhN56MBYuD. *Metallovedenie i Termich. Obrab. Metallov*, **3**, 19–23.
6. Paton, B.E., Chepurnoj, A.D., Saenko, V.Ya. et al. (2004) Prospects of application of electroslag technologies in production of high-pressure vessels. *Advances in Electrometallurgy*, **1**, 2–8.

Received 24.12.2013

TECHNOLOGICAL PECULIARITIES OF WELDING OF WROUGHT MAGNESIUM ALLOYS BY ELECTRON BEAM IN VACUUM

A.A. BONDAREV and **V.M. NESTERENKOV**
E.O. Paton Electric Welding Institute, NASU
11 Bozhenko Str., 03680, Kiev, Ukraine. E-mail: office@paton.kiev.ua

Magnesium alloys find ever wider application in different fields of industrial production, especially when products should have the lowest mass characteristics. Use of magnesium alloys for manufacture of such structures is the most challenging, but in this case, the technologies of their manufacture including also processes of welding using different methods, should be available and reliable. At the present time many specialists attribute the EBW to the category of high technologies. Firstly, the EBW process is carried out under the conditions of vacuum environment, which absolutely eliminates any oxidizing processes of liquid metal in weld pool. Moreover, during melting in vacuum the refining purification of molten metal from harmful impurities takes place, and strength characteristics of joints are the highest in this case. In the present work the results of experimental investigations of weldability of wrought magnesium alloys of different thicknesses produced using electron beam are given. The influence of the system of alloying and parameters of mode on formation of welds and sizes of penetration zone of billets of different thickness was shown. The strength characteristics of welded butt joints were determined. 8 Ref., 4 Tables, 6 Figures.

Keywords: *electron beam welding, magnesium alloys, welding modes, strength of welded joints, microstructure of weld and base metal*

Magnesium alloys, being the lightest structural material and having comparatively high mechanical properties, are characterized by high chemical resistance towards a number of aggressive environments and are capable to perceive high impact loads due to low elasticity modulus, and also well treated by a cutting tool. The number of grades of industrial wrought magnesium alloys approaches to about two dozens. Among light metals aluminium is 1.5 times and titanium 2.5 times heavier than magnesium, and steel is 4 times heavier than the latter. This explains growing interest to application of magnesium alloys in different fields of industry both in our country as well as abroad [1–4].

The application of magnesium alloys as a structural material in welded structures would not be possible without development of methods of their technological treatment and welding [5, 6].

The large number of works [7] is devoted to the weldability of magnesium alloys of different systems of alloying using arc welding methods, including also superlight structural alloys of the Mg–Li system.

However, as the analysis of works devoted to investigations of weldability of magnesium alloys showed, these matters are still not sufficiently highlighted in the literature. And the information on weldability of magnesium alloys using electron beam is practically absent.

The results of earlier carried out investigations evidence that magnesium alloys of grades MA2-1, MA12, IMV2, IMV2-1 and alloys of the alloying systems Mg–Zn–Zr–Ce and Mg–Nd–Zr can be successfully welded using arc methods. The strength factor of joints for most of them is in the range of 0.9–1.0 of the base metal. Other strength values of joints are also at the level of properties of base metal at a high density of weld metal.

The main problem in welding of magnesium alloys is to prevent formation of hot cracks in welded joints.

At the E.O. Paton Electric Welding Institute the investigations on weldability of magnesium alloys, the grade and chemical composition of which are given in Table 1, were carried out.

MA2-1 alloy belongs to lower-alloy medium-strength magnesium alloys. It has a good ductility in hot state and is good welded using arc methods. It was used in work to select parameters of mode for welding billets of this alloy of up to 200 mm thickness.

The alloy VMD-3 based on the Mg–Zn–Zr system belongs to the category of high-alloy and the most strength magnesium wrought alloys. This alloy is additionally alloyed with cadmium and lanthanum. It is known that lanthanum during its introduction in the amount of 0.2–0.8 %

© A.A. BONDAREV and V.M. NESTERENKOV, 2014

Table 1. Chemical composition of magnesium alloys investigated, wt.%

Alloy	Al	Zn	Mn	Li	Cd	Nd	La	Zr	Ni	Si	Fe	Be
MA2-1	3.8–5.0	0.8–1.5	0.4–0.8	–	–	–	–	–	0.005	0.10	0.05	0.02
VMD-3	–	2.3–3.5	–	–	1–2	–	0.5–1.0	0.5–0.9	0.005	0.15	0.03	0.02
VMD-6	0.1	5.5–7.0	–	–	0.2–1.0	1.4–2.0	–	0.5–0.9	0.004	0.15	0.04	0.002
IMV-2	5.0	1.0	0.4	8.0	4.0	–	–	–	–	–	–	–

Table 2. Mechanical properties of investigated magnesium alloys

Alloy	Semi-product	σ_t, MPa	$\sigma_{0.2}$, MPa	δ, %	KCV, J/cm^2
MA2-1	Plate	270.3–280.0	210.6–230.5	11.3–12.5	0.5–0.7
VMD-3	Sheet	270.1–280.3	230.5	6.5–9.5	0.45
VMD-3	Plate	320	260	13.2	–
VMD-6	Sheet	200.4–210.2	90.2–90.5	5.3–8.7	0.25
IMV-2	Same	220–230	190.0–190.5	17.5–20.0	0.4–0.5

provides intensified refining of grains and increases strength of alloys of the Mg–Zn system. This alloy has a good ductility in hot state and satisfactory weldability. In the work the specimens of this alloy in the form of sheets 2.5 and 10 mm thick were used.

The alloy VMD-6 is a new high-strength wrought magnesium alloy. It is not weldable and applied for high-load parts. In the work the specimens of this alloy in the form of discs of 6 mm thickness, cut out of a rod of 160 mm diameter, were used.

The alloy IMV-2 belongs to the series of superlight structural alloys based on Mg–Li, it has a low density (1.6 g/cm^3), high specific rigidity and good arc weldability. Besides, the alloys of the system Mg–Li have high resistance to hot cracks formation in welding and low sensitivity to hydrogen porosity. However, the presence of high content of lithium with high sensitivity to oxygen in the alloy requires careful protection of molten metal of weld pool and heated adjacent areas of base metal from the surrounding air. For this purpose, it is recommended to apply the argon blowing on the side of penetration in arc welding.

During optimizing the EBW modes and techniques of above-mentioned magnesium alloys the specimens of 12 mm thickness were used. The properties of investigated alloys are given in Table 2.

In the process of carrying out of investigations all the given grades of alloys were welded without fillers. The assembly of specimens for welding was performed with the smallest possible gaps. Preparation of edges was performed using scraping to the depth of up to 0.1 mm. Before this the specimens were subjected to degreasing with organic solvents.

Welding of billets of alloys MA2-1 and VMD-3 of 100 mm thickness and larger, and 450 mm length was performed using power source ELA-60/60 with accelerating voltage of 60 kV and beam current of up to 1 A.

The modes of welding of magnesium alloy joints, providing full penetration depth at minimum required power, are given in Table 3.

EBW of mentioned alloys was performed both by static beam as well as by the beam rotating around the circumference. Frequency of oscillations was accepted equal to 300 Hz, and amplitude — to 1.5 mm.

The properties of joints were determined on the round specimens of the type II according to GOST 6996–66, impact toughness was determined on the specimens with Mesnager notch.

Table 3. Condition parameters of welding the magnesium alloys of different thickness (U_{acc} = 60 kV)

Alloy	Thickness, mm	Beam current, mA	Welding speed, m/h
MA2-1	20	80	45
MA2-1	135	430	15
MA2-1	165	430	10.5
VMD-3	10	45	55
VMD-3	7	30	24
VMD-3	11	40	24
VMD-3	135	450	14
VMD-6	7.5	40	48
VMD-6	7.5	30	33
IMV-2	10	22	24
IMV-2	12	27	24

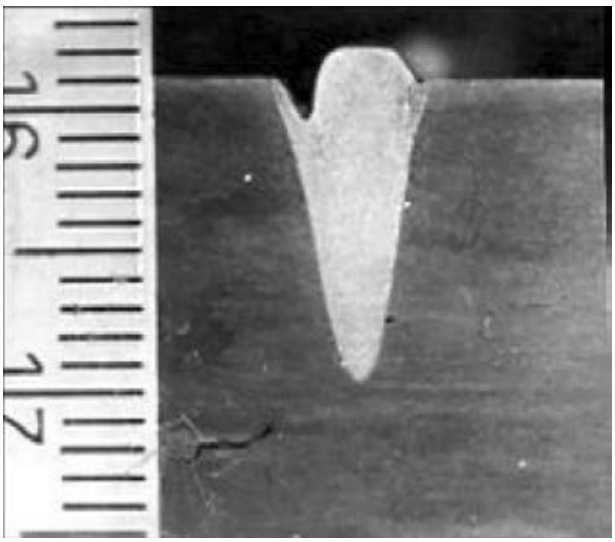

Figure 1. Macrosection of alloy MA2-1 joint with partial penetration

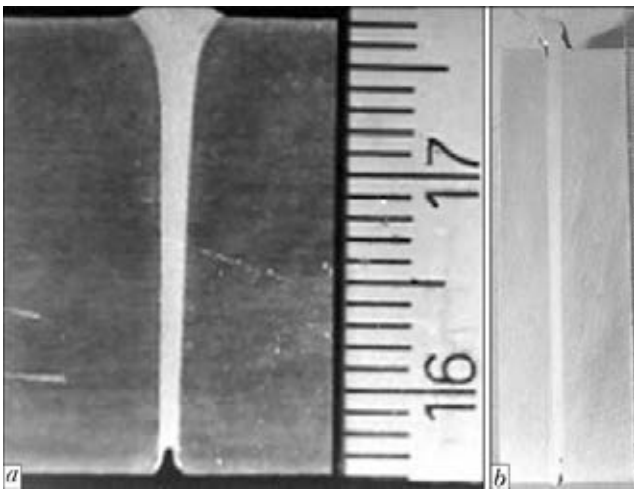

Figure 2. Formation of root part of weld 20 (*a*) and 100 (*b*) mm depth in EBW of MA2-1 alloy with full penetration

Visual control of the process of EBW of magnesium alloys allowed establishing the fact that depending on the system of alloying the behavior of molten metal of weld pool is different. Thus, in welding of alloys MA2-1 and VMD-3 with full penetration and alloy IMV-2 with full and partial penetration the process runs smoothly, without splashes and spattering of molten metal. In this case in welds the defects of the type of undercuts of 2–3 mm depth on the both sides of upper bead along the fusion zone are observed (Figure 1).

In EBW one more feature in formation of a joint was observed, which is peculiar only to magnesium alloys. It consists in the fact that in welding with full penetration almost in all the cases on the side of root weld the blowing out of molten metal occurs by pressure of vapors in the crater. As a result the undercut of up to 3.5 mm depth is formed (Figure 2). With the growth of thicknesses of billets being welded the deep undercuts are formed both on the side of weld root as well as on the side of upper bead (Figure 2, *a*). To remove these defects the upper and lower backing straps are applied, which are removed after welding (Figure 3).

In the process of carrying out the investigations all the welded joints of magnesium alloys were subjected to X-ray control to detect inner defects. The results of analysis showed that in EBW the pores and cracks are not formed. Cracks were not detected even on the billets of alloy VMD-6, which by their design correspond to one of the most complicated variants of round sample for determination of tendency to cracks formation. The results of investigations of properties of joints of magnesium alloys are given in Table 4. The joints of all the given alloys were not subjected to heat treatment after welding.

Table 4. Mechanical properties of welded joints of magnesium alloys

Alloy	Thickness of metal to be welded, mm	σ_t, MPa	$\sigma_{0.2}$, MPa	δ, %	*KCV*, J/cm^2
MA2-1	20	$\frac{250.1–250.7}{250.4}$	$\frac{210.2–250.3}{230.6}$	$\frac{8.0–12.5}{10.4}$	0.5
MA2-1	135	$\frac{250.8–270.6}{260.9}$	$\frac{120.2–130.4}{120.8}$	$\frac{11.7–16.7}{15.2}$	$\frac{0.75–1.0}{0.85}$
VMD-3	10	$\frac{250.6–270.9}{260.8}$	$\frac{220.5–230.4}{220.7}$	$\frac{5.2–8.4}{7.5}$	0.4
VMD-3	135	$\frac{220.3–250.9}{240.5}$	$\frac{220.0–240.8}{230.2}$	6.7	0.5
VMD-3	135	$\frac{260.3–270.2}{260.85}$	$\frac{250.2–260.3}{250.6}$	5.4	0.5
IMV-2	12	$\frac{200.5–220.4}{210.8}$	$\frac{170.8–180.1}{10.8}$	4.0	0.3–0.7
VMD-6	7.5	$\frac{200.6–200.8}{200.6}$	Fracture beyond the base	–	0.4

Analysis of results of mechanical properties of fractured specimens showed that in the alloys IMV-2 and VMD-6 the fracture occurred in all the cases on base metal at the distance of 10–15 mm from the weld axis. The difference in values of ultimate strength for IMV-2 sheets 10 and 12 mm thick was not detected. Fracture of specimens of alloys MA2 and VMD-3 occurred mostly along the weld metal. In EBW of MA2-1 alloy of 135 mm thickness and next cutting out of specimens of different areas of welds in depth the anisotropy of strength characteristics in weld was not detected.

Impact toughness of joints (weld metal and HAZ) for investigated grades of alloys is at the level of similar characteristics for base metal.

Strength factor of joints for alloys IMV-2 and VMD-6 is practically equal to one. For the alloys MA2-1 and VMD-3 it is in the range of 0.95–1, and for VMD-3 is 0.75–0.85.

Analysis of microstructure of different areas of joints of magnesium alloys showed that structure of weld metal in EBW almost does not differ from that of alloys in cast state. Considering the high rates of solidification in EBW somewhat smaller size of grains and thickness of intergranular sublayers are observed as compared to the structure of welds in arc welding methods [8]. Visual defects in weld metal on the alloys MA2-1, VMD-6 and IMV-2 are not observed (Figure 4).

In HAZ metal at the area adjacent to the fusion zone, recrystallziaiton of initial structure of base metal with formation of equiaxial grains is observed. However, here the general direction of texture of base metal is observed (Figure 5). Thickening of intergranular sublayers with precipitation of low-melting eutectics in HAZ metal is about 3–5 times higher than in base metal.

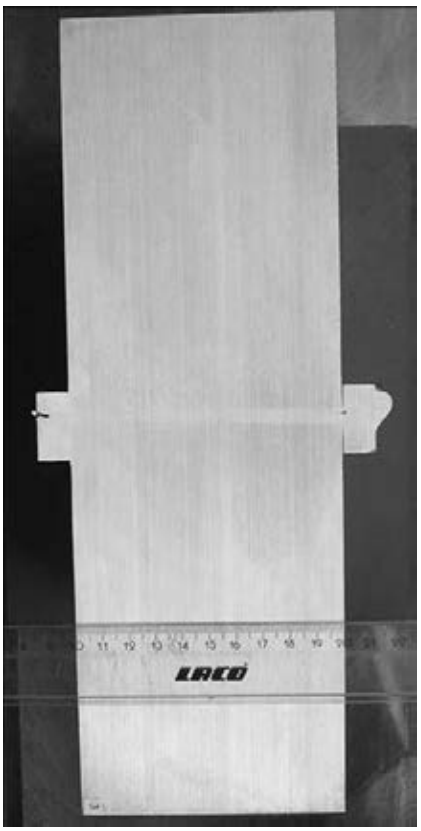

Figure 3. Formation of welds in EBW of alloy MA2-1 with two backing straps

Figure 6 presents for comparison structure of base metal of alloys MA2-1, VMD-6 and IMV-2.

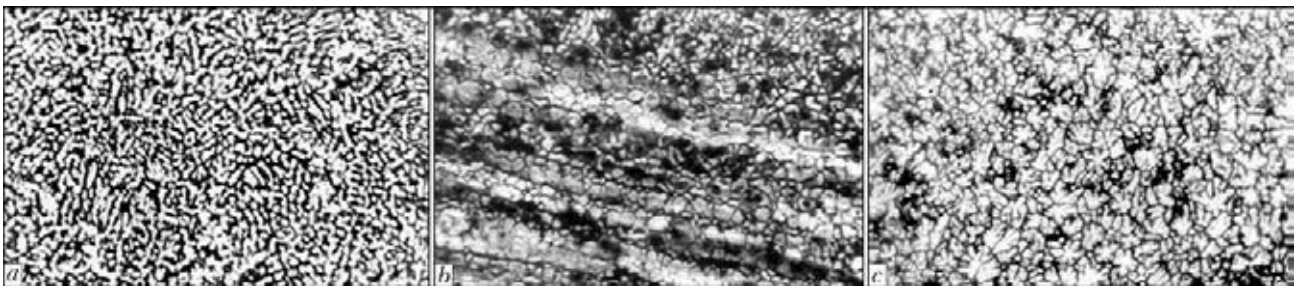

Figure 4. Microstructure (×150) of weld metal on alloys MA2-1 (*a*), VMD-6 (*b*) and IMV-2 (*c*)

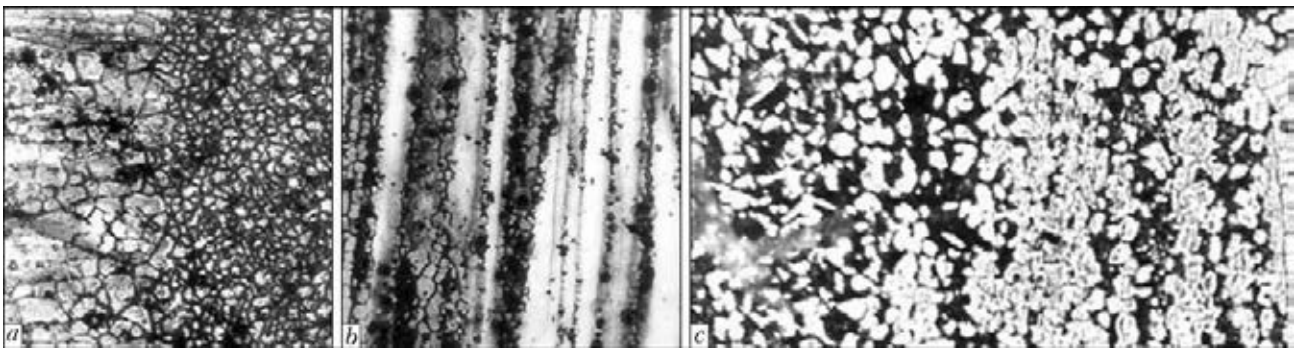

Figure 5. Microstructure (×150) of welded joints of alloys MA2-1 (*a*), VMD-6 (*b*) and IMV-2 (*c*) in the fusion zone

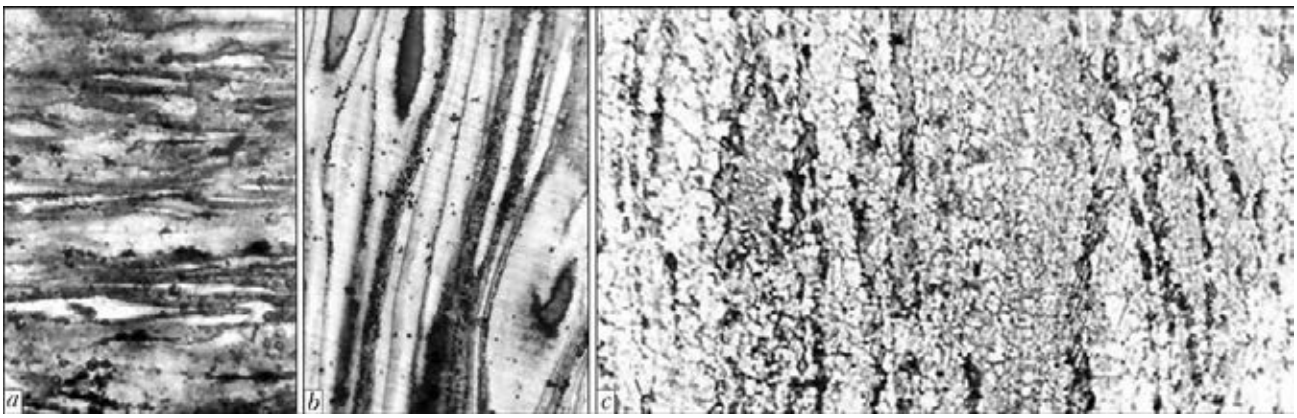

Figure 6. Microstructure (×150) of base metal of alloys MA2-1 (*a*), VMD-6 (*b*) and IMV-2 (*c*)

Conclusions

1. Complex investigations of weldability of magnesium alloys, using electron beam in vacuum, including high-strength Mg–Li alloys were carried out.

2. It was established that to provide high quality of formation and strength properties of joints, welding should be performed using scanning electron beam at the frequencies 200–700 Hz and amplitude of 1.5–2.5 mm.

3. It was shown that strength characteristics of welded joints of high-strength magnesium alloys are at the level not lower than 95 % of similar properties of base metal.

4. It is recommended to use cover plates and backings under the butt of the same metal at the thickness of not less than 5–10 mm in preparation of butt joints to prevent formation of defects in the form of lowering of surface of welds or flowing out of molten metal on the back side of weld.

1. (1978) *Magnesium alloys*: Refer. Book. Vol. 1: Metals science of magnesium and its alloys. Ed. by M.B. Altman, A.F. Belov, V.I. Dobatkin et al.; Vol. 2: Technology of production and properties of castings and strained semi-products. Ed. by I.I. Guriev, M.V. Chukhrov. Moscow: Metallurgiya.
2. Rokhlin, L.L., Nikitina, N.I., Volchenkova, V.A. (2006) Examination of magnesium-enriched alloys Mg–Al_2Cu. *Metally*, **2**, 104–108.
3. Drits, M.E. (1964) *Magnesium alloys for service at higher temperatures*. Moscow: Nauka.
4. Vozdvizhensky, V.M., Grachev, V.A., Skassky, V.V. (1984) *Cast alloys and technology of their melting in machine-building*. Moscow: Mashinostroenie.
5. (1978) To problem of electron beam welding of magnesium alloys. In: *Magnesium alloys*. Moscow: Nauka.
6. Ejdenzon, M.A. (1974) *Metallurgy of magnesium and other light metals*. Moscow: Metallurgiya.
7. (1978) *Magnesium alloys*: Transact. of A.A. Baikov Institute of Metallurgy. Moscow: Nauka.
8. Bondarev, A.A., Nesterenkov, V.M. (2013) Study of weldability of magnesium alloy MA2 by electron beam in vacuum. *Kompres. Energetich. Mashinostroenie*, **2**, 21–28.

Received 10.07.2013

HIGH-POWER LASER WELDING OF AUSTENITIC STAINLESS STEEL WITH ELECTROMAGNETIC CONTROL OF WELD POOL

M. BACHMANN, V. AVILOV, A. GUMENYUK and **M. RETHMEIER**
BAM — Federal Institute for Materials Research and Testing
87 Unter den Eichen, 12205, Berlin, Germany. E-mail: marcel.bachmann@bam.de

Laser deep-penetration welding became a widely applied tool in industrial applications due to available laser power of 20 kW and more for the single-pass welding of steel plates of up to 20 mm thikness. Above a critical limit, liquid metal tends to drop out of the bead due to hydrostatic pressure. Laser welding, in contrast to electron beam welding technique, allows for an electromagnetic manipulation of fluid flow in the weld pool. AC electromagnetic system for compensation of the hydrostatic pressure by induced Lorentz forces in the melt was experimentally and numerically investigated for single-pass full-penetration welding of up to 20 mm thikness austenitic stainless steel plates of grade AISI 304. It was shown that the application of 200–234 mT magnetic fields at oscillation frequency of around 2.6 kHz lead to a full compensation of hydrostatic forces in the melt for plate 10–20 mm thick, respectively. Coupled fluid flow, thermal and electromagnetic finite element simulations were done with different applied magnetic flux densities and oscillation frequencies calculating for the optimal magnetic field strength to avoid melt sagging in the weld pool. The simulation results point to a lower magnetic field density needed for that purpose. The reason for that can lie in the magnetic properties of the material not being totally non-ferromagnetic. 17 Ref., 1 Table, 5 Figures.

Keywords: *laser welding, high power, austenitic stainless steels, drop out of bead, control magnetic field, hydrostatic force compensation, modeling of fluid flow, calculation*

In the course of the last decade, the availability of laser sources within the power class above 10 kW made it possible to weld ever thicker aluminium and steel plates of up to 30 mm in a full-penetration process [1, 2]. Such a process has the advantage of being very efficient along with the well-known key benefits of laser welding compared to multipass arc welding processes, e.g. the low heat input, high welding speeds as well as low distortion [3].

The present investigation deals with the single-pass laser welding of up to 20 mm thickness stainless steel plates of AISI 304 grade. The conventional method to weld thick components is to use EBW [4, 5], which brings up challenges for large modules due to the need of technical vacuum. Nowadays, modern laser beam sources enable a stable single-pass welding process up to 16 mm penetration for steel [6, 7].

Above a critical limit, the surface tension of the molten material cannot balance the hydrostatic pressure of the melt and drops out during the welding before solidification occurs.

Another challenge are the highly dynamical processes in the welding zone, e.g. due to Marangoni flow and natural convection.

Laser welding in contrast to EBW allows for an electromagnetic treatment of the melt. Electromagnetic technologies in the processing of metals are widespread and range from crystal growth and cold crucible melting to the porosity prevention and surface treatment [8], and also stirring [9] in welding applications.

The approach in this investigation is the application of oscillating magnetic field perpendicular to welding direction below the welding zone, which induces eddy currents contactless. The resulting volumetric Lorentz forces in the melt counteract the effect of gravitational forces and compensate for the hydrostatic pressure. System of electromagnetic weld pool control was already experimentally [10, 11] investigated for steel of up to 18 mm thickness and aluminium alloys 30 mm thick. Numerical justification for 20 mm aluminium was presented in [12].

The present investigation deals with the numerical calculation and experimental validation of the electromagnetic weld support system for 20 mm stainless steel AISI 304. Representative simulation studies of a fluid flow simulation coupled with an electromagnetic processing are presented in [12–14].

*Basing on the paper presented at the Int. Conf. on Laser Technologies in Welding and Materials Processing (27 – 31 May 2013, Katsively, Crimea, Ukraine).

© M. BACHMANN, V. AVILOV, A. GUMENYUK and M. RETHMEIER, 2014

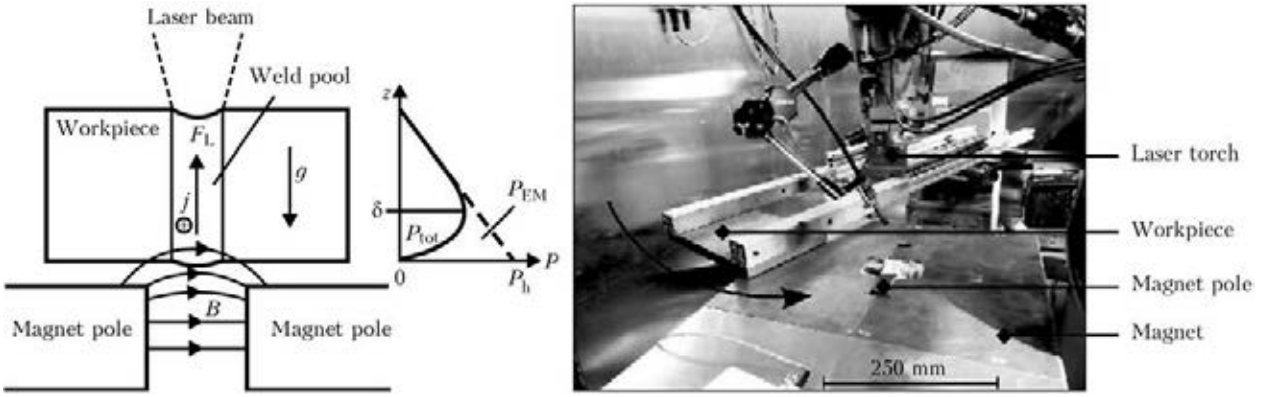

Figure 1. Scheme of the electromagnetic weld pool support system (*a*) and experimental setup (*b*)

Experimental setup. Working principle of the applied electromagnetic weld pool support is sketched in Figure 1, *a*. The oscillating magnetic field B is located in the centre below the weld pool and induces eddy currents j within the skin depth $\delta = (\pi f \mu \sigma)^{-1/2}$ of the material, where f is the oscillation frequency; μ is the magnetic permeability, and σ the electric conductivity. Interaction of the induced currents with applied magnetic field produces a Lorentz force $F_L = jB$ in the melt, which counteracts the hydrostatic pressure and, in the case of an optimal control, ensures balancing of pressures on the upper and lower weld surfaces to avoid dropping of the melt.

The magnet was located 2 mm below the workpiece. The magnet poles had a distance of 25 mm, and their cross section had the dimensions 25 × × 25 mm. The experimental setup can be seen in Figure 1, *b*.

The bead-on-plate welds were done with fibre laser with beam power of up to 18 kW. Welding of 20 mm AISI 304 steel produced no reasonable result as the liquid material was blown out of the weld. Therefore, the 20 mm joints were made on 10 mm AISI 304 austenitic steel at the root side and 10 mm S235 ferritic steel above as the higher surface tension of S235 steel stabilizes the weld surface. The penetration depth of magnetic field was adjusted at around 10 mm so that the magnetic characteristics of the ferritic S235 steel do not influence the applied magnetic field significantly. The 20 mm case was supposed to show the principal applicability of the magnetic weld pool support for even higher plate thicknesses. The laser and optics properties are summarized below:

Laser type	Yb, fibre
Fibre diameter, μm	200
Focal length, mm	350
Maximal laser power, kW	20
Focal spot diameter, μm	600
Shielding argon flow, l/min	30

Mathematical modelling. The numerical model calculates the turbulent fluid flow equations, i.e. mass conservation with mass density ρ and velocity u, and the Navier–Stokes equations with dynamic viscosity η, pressure p and source term F:

$$\nabla(\rho u) = 0, \tag{1}$$

$$\rho(u\nabla)u = -\nabla p + \nabla\left[\eta(\nabla u + (\nabla u)^T) - \frac{2}{3}\eta(\nabla u)I\right] + F, \tag{2}$$

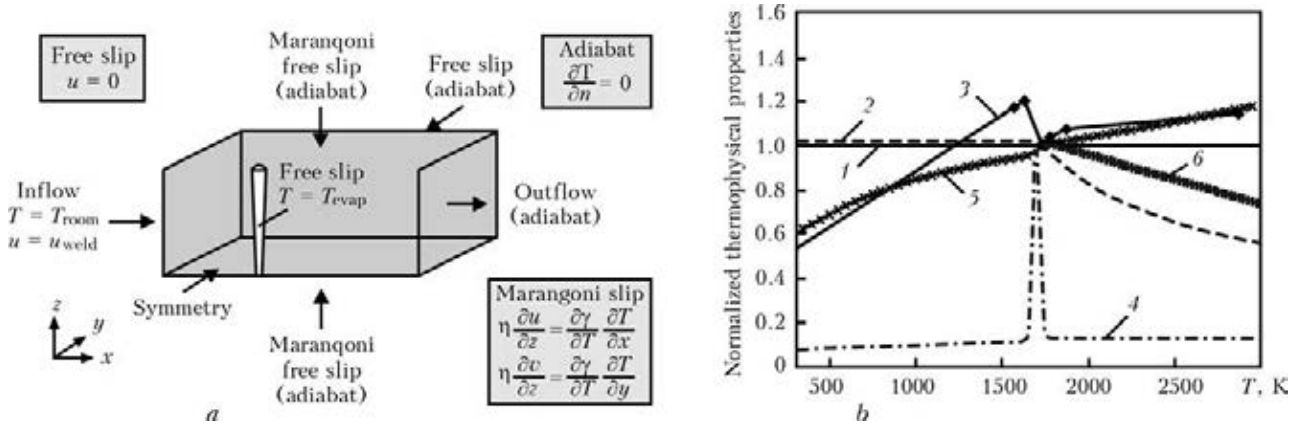

Figure 2. Boundary conditions (*a*), and thermophysical properties of stainless steel AISI 304 at T_{melt} (*b*): *1* — density ρ/ρ; *2* — dynamic visvosity η/η; *3* — heat conductivity λ/λ; *4* — heat capacity C_p^{eff}/C_p^{eff}; *5* — electrical resistivity ρ_{el}/ρ_{el}; *6* — surface tension γ/γ

$$F = -\rho g - c_1 \frac{(1 - f_l)^2}{f_l^3 + \varepsilon} (u - u_{weld}) + <jB>. \quad (3)$$

In (3), the first term accounts for the gravitational influence, the second term refers to braking of the solidified material down to processing velocity, and the last term — to applied time-average of the Lorentz force; f_l is the liquid fraction, and c_1 and ε are the constants.

Additionally, the energy equation with effective heat capacity C_p^{eff} accounting also for the latent heat of fusion, temperature T and heat conductivity λ is solved:

$$pC_p^{eff} u\nabla T = \nabla(\lambda \nabla T). \quad (4)$$

The Maxwell equations with electric field E accounts for the applied electromagnetic influence of the weld support system. The influence of flow field on electric current density distribution is described by the generalized Ohm's law:

$$\nabla B = \mu j, \quad \nabla E = \frac{\partial B}{\partial t}, \quad j = \sigma(E + uB). \quad (5)$$

The boundary conditions are summarized in Figure 2, *a*. They are explained in more detail in [12]. The used material model was taken from [15–17] (Figure 2, *b*), and thermophysical properties of stainless steel AISI 304 at T_{melt} = 1700 K and T_{evap} = 3000 K are given below:

Density ρ, kg/m^3	6900
Latent heat of fusion H_f, J/kg	$2.61 \cdot 10^5$
Dynamic visvosity η, Pa·s	$6.4 \cdot 10^{-3}$
Marangoni coefficient γ', N/(m·K)	$-4.3 \cdot 10^{-4}$
Heat capacity C_p, J/(kg·K)	800
Heat conductivity λ, W/(m·K)	28
Electrical resistivity $\rho_{el} = \sigma^{-1}$, μm	$1.33 \cdot 10^{-6}$
Surface tension γ, N/m	1.943

Due to limited penetration depth of magnetic field in the liquid material (10 mm), the whole 20 mm workpiece was modelled with material model for AISI 304 steel.

Numerical results. The temperature as well as velocity distributions are shown in Figure 3 for the case of optimal compensation of hydrostatic pressure in the melt. The welding speed was 0.4 m/min and oscillation frequency —

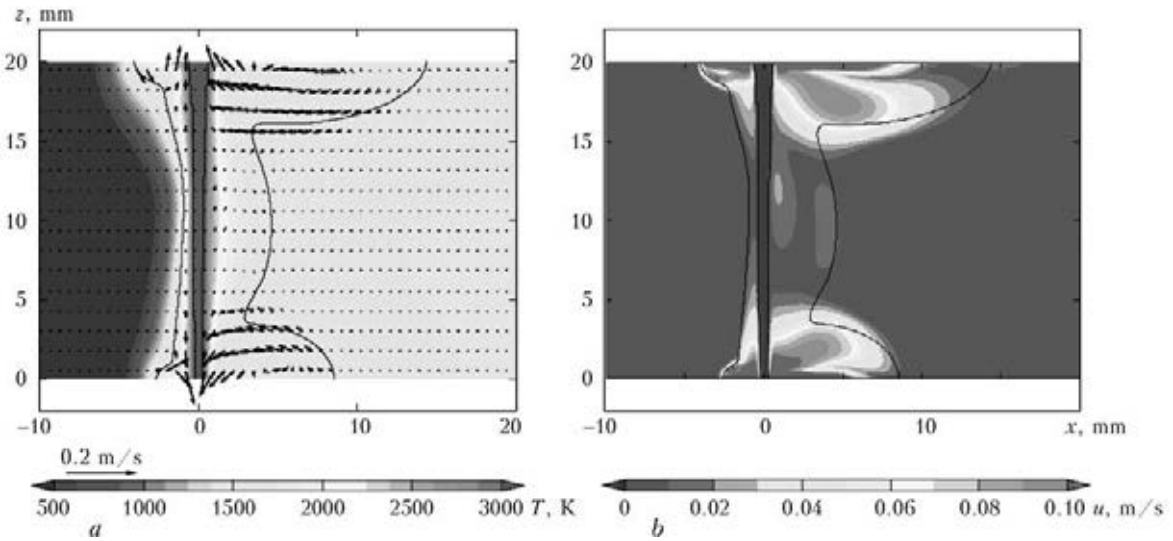

Figure 3. Symmetry plane of simulation results for case with optimal electromagnetic control of the hydrostatic pressure at welding speed of 0.4 m/min: *a* — temperature distribution and velocity vectors; *b* — velocity magnitude distribution

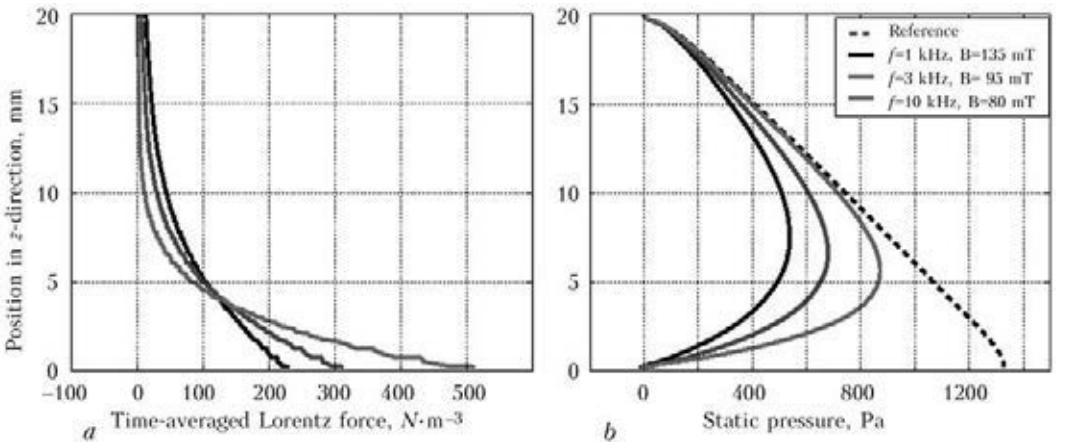

Figure 4. Pressure distribution 3 mm behind the keyhole in vertical axis (*a*), and time-averaged vertical component of the Lorentz force (*b*)

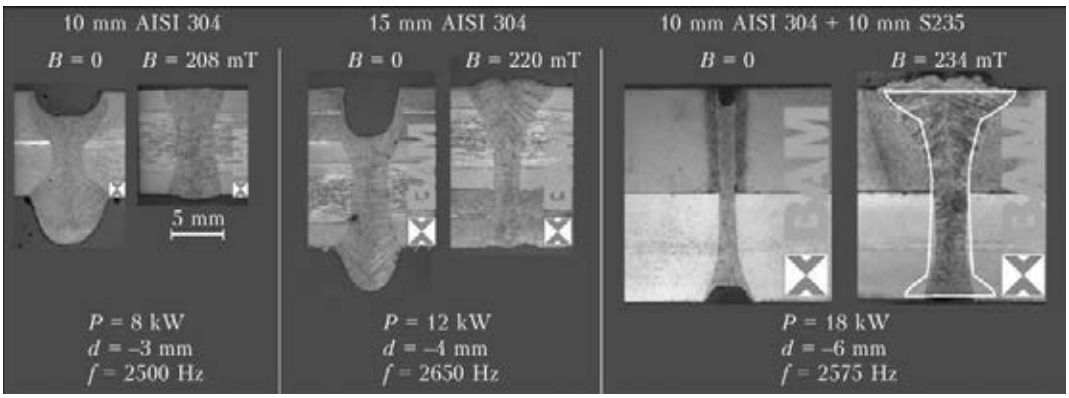

Figure 5. Single-pass laser welding without ($B = 0$) and with ($B \neq 0$) optimal parameters of the electromagnetic support system for 10–20 mm thickness at 0.4 m/min welding speed. Laser power P and focus depth d were adapted with respect to plate thickness; for 20 mm thickness the simulational cross section is overlayed at 95 mT and 3 kHz

3 kHz that leads to penetration depth of the magnetic field of around 10 mm in the liquid phase of material. The peak u values in the regions near the free surfaces of weld pool are due to the Marangoni flow directed from hot to cold regions as the surface tension increases along that path. Therefore, the bead is elongated at both surfaces. At the lower surface, this elongation is smaller due to presumed geometry of keyhole with smaller diameter at the lower side.

Figure 4, *a* shows the hydrostatic pressure compensation in the weld 3 mm behind the keyhole in symmetry plane for three values of frequencies. It shows that pressure values at both surfaces are nearly equal, so that dropping of melt cannot occur due to gravity effects, and calculated pressure distribution corresponds well with vertical component of the Lorentz force (Figure 4, *b*).

Experimental results. The experimental results for thicknesses between 10 mm and 20 mm are shown in Figure 5. Up to 15 mm, the material AISI 304 was used; for 20 mm — combination of steels AISI 304 (lower side) and S235 (upper side) was used, due to stability issues of welding process at the upper weld pool side and the higher surface tension of structural steel. Up to thickness of 15 mm, the reference cases show severe sagging of material, whereas the case of 20 mm is associated with unstable welding process and material loss on root and top side. The magnetic flux density needed to avoid sagging increases slightly with higher material thicknesses, and a state of optimal compensation can be reached for any thickness. The cross sections of simulation with $B = 95$ mT at 3 kHz oscillation frequency corresponds well with experiment (234 mT and 2.6 kHz).

Conclusion

Electromagnetic weld pool support was successfully applied for up to 20 mm thickness stainless steel, and severe sagging of liquid material could be prevented. The simulations show smaller value of the magnetic flux density for compensation of hydrostatic pressure. Only slight increase of magnetic field in the experiments for different thicknesses allows for speculations about a further effect, that must be compensated for, e.g. other dynamic oscillatory processes in the melt associated with the vapor phase in keyhole and corresponding reaction forces or even the influence of weakly ferromagnetic properties of the material, especially in the light of the exact predictions for magnetic flux density for aluminium alloy AlMg3 [12].

Acknowledgements. *Financial funding of the Deutsche Forschungsgemeinschaft DFG (Bonn, Germany) under Grant No. DFG GU 1211/2-1 is gratefully acknowledged.*

1. Avilov, V. et al. (2012) *Sci. and Technol. of Welding and Joining*, **17**, 128–133.
2. Vollertsen, F. et al. (2010) *Welding in the World*, **54**, 62–70.
3. Ready, J.F. et al. (2001) *LIA Handbook of Laser Materials Processing*.
4. Sanderson, A. et al. (2000) *Fusion Eng. Des.*, **49/50**, 77–87.
5. Kohyama, A. et al. (1984) *J. Nucl. Mater.*, **122**, 772–776.
6. Kawahito, Y. et al. (2009) *Sci. and Technol. of Welding and Joining*, **14**, 288–294.
7. Shin, M. et al. (2010) *Transact. of JWRI*, **39**, 33–38.
8. Schneider, A. et al. (2013) *Phys. Proc.*, **41**, 4–11.
9. Vollertsen, F. et al. (2006) *J. Laser Appl.*, **18**, 28–34.
10. Avilov, V.V. et al. (2009) *Proc. of EPM* (2009, Dresden, Germany).
11. Avilov, V.V. et al. (2012) *Sci. and Technol. of Welding and Joining*, **17**, 128–133.
12. Bachmann, M. et al. (2012) *J. Phys: Appl. Phys. D*, **45**, 13.
13. Gatzen, M. et al. (2009) *Proc. of LAMP*.
14. Velde, O. et al. (2001) *Int. J. Heat Mass Transfer*, **44**, 2751–2762.
15. Sahoo, P. et al. (1988) *Metall. and Mat. Transact. B*, **19**, 483–491.
16. Mills, K.C. (2002) *Recommended values of thermophysical properties for selected commercial alloys*. Woodhead Publ.
17. Wilthan, B. et al. (2008) *Int. J. Thermophys.*, **29**, 434–444.

Received 10.01.2014

DETONATION COATINGS OF COMPOSITE POWDER OF FERROMOLYBDENUM–SILICON CARBIDE PRODUCED USING METHOD OF MECHANICAL-AND-CHEMICAL SYNTHESIS

Yu.S. BORISOV, A.L. BORISOVA, E.A. ASTAKHOV, A.N. BURLACHENKO, Z.G. IPATOVA and **V.F. GORBAN**

[1]E.O. Paton Electric Welding Institute, NASU
11 Bozhenko Str., 03680, Kiev, Ukraine. E-mail: office@paton.kiev.ua
[2]I.N. Frantsevich Institute of Problems of Materials Science, NASU
3 Krzhizhanovsky Str., 03680, Kiev, Ukraine. E-mail:epp@ipms.kiev.ua

Investigation of formation of particles of composite powder in the process of mechanical-and-chemical synthesis at processing of mixture of powders of ferromolybdenum and silicon carbide in planetary mill was carried out. It was established that as a result of this process the formation of molybdenum carbide and also silicides of iron and molybdenum with increase of average microhardness of particles from 7270 to 10,520 MPa is occurred. The produced powders are used for detonation spraying of coatings. The properties of coatings of powder FeMo and composite powder FeMo–SiC were investigated using methods of metallography, X-ray diffraction phase analysis, microindenting, and their resistance to wear and corrosion was measured. Basing on the results of microindenting it was established that the complex of mechanical characteristics (H_{IT}, E, ε_{el}, σ_{el}) of detonation coating of composite powder FeMo–SiC exceeds as to its level the same data for the coating of powder FeMo, and values H_{IT}/E^* and H^3_{IT}/E^{*2}, used for evaluation of wear resistance, allow predicting increased resistance to wear for the coating FeMo–SiC as compared to the coating FeMo. The application of map of types of structural states of material, basing on the ratio of values of H_{IT} and ε_{el}, allowed evaluating the state of coating of composite powder FeMo–SiC as micro-nanostructured one. The measurements of wear and corrosion resistance of detonation coating of FeMo–SiC as compared both to FeMo coating and also detonation coating of mixture of powders NiCrBSi–WC (according to wear resistance) and of galvanic chromium (according to corrosion resistance) showed considerable advantage of the first ones. The reasons for such increase of functional properties in detonation coating of composite powder FeMo–SiC should be attributed to the presence of sprayed particles of products of mechanical-and-chemical synthesis, in particular of silicide phases, and high dispersity of formed structure of coatings. 14 Ref., 5 Tables, 10 Figures.

Keywords: *detonation spraying, coating, composite powder, mechanical-and-chemical synthesis, ferromolybdenum, silicon carbide, phase composition, microhardness, microindenting, mechanical properties, micronanostrucutred state, wear resistance, electrochemical characteristics*

One of the ways of modern development of thermal spraying is the development of technology of deposition of coatings with composite structure possessing increased functional properties according to the purpose of their application. Often this problem is solved using spraying of composite powders (CP) produced using different methods, in particular, cladding, conglomeration with further sintering, and using technology of self-spreading high-temperature synthesis [1, 2].

Basing on the results of investigations of the process of interaction of transition metals (Cr, Ti) and non-metallic refractory compounds (SiC, B_4C, Si_3N_4) [3–6] a number of CP compositions of for thermal spraying of coatings was developed, where during heating under the conditions of plasma jet the exothermal reaction of interaction with formation of carbides, borides, nitrides and silicide matrix (in case SiC and Si_3N_4) is proceeding. The produced coatings demonstrated high resistance to wear [4].

The further step in the development of this trend of creation of CP, designed for deposition of coatings with high functional properties, is the application as metallic component at ineraction with non-metallic refractory compound of different ferroalloys (FeTi, FeV) [7–9]. To form CP the conglomeration of mechanic mixture of powders with the following sintering was used. The results of investigation of wear resistance of coatings produced of these powders using meth-

© Yu.S. BORISOV, A.L. BORISOVA, E.A. ASTAKHOV, A.N. BURLACHENKO, Z.G. IPATOVA and V.F. GORBAN, 2014

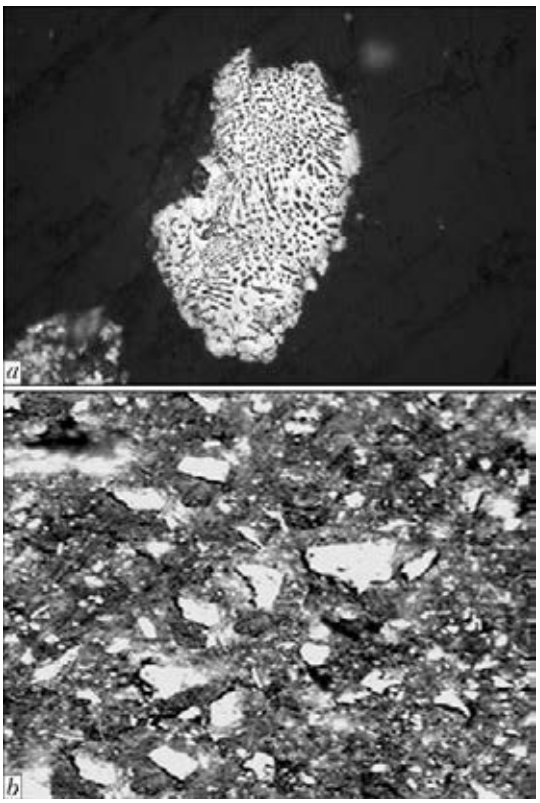

Figure 1. Microstructure (×500) of particles of initial powders: *a* — FeMo; *b* — SiC

ods of plasma and detonation spraying proved the efficiency of development of this trend [9].

In the present work the results of investigation of process of formation of CP particles of mixture of ferroalloy FeMo and SiC using method of mechanical-and-chemical synthesis (MCS) [10], having wide challenges in the field of development of saving and efficient technology of CP production, and also study of structure and properties of detonation coatings of FeMo–SiC CP are given.

Methods of experiment. As the initial materials for producing of FeMo–SiC CP the alloy of ferromolybdenum (GOST 4759–91), which was crushed to the size of particles of not more than 100 μm, and silicon carbide (GOST 3647–71) with the size of particles of not more than 3 μm, were used.

Table 1. Thermodynamic activity of process of synthesis of products of the most probable reactions in FeMo–SiC system

Reaction	SiC, wt.%	ΔH^0_{298}, kJ/mole	ΔT_{ad}, K
$5Mo + SiC = Mo_2C + Mo_3Si$	7.7	−85.02	342
$3Fe + SiC = Fe_3Si + C$	19.0	−27.98	167

The composition of initial mixture was selected basing on the thermodynamic evaluation of possible reactions of silicon carbide with molybdenum and iron. The calculations showed that in interaction of SiC with iron the reaction of formation of iron silicide (Fe_3Si) is most probable from the thermodynamic aspect with precipitation of free carbon, while in interaction of SiC with molybdenum the reaction of formation of mixture of molybdenum carbide (Mo_2C) with molybdenum silicide (Mo_3Si) is probable. These reactions are characterized by maximum values of heat effect and adiabatic increase of temperature (Table 1).

As the ferromolybdenum contained 65 wt.% Mo and 35 wt.% Fe, then according to the calculation it is necessary to add 11.65 wt.% SiC to the mixture for full running of above-mentioned reactions.

The process of MCS of mixture of powders of the mentioned composition was performed using planetary mill «Aktivator-2S» in the air environment at the speeds of drum rotation of 1500 rpm, ratio of mass of balls to the mass of charge was 10:1 during the period of 0.5–5.0 h. In the MCS process after 0.5, 1.5, 3 and 5 h of treatment the samples were taken for investigation of phase composition of mixture, hardness, size and shape of particles.

Detonation coatings were sprayed on steel specimens in the installation «Perun-S» at the consumptions, m^3/h: propane–butane — 0.5,

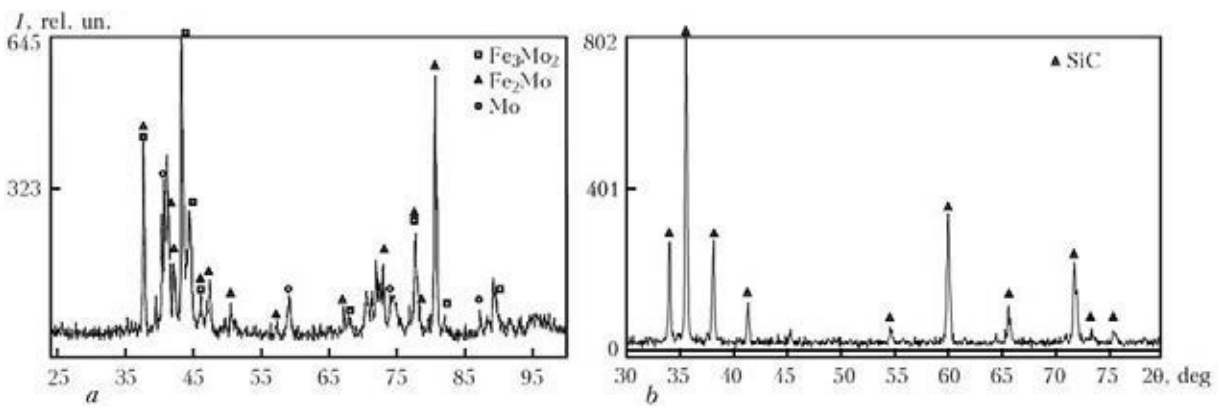

Figure 2. X-ray photographs of initial powders: *a* — FeMo; *b* — SiC

oxygen — 1.3, air — 0.65, air for transportation of powder — 0.12, and spraying distance of 100 mm.

CP and sprayed coatings were investigated using methods of metallographic analysis, X-ray diffraction phase analysis (X-ray DPA) (installation DRON-UM-1, radiation CuK_α, monochromatized), microdurometric analysis (at indenter load of 25 g for powders and 50 g for coatings) and also microindenting (of coatings only).

Microindenting was carried out in the installation «Micron-gamma» at room temperature (loading in the range of up to F = 2 N) using Berkovich diamond pyramid at the sharpening angle of 65° at automatically performed loads and unloads during 30 s. Simultaneously, the record of diagram of loading, holding and unload in the coordinates F–h was carried out. Accuracy of determination of force F amounted to 10^{-3} N, depth of penetration of indenter h was ±2.5 nm. Values of diagram F, h_{max}, h_{res}, h_c were fixed according to the data of 2,000 points on the diagram of indenting [11]. Calculation of such characteristics of material as hardness H_{IT}, contact modulus of elasticity E^* was carried out according to the standard ISO 14577-1:2002(E).

Wear under the conditions of dry friction of sliding was investigated in the friction machine M-22M, where it was possible to measure simultaneously the coefficient of friction, wear of

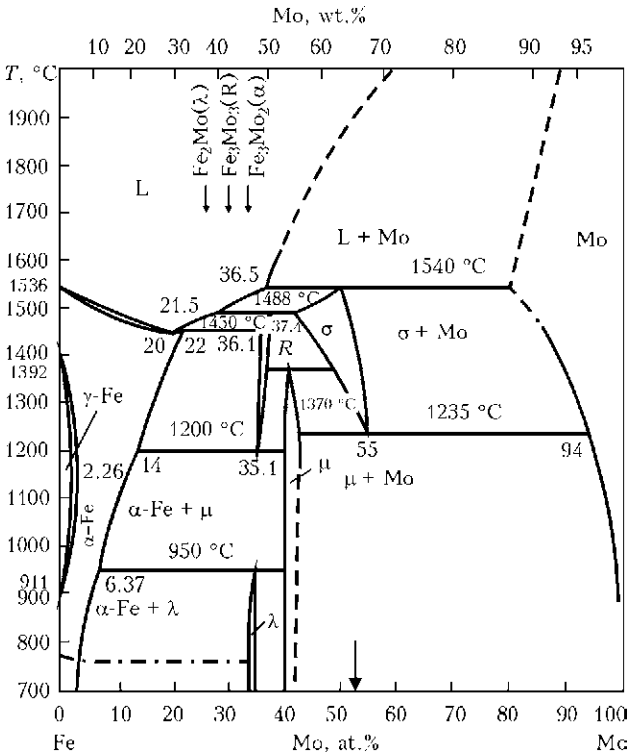

Figure 3. Constitutional diagram of FeMo systems (arrow indicates the composition of alloy)

specimen with coating and temperature in the contact zone. The coating was deposited on the insert of steel 45, the shaft of hardened steel 45 (*HRC* 55–58) served as a mating body. The tests were carried out at the loading of 2 MPa and

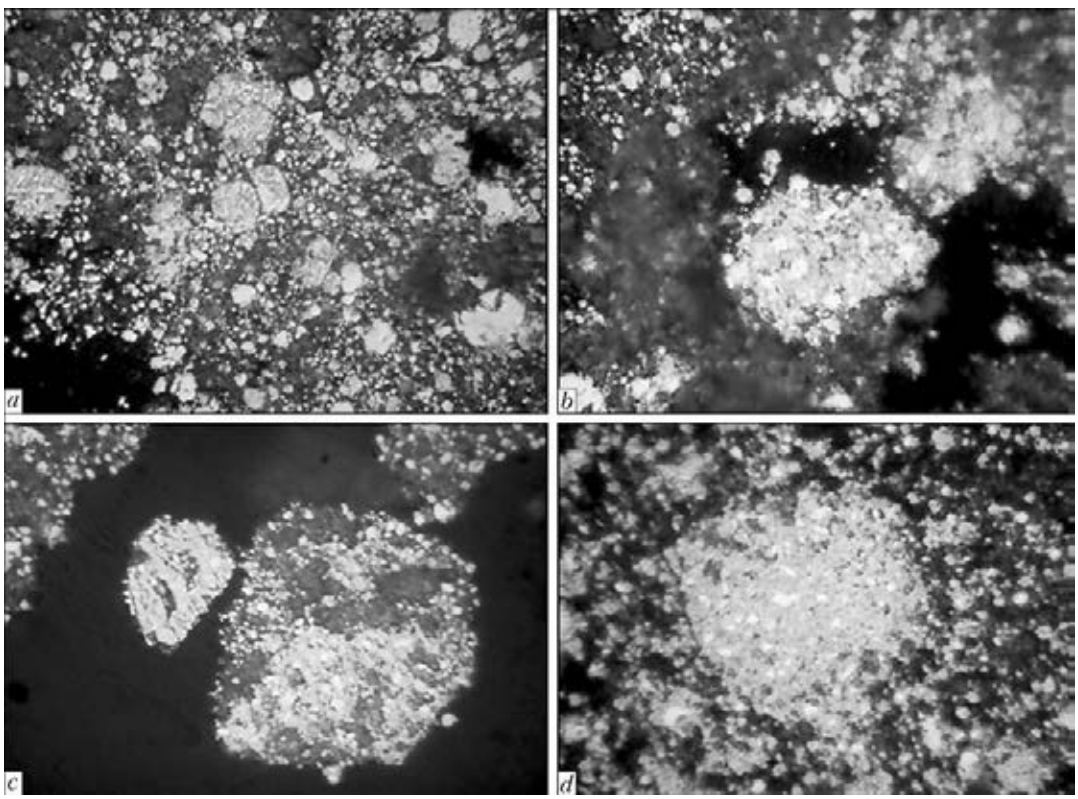

Figure 4. Microstructure (×1000) of powder particles of FeMo–SiC system produced using MCS method at different duration of treatment: *a* — 0.5; *b* — 1.5; *c* — 3; *d* — 5 h; etched

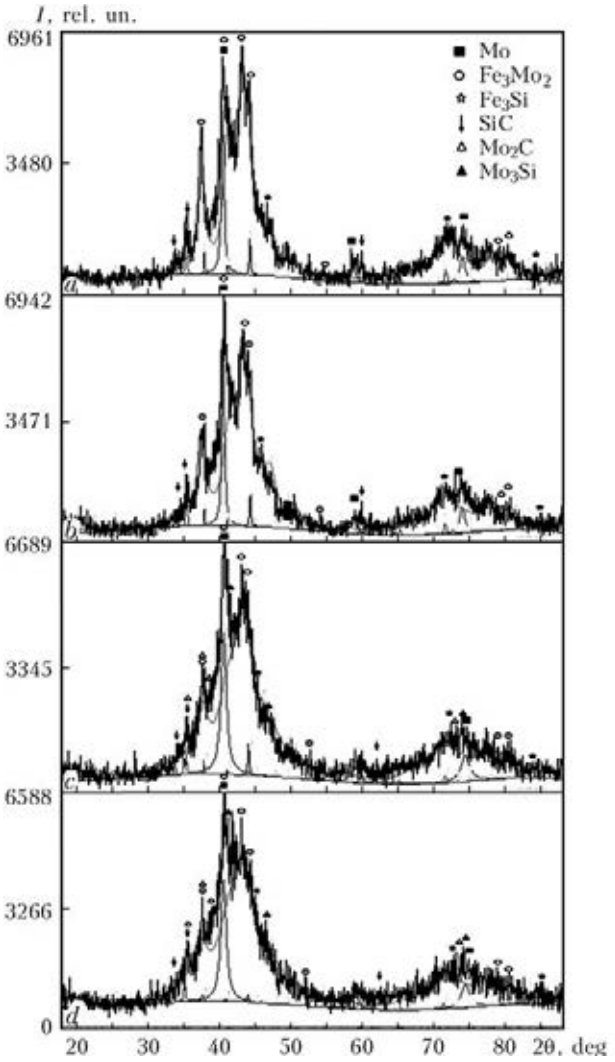

Figure 5. X-ray photographs of powder particles of FeMo–SiC system depending on duration of MCS: *a* — 0.5; *b* — 1.5; *c* — 3; *d* — 5 h

speed of sliding of 5 m/s. The path of sliding was 4 and 5 km.

Corrosion resistance of coatings in sea water and 10 % solution of H_2SO_4 was investigated using method of measurement of polarization potential in the potential controlling device P-5827M using three-electrode cell YaSE-2.

Experiment results. During investigation of structure and phase composition of initial powders (Figures 1 and 2) it was established that ferromolybdenum, containing 65 wt.% Mo according to GOST 4759–91, consists of molybdenum Fe_3Mo_2 (μ-phase), and silicon carbide only of α-SiC, as is followed from the equilibrium constitutional diagram (Figure 3).

In the process of MCS of powder mixture FeMo + 11.65 wt.% SiC at the initial stage (0.5 h) the refining of metallic particles FeMo with embedding of fine-dispersed particles of initial silicon carbide to them is observed (Figure 4, *a*). Further on, the formation of composite particles composed of initial components (Figure 4, *b*) and also products of their chemical interaction (Figure 4, *c*, *d*) is occurred. On the X-ray photographs of samples of powders taken from the reactor in the process of MCS, due to a high level of their cold working, on the background of halo, which evidences of high level of amorphisation of particles, one can detect only single X-ray lines of initial phases (Fe_3Mo_2, SiC) and products of their interaction (Mo_2C, Mo_3Si and Fe_3Si) (Figure 5), formation of which was supposed according (see Table 1) to the thermodynamic evaluation of possible reactions of molybdenum and iron with SiC.

Microhardness of particles of FeMo–SiC CP with increase of duration of MCS grows monotonously reaching 10,520–1720 MPa at the period of treatment of mixture of 5 h (Table 2). At variation curves of microhardness two maximums are observed, which signify two the most obvious and characteristic values of hardness of particles (Figure 6). It is characteristic that with increase of duration of MCS both maximums and also the average value of microhardness of particles move to the region of the higher values.

For detonation spraying of coatings the FeMo–SiC CP, produced by MCS at the time of processing of 5 h, and the powder of ferromolybdenum with the size of particles of not more than 63 μm, were used for comparison. In both cases the dense, thin lamellar coatings with oxide sublayers at the boundaries of lamellas and small number of round metallic particles are formed. Defects and delaminations of coatings at the

Table 2. Phase composition and microhardness of CP of FeMo–SiC system depending on MCS duration

Duration of MCS, h	Phase composition	Microhardness, MPa	
		Average	Most probable
Initial	Fe_3Mo_2, Mo, SiC	7270 ± 1870 (FeMo), 27200 (SiC) [12]	–
0.5	Fe_3Mo_2, Mo, SiC, amorphous phase	7950 ± 1760	6375, 11125
1.5	Fe_3Mo_2, Mo, SiC, amorphous phase	8710 ± 2230	7750, 11250
3.0	Fe_3Mo_2, Mo, Mo_2C, Mo_3Si, Fe_3Si, SiC, amorphous phase	10090 ± 1530	8900, 11300
5.0	Fe_3Mo_2, Mo, Mo_2C, Mo_3Si, Fe_3Si, SiC, amorphous phase	10520 ± 1720	9700, 11750

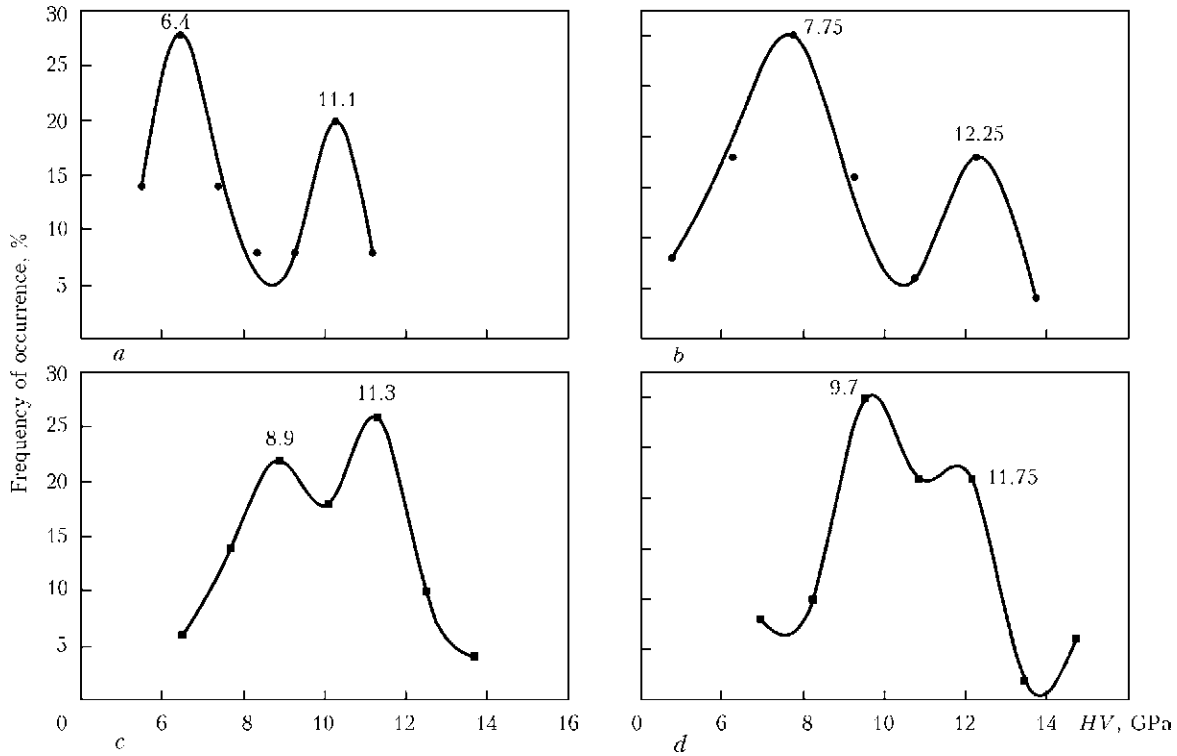

Figure 6. Variation curves of microhardness of CP particles of FeMo–SiC system depending on the duration of MCS: *a* — 0.5; *b* — 1.5; *c* — 3; *d* — 5 h

boundary with the base were not observed (Figure 7).

According to the results of X-ray DPA, the complex oxide Fe_2MoO_4 was revealed in the coating of ferromolybdenum except the basic phase of initial powder, while in the coating of FeMo–SiC CP, except the phases included into the composition of initial powder, the same oxide Fe_2MoO_4 and disilicide of molybdenum $MoSi_2$ were revealed (Figure 8). It can evidence about active proceeding of interfacial interaction of CP components under the conditions of detonation spraying, all the more the traces of SiC in the coating were not detected.

The mechanical characteristics of coatings of powders of ferroalloy FeMo (with content of 65 wt.% Mo) and products of MCS in the mixture FeMo–SiC were investigated using method of microindenting (Figure 9).

According to the modern existing point of view in evaluating the surface of resistance to wear it is necessary to consider not only the value of its hardness, but also to the same extent the modulus of elasticity of its material. Therefore, at the present time the ratio H/E is used as the characteristic of wear resistance of surface [13].

At the same time, the behavior of coatings in the process of wear depends on the level of its resistance to plastic deformation, which is proportional to the value of ratio H^3/E^2 [13]. Therefore, the above-mentioned characteristics of mechanical properties of materials and coatings, determined as a result of application of method of

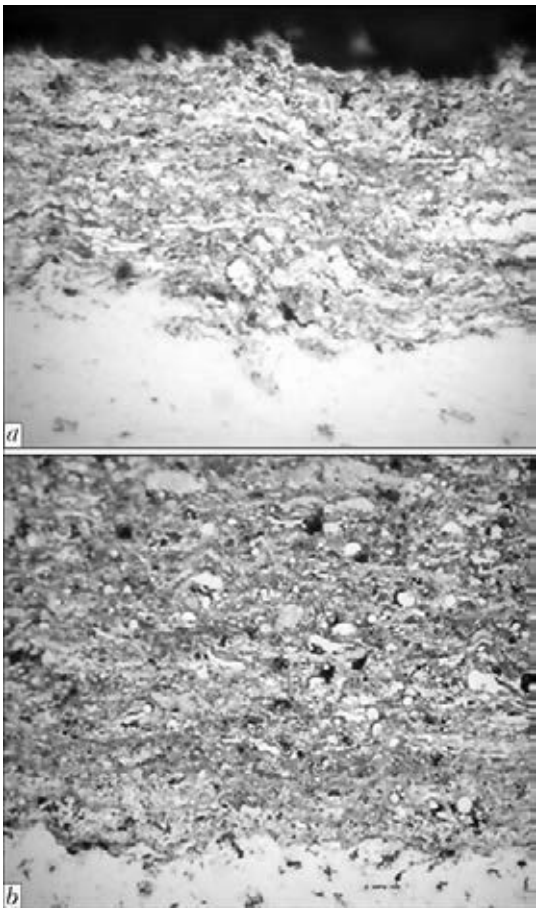

Figure 7. Microstructure (×400) of detonation coatings of ferromolybdenum (*a*) and FeMo–SiC CP (*b*)

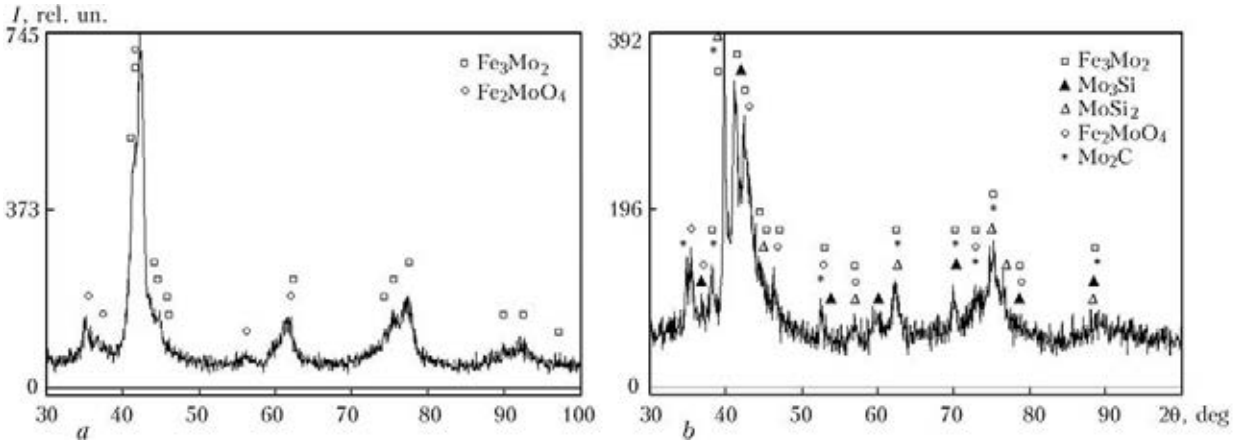

Figure 8. X-ray photographs of detonation coatings of powder FeMo (*a*) and FeMo–SiC CP (*b*)

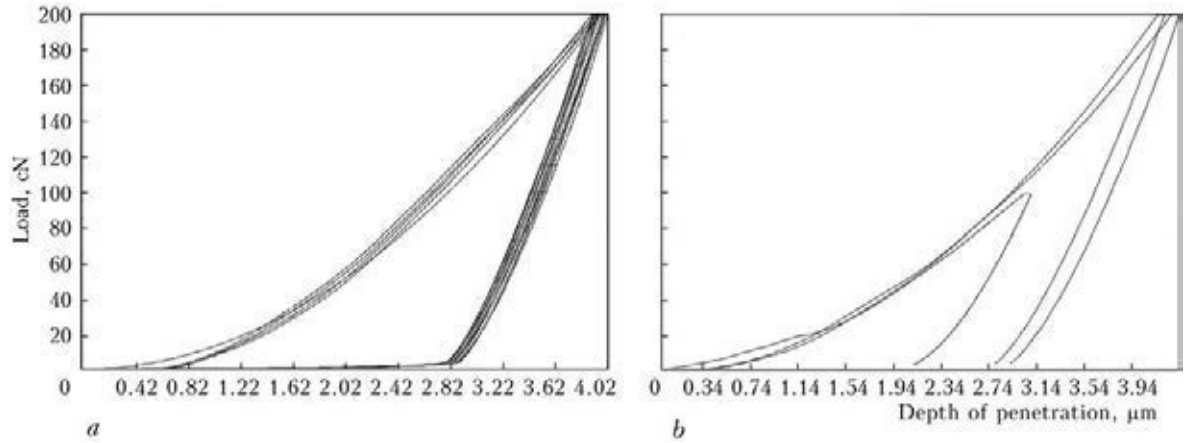

Figure 9. Diagram of detonation coatings of powder of ferroalloy FeMo (*a*) and FeMo–SiC CP (*b*) obtained using microindenting

nano- (or micro-) indenting, are used as the criteria of their wear resistance [13, 14]. As the generalization of results of measurements of these characteristics for a wide range of materials and coatings showed, their value depends both on the composition as well as on the structural state of material of surface (single- and coarse-crystalline, fine and nanocrystalline, amorphous and amorphous-nanocrystalline) [11].

Coming from the above-mentioned, for evaluation of wear resistance of coatings FeMo–SiC the parameters H_{IT}/E^* and H_{IT}^3/E^{*2} were added to the obtained data of microindenting, presented in Table 3.

The analysis of results of microindenting shows that coating, produced of CP of the system FeMo–SiC, has higher values of wear resistance than the coating produced of the powder FeMo. Thus, parameters H/E^* grow from 0.066 to 0.080

Table 3. Results of microindenting of detonation coatings of FeMo–SiC system

Characteristic of microindenting	Composition of sprayed powders	
	Ferroalloy FeMo (65 wt.% Mo)	Product of MCS FeMo (65 wt.% Mo) + SiC
Maximum depth of penetration of indenter h_{max}, μm	3.934	3.575
Contact depth of penetration of indenter h_c, μm	3.256	2.856
Hardness at indenting of H_{IT}, GPa, in the dent contact region of depth h_c	7.7 ± 3	10.3 ± 25
Contact modulus of elasticity E^*, GPa	115.0	127.6
H_{IT}/E^*	0.066	0.080
H_{IT}^3/E^{*2}	0.0345	0.0670
Relative out-of-contact elastic strain ε_{el}, %	2.04	2.47
Stress of out-of-contact elastic strain ε_{el}, GPa	2.5	3.16

and H_{IT}^3/E^{*2} — from 0.0345 to 0.0670. Growth of parameters ε_{el} and σ_{el} (from 2.04 to 2.47 and from 2.50 to 3.16, respectively) evidence also of improvement of ductile properties of CP coating of the system FeMo–SiC, as compared to the coating of pure ferroalloy FeMo, in particular increase of its resistance to abrasive wear. Besides, the combination of simultaneous growth of H_{IT} and ε_{el} at consideration of map of types of structural states of materials, suggested by the authors of work [11], can evidence of shifting the structure of coating from CP of the system FeMo–SiC (as compared to the FeMo coating) to the region of nanocomposite one containing micro- and nanodimensional phases (Figure 10). This is confirmed also by X-ray photographs of coatings (see Figure 8), where larger widening of peaks in case of coating of FeMo–SiC CP is observed.

To evaluate the functional properties of produced FeMo–SiC-coating the measurement of its tribotechnical and electrochemical characteristics was carried out. In Table 4 the results of determination of linear wear and coefficient of friction of investigated detonation coatings under the conditions of dry friction on the path of 4 km at loading of 2 MPa, as compared to detonation coating of mechanical mixture NiCrBSi-PG-10N-01 + WC (63/35) alloy and steel 45 with *HRC* 55–58, are given. As we see, in detonation coating of FeMo–SiC CP the resistance to wear under the conditions of dry friction is 5–10 times higher than for FeMo alloy coating, 2.5–5 times higher than for coating of powder containing 65 wt.% of nickel self-fluxing alloy PG-10N-01 in mixture with 35 wt.% WC, and 35–75 times higher than that of steel 45. The coefficient of friction in this case is maintained

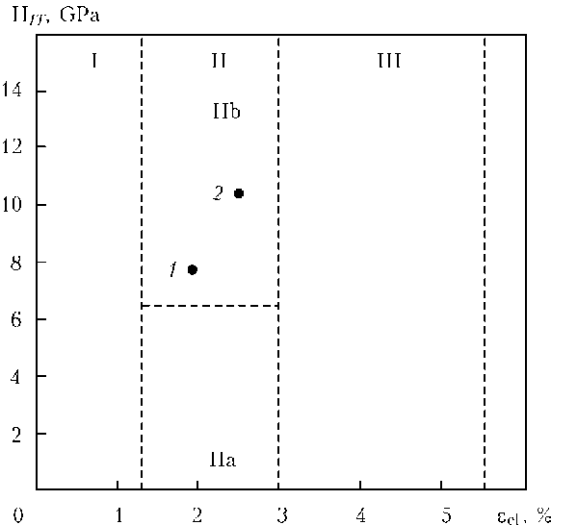

Figure 10. Map of types of structural state of materials [11]: I — coarse-crystalline; IIa — fine-crystalline; IIb — nanocrystalline; III — amorphous-nanocrystalline; *1* — FeMo; *2* — FeMo–SiC CP coating

at the level of 0.6–0.7. These results coincide with high wear resistance of coating of FeMo–SiC CP predicted above based on the values H_{IT}/E^* and H_{IT}^3/E^{*2}, and obviously connected both with its structural state and also with phase composition.

The results of measurement of electrochemical characteristics of coatings, given in Table 5, evidence of high corrosion resistance of detonation coating of FeMo–SiC CP not only as compared to FeMo-coating but also to galvanic chromium coating.

The estimated rate of corrosion of detonation coating of FeMo–SiC CP in sea water amounts to 0.077 against 0.1 and 0.18 mm/year for FeMo coating and galvanic chromium one. According to this fact the service life of protective coating 0.5 mm thick is equal to 6.7, 4.8 and 4.5 years for coatings of FeMo–SiC CP, FeMo and galvanic chromium, respectively. The reasons of

Table 4. Linear wear and coefficient of friction of detonation coatings

Material of coating	Method of preparation of powder	Linear wear, μm/km	Friction coefficient
FeMo	Refined alloy	20	0.6
FeMo–11.65SiC CP	MCS	2–4	0.6–0.7
PG-10H-01 + WC	Mechanical mixture (65/35)	11	0.6
Steel 45	–	145	0.72

Table 5. Electrochemical characteristics of detonation coatings in different testing environment

Material of coating	10 % H_2SO_4 water solution		Sea water	
	Corrosion potential E, V	Rate of corrosion $i \cdot 10^5$, A/cm^2	Corrosion potential E, V	Rate of corrosion $i \cdot 10^6$, A/cm^2
FeMo	–0.20	6.4	–0.32	9.2
FeMo–11.65SiC CP (MCS)	–0.12	3.6	–0.32	5.0
Galvanic chromium	–0.12	720	–0.18	9.6

such increase of corrosion resistance should be attributed to appearance of silicide phases in the coating, and also, probably, to the peculiarities of structural state of detonation coating of FeMo–SiC CP.

Conclusions

1. As a result of MCS process proceeding during 5 h in the planetary mill, the CP particles are formed of mixture of powders of ferroalloy FeMo and SiC containing, except of Fe_3Mo_2 and Mo, the products of synthesis in the form of Mo_2C, Mo_3Si and Fe_3Si. Here, the average microhardness of particles on the base of FeMo is increased from 7270 to 10,520 MPa.

2. Using powders FeMo–SiC with size of particles of less than 63 μm for detonation spraying the dense coatings were produced containing phases $MoSi_2$ and Fe_2MoO_4 with features of amorphisation of coating, except of phase components of initial powder.

3. Using method of microindenting the measurement of mechanical characteristics of coatings of FeMo and FeMo–SiC CP was carried out. It was found that coating of products of MCS of FeMo–SiC possesses a complex of properties described by the criteria H_{IT}/E^* and H^3_{IT}/E^{*2}, the values of which allow predicting its increased wear resistance as compared to FeMo coating (respectively, for the coatings of FeMo and FeMo–SiC CP H_{IT}/E^* is equal to 0.066 and 0.080, H^3_{IT}/E^{*2} is 0.0345 and 0.0670).

4. The analysis of nature of structure of coatings using the map of types of structural states showed that in case of application of FeMo–SiC CP produced by MCS for detonation spraying, the coating according to its mechanical characteristics lies in the region of micronanostructured state.

5. During investigation of tribotechnical and electrochemical characteristics of detonation coatings of powders FeMo and FeMo–SiC CP it was established that coatings, produced of MCS products FeMo–SiC, have higher wear (under the conditions of dry friction) and corrosion resistance (in 10 % H_2SO_4 solution and sea water) than FeMo coating, and also coating of mixture PG-10N-01 with WC (in case of wear) and of galvanic chromium (under the conditions of corrosion effect). The reasons for this fact are the formation of silicide phases in the coatings and also increased dispersity of their structure.

1. Kulik, A.Ya., Borisov, Yu.S., Mnukhin, A.S. et al. (1985) *Thermal spraying of composite powders*. Leningrad: Mashinostroenie.
2. Borisova, A.L., Borisov, Yu.S. (2008) Application of processes of self-propagated high-temperature synthesis in technology of thermal spraying of coatings. *Poroshk. Metallurgiya*, **1/2**, 105–125.
3. Borisova, A.L., Borisov, Yu.S., Shvedova, L.K. et al. (1979) Interaction in Cr–SiC system in conditions of conventional and plasma heating. *Ibid*., **10**, 79–84.
4. Borisova, A.L., Borisov, Yu.S., Polyanin, B.A. et al. (1985) Interaction in Ti–SiC composite powders and properties of sprayed coatings. *Ibid*., **10**, 92–96.
5. Borisov, Yu.S., Borisova, A.L., Adeeva, L.I. et al. (1995) Composite plasma coatings Ti–Si–C. *Problemy Spets. Elektrometallurgii*, **3**, 62–70.
6. Borisov, Yu.S., Borisova, A.L., Shvedova, L.K. (1986) Transition metal–nonmetallic refractory compounds composite powders for thermal spraying. In: *Proc. of ITSC on Advances in Thermal Spraying* (Montreal, Canada, Sept. 8–12, 1986). Pergamon Press, 323–332.
7. Grigorenko, G.M., Borisova, A.L., Borisov, Yu.S. et al. (2002) Investigation of interphase interaction of ferrotitanium with silicon carbide in powder mixtures used for thermal spray coating. *Advances in Electrometallurgy*, **4**, 30–33.
8. Grigorenko, G.M., Borisova, A.L., Borisov, Yu.S. et al. (2003) Investigation of interphase interaction of ferrotitanium with boron carbide in powder mixtures for deposition of thermal coatings. *Ibid*., **1**, 26–29.
9. Murashov, A.P., Astakhov, E.A., Demianov, I.A. et al. (2003) Wear resistance of thermal coatings produced from composite powders «ferroalloys–B_4C, SiC. *The Paton Welding J*., **7**, 43–44.
10. Lovshenko, G.F., Lovshenko, F.G., Khina, B.B. (2008) *Nanostructural mechanically alloyed materials on the base of metals*. Mogilyov: BRU.
11. Firstov, S.A., Gorban, V.F., Pechkovsky, E.P. (2009) *New method of treatment and analysis of results of automatic indentation of materials*. Kiev: Logos.
12. (1986) *Properties, production and application of refractory compounds*: Refer. Book. Ed. by T.Ya. Kosolapova. Moscow: Metallurgiya.
13. Leyland, A., Matthews, A. (2000) On the significance of the H/E ratio in wear control: A nanocomposite coating approach to optimized tribological behavior. *Wear*, **246**, 1–11.
14. Gorlenko, A.O., Shupikov, I.L., Topolyansky, P.A. et al. (2012) Modification of operating surfaces of parts by deposition of strengthening nanocoating. *Metalloobrabotka*, **2**, 31–36.

Received 16.12.2013

PROSPECTS FOR DEVELOPMENT OF LOAD-CARRYING ELEMENTS OF FREIGHT CAR BOGIE

O.V. MAKHNENKO, G.Yu. SAPRYKINA, I.V. MIRZOV and **A.D. PUSTOVOJ**
E.O. Paton Electric Welding Institute, NASU
11 Bozhenko Str., 03680, Kiev, Ukraine. E-mail: office@paton.kiev.ua

In recent years accidents related to fracture of cast load-carrying elements of three-piece bogies of freight cars have become more frequent in the railways of Ukraine and Russia. The work substantiates the rationality of development and application of all-welded load-carrying elements of freight car bogie (FCB), improving their operational reliability. Welded structures of FCBs are widely applied in West Europe. Attempts to develop structures of all-welded elements of FCBs irreplaceable with cast structures are made in Ukraine and Russia. However, none of the developed welded structures is currently applied at regular cargo transportation, because of non-optimal design of bogie welded elements in terms of ensuring the required fatigue resistance margin. To develop a competitive welded solebar and bogie bolster it is, first of, all necessary to increase the fatigue resistance of bogie elements, improve the accuracy of solebar fabrication to avoid skewing of wheelset axles, leading to fast wear, lower their weight and cost, increase element run between scheduled depot repairs. Strength analysis of bogie welded elements should be performed in keeping with the norms currently in force, as well as current world standards, norms and recommendations, allowing for the most recent achievements in the field of dynamics of railway cars and methods to determine welded joint fatigue resistance. 20 Ref., 8 Figures.

Keywords: *welded structure, three-piece bogie of freight car, solebar, bogie bolster, solebar fracture, fatigue resistance*

In recent years accidents related to freight car bogie (FCB) fracture (Figure 1) have become more frequent in railway transportation. By the data of OJSC «RZhD» in 2011, 25 fractures of FCB solebars occurred, and in 2012, 23 accidents took place [1], by December 1, 2013, 37 cases of solebar fractures were recorded (Figure 2) with human casualties.

Analysis of operating reliability of cast structures of bogie solebar of 18-100 type freight car showed that fatigue crack initiation is the main cause for solebar failure [2], as the solebar of this bogie model does not have a sufficient margin of fatigue resistance and survivability [3]. Therefore, the task of improvement of its fatigue resistance is quite urgent. Large steel castings of FCB elements have several disadvantages of technological and design nature. Steel casting walls have a quite large scatter of thickness [4]. Moreover, casting has inherent defects such as pores, blowholes, etc., repair of which is labour-consuming [5].

Modern economic situation motivates manufacturers to look for an alternative to traditional cast elements of FCBs (solebars and bogie bolsters), the quality and reliability of which is not high enough. One of the optimum variants is

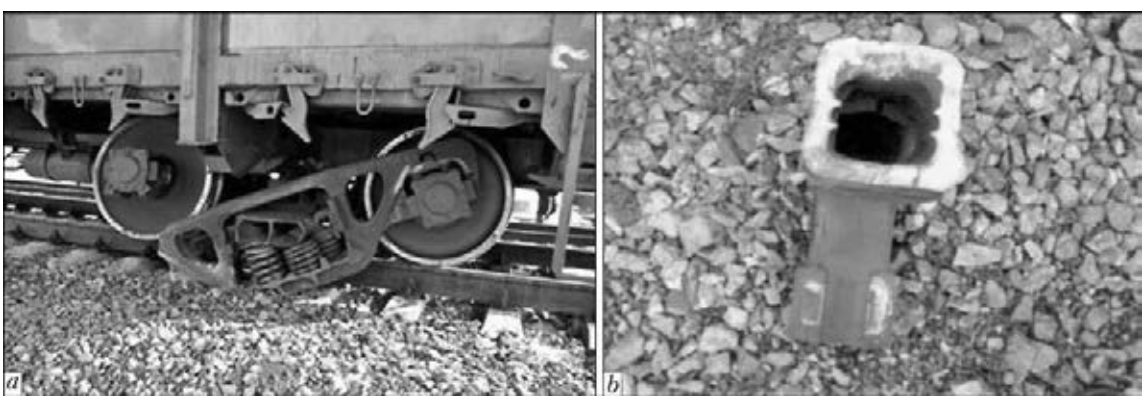

Figure 1. Fatigue fracture of cast structure of freight car solebar along R55 radius (*a*) and its fragment (*b*)

© O.V. MAKHNENKO, G.Yu. SAPRYKINA, I.V. MIRZOV and A.D. PUSTOVOJ, 2014

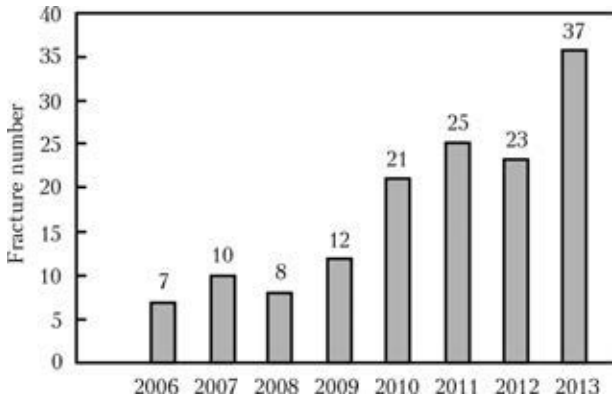

Figure 2. Dynamics of cases of solebar fracture in FCBs along R55 by years [1]

manufacture of the above parts by the technology of welding using rolled sheets.

Transition to all-welded structures of bogie elements can primarily ensure higher reliability of freight car structure, leading to lower number of operational failures and considerable reduction of the cost of unscheduled repair and reconditioning operations, respectively. Moreover, reduction of these elements mass by 5 to 10 % compared to cast variant can be achieved, that is a quite significant value in the overall freight traffic volume. In fabrication of solebar welded structure it is possible to ensure basic size accuracy within ±1 mm, that eliminates the possibility of wheelset axles skewing at bogie formation and will essentially reduce wheel wear for this reason. Putting bogie elements into production with application of welding technology is not so costly, compared to casting technology, and it can be implemented in practically any mechanical engineering plant, that can create the conditions for market saturation with quality elements of the bogie, namely solebar and bolster beam with improved fatigue resistance characteristics.

Known are different variants of welded structures of FCBs. In 2002, V.M. Bubnov Chief Specialized DB of Car Construction (GSKBV Ltd.) (Mariupol, Ukraine) together with SUE «NVTs Vagony» (St.-Petersburg) developed a welded structure of three-piece bogie of 18-1711 model with 25 tf axle load (Figure 3). However, the first test samples of solebars and bolster beams did not pass bench testing. With the assistance of PWI specialists bogie bolster design has been improved: fatigue resistance of its welded joints has been increased [7]. During performance of abbreviated accelerated tests of two test samples of bogie bolster for cyclic load, 30 mm long macrocrack was found in the first bolster at $2.745 \cdot 10^6$ load cycles, in the second bolster no fatigue macrocrack was found after $6 \cdot 10^6$ load cycles and testing was stopped. These tests showed that welded bolsters provide the required fatigue life, are not inferior to cast products in terms of strength and weight characteristics, and can be recommended for performance of the complete test cycle.

In 2004, OJSC «Kryukovsky Railway Car Building Works» (KVZ) (Kremenchug, Ukraine) developed a welded structure of FCB (Figure 4), in which solebars and bogie bolsters were made welded from rolled sheets of low-alloyed 09G2D or 09G2S steel (GOST 19281–89) of not lower than 295 strength class [8].

Development prototype was bogie of 18-100 model. It was anticipated that putting the devel-

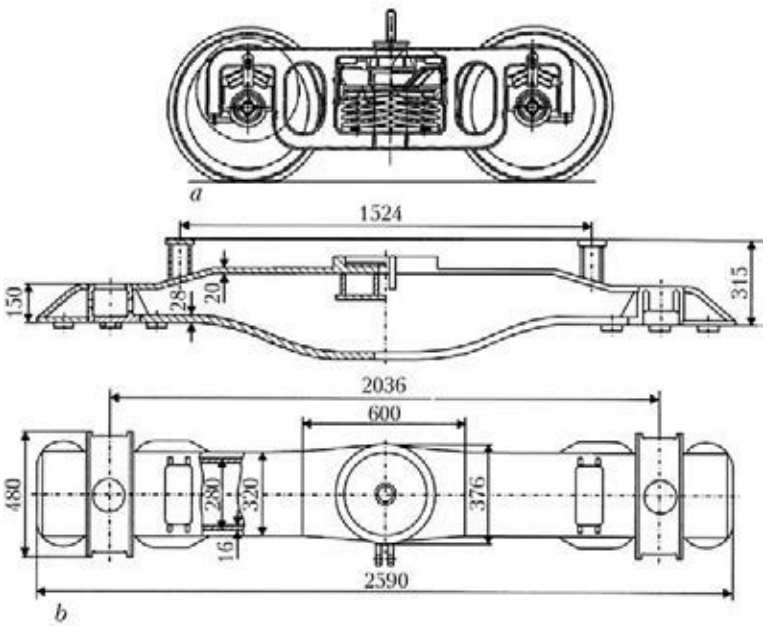

Figure 3. Schematics of welded structure of three-piece bogie of freight car developed by GSKBV together with company «Vagony» [6]: *a* — bogie from solebar side; *b* — bogie bolster developed with participation of PWI specialists

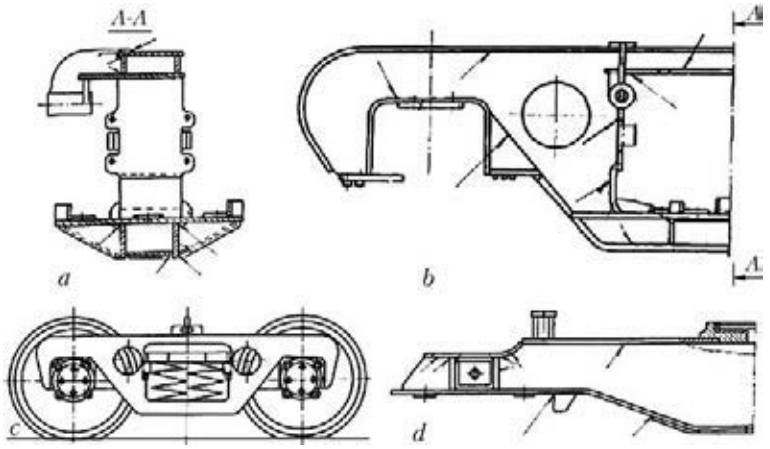

Figure 4. Schematic of welded structure of FCB of KVZ [8]: *a* — sectional view of solebar along the axis of symmetry; *b* — solebar; *c* — bogie; *d* — bogie bolster

oped design into production will improve the quality of large-sized parts of solebars and bogie bolsters and co-axiality of wheelsets in the bogie lower product cost, and reduce the dependence on casting suppliers.

In 2004, company «Vagony» and CJSC «Tver Institute for Car Construction» (TIV) (RF) developed the basic two-axle bogie of 18-9750 model of the typesize range with 25 tf static axle load (with the possibility of application for axle load of 23.5 tf), with welded structure of solebar and bogie bolster [9]. Its solebar (Figure 5) has closed box-like section along its entire length and consists of the upper and lower chords connected by an inclined chord. Note that widened form of spring opening allows a significant increase of rounding-off radii in its corners to lower stress concentration, as well as provides access for brake block examination.

In 2007, FSUE «F.E. Dzerzhinsky Uralvagonzavod» (Nizhny Tagil, RF) developed a stamp-welded variant of FCB [10]. Main load-carrying parts of box-like section (bogie bolster and solebar) are made of two parts, each of which is one stamped blank joined to its counterpart along a vertical longitudinal part plane (Figure 6).

However, despite a whole number of attempts to create in CIS territory welded structures of load-carrying elements of three-piece bogies of freight cars, irreplaceable with cast structures, none of the developed welded structures is currently applied at regular cargo transportation. One of the causes is related to the fact that they do not ensure the required reliability and fatigue life. Welded structures were poorly optimized in terms of fatigue resistance of welded joints.

In the railways of the USA, Canada, China and Japan three-piece two-axle bogies are mainly used, which are similar to bogie of 18-100 model, with cast load-carrying elements. In West Europe a unified bogie of Y25 type and its numerous modifications with axlebox suspension and with rigid H-shaped welded frame is used (Figure 7). Wide application of welded bogies of Y25 type (1435 mm track, 25 t capacity per axle) is due to high reliability of the structure, as well as low cost of their fabrication and maintenance. New designs of welded FCBs with high operating characteristics are developed, for instance RC25NT bogie (1435 mm track, 25 t capacity) manufactured by ELH Company (Halle, Germany) with frame structure and central spring suspension (Figure 8).

In order to develop a competitive welded solebar and bogie bolster irreplaceable with cast variant of solebar of 18-100 type bogie, the following problems should be solved: first, fatigue resistance and reliability of bogie elements should be improved; secondly, accuracy of solebar fabrication should be increased to eliminate skewing of wheelset axles leading to fast wear of wheels, third, solebar weight and cost should be lowered through application of rolled sheets and welding fabrication technology; fourth, bogie element run between scheduled depot repairs should be in-

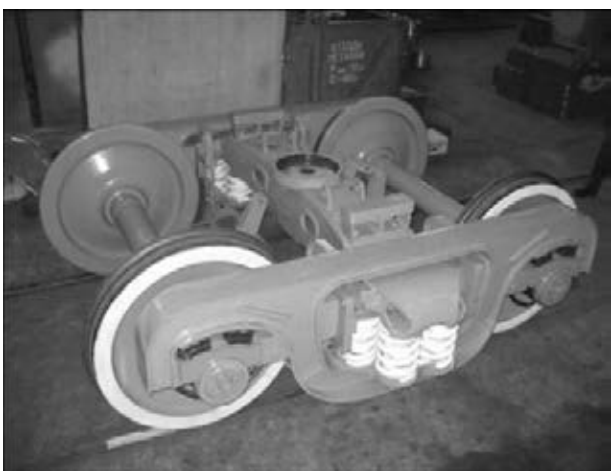

Figure 5. Design of 18-9750 model bogie of freight car of companies «Vagony» and TIV

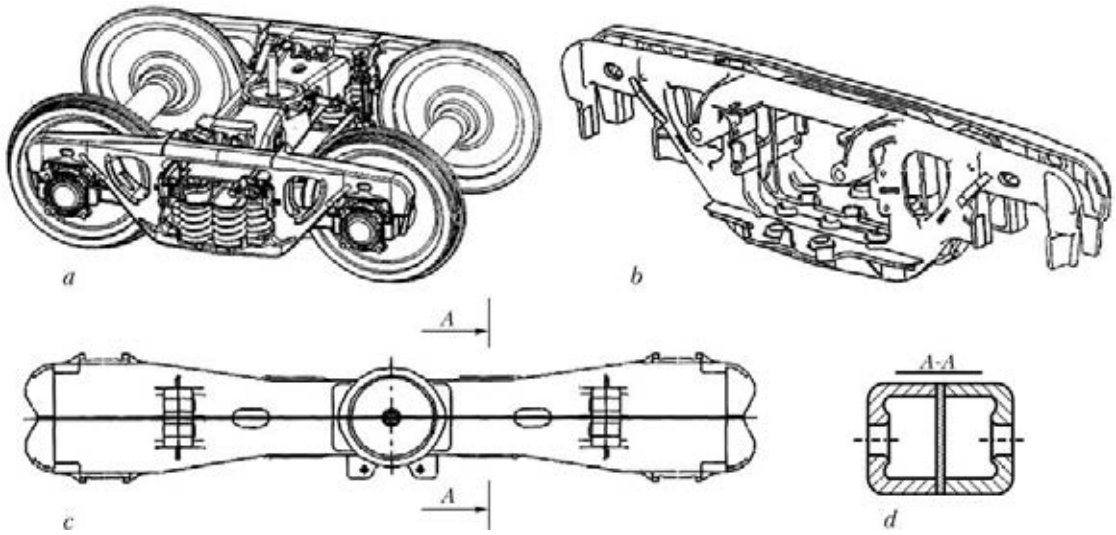

Figure 6. Schematic of bogie of freight car of company «Uralvagonzavod» (*a*), its solebar (*b*), bogie bolster (*c*) and *A*–*A* section of bogie bolster (*d*)

creased. Additional complexity of solving these problems consists in strict limitations in design of welded structures, associated with a large number of unchanged overall dimensions of seats.

Thus, the main objective is ensuring the reliability of welded variant of load-carrying elements of three-piece two-axle bogie, in particular, due to improvement of fatigue resistance and survivability compared to cast structure. In development of all-welded structures, it should be taken into account that in keeping with the norms [11], strength of FCB elements is assessed by working stresses in the main design conditions (I and III).

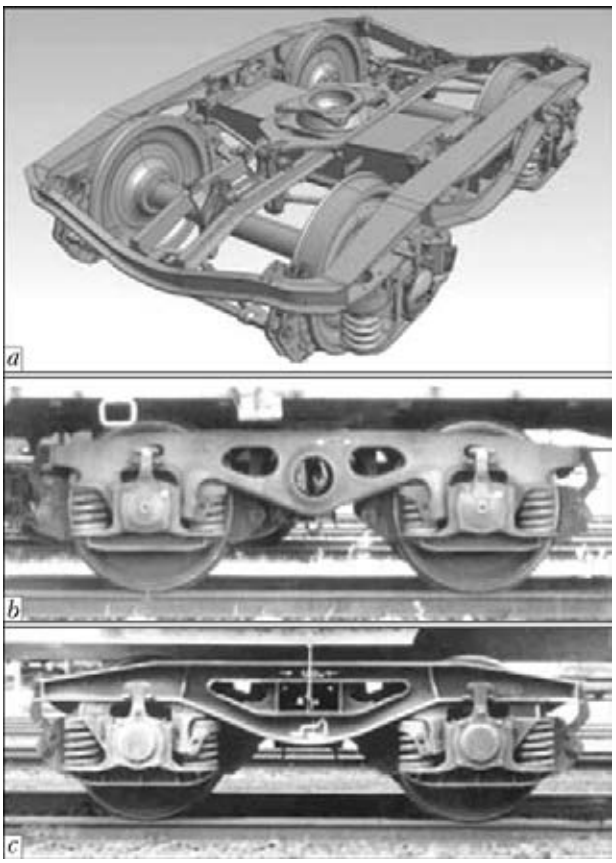

Figure 7. General view of Y25 bogie structure (*a*), cast structure of Y25Cm type bogie (*b*) and welded structure of Y25C bogie (*c*)

In design condition I a relatively rare combination of extreme loads is considered. In this case the main requirement in strength analysis is prevention of residual deformations (damage) in the assembly or part. In operation, condition I corresponds to backup and breakaway of heavy trains at manoeuvring, in particular at automatic shunting from hump yards, and emergency braking in trains at low movement speeds.

In design condition III a relatively frequent combination of medium loads is considered, which is characteristic for normal operation of a car in a moving train. Main requirement in design by this mode is prevention of fatigue fracture of the part assembly. In operation this design condition corresponds to the case of car movement as part of the train along straight and curvilinear track sections and points at allowable speed, at periodical adjusting braking, at periodical medium jerks and jolts, and at normal operation of the car mechanisms and assemblies.

Fatigue resistance of the developed all-welded structures of FCB elements should be calculated

Figure 8. General view of RC25NT bogie welded structure

in keeping with the norms [11] by the coefficient of fatigue resistance for different evaluated zones (base metal and welds) and allowing for the distribution of vertical dynamic factor in the operating speed ranges (load spectrum) [12].

Fatigue resistance coefficient of a structure is evaluated by the formula

$$n = \frac{\sigma_{a,\,N}}{\sigma_{a,\,e}} \geq [n], \qquad (1)$$

where $\sigma_{a,\,N}$ is the fatigue limit (by amplitude) at symmetrical loading cycle at test base of $N_0 = 10^7$ cycles; $\sigma_{a,\,e}$ is the design value of dynamic stress amplitude of a conditional symmetrical cycle, equivalent to real condition of service stresses during part operating life in terms of damaging impact, which is determined based on linear damage accumulation (Palmgren–Miner method); $[n]$ is the allowable minimum value of fatigue resistance coefficient, assumed in keeping with the norms [11], for the newly designed bogie $[n] = 2$.

It is rational to perform strength analysis at loads corresponding to static strength testing and abbreviated accelerated fatigue resistance testing, which are specified by currently valid normative documents [13, 14].

Proceeding from the most recent achievements in the field of determination of welded joint fatigue resistance, it is rational to perform fatigue resistance design of bogie elements also in keeping with IIW recommendations [15] by the condition of fatigue fracture initiation (macrocracks) in different evaluated zones of the structure (welded joint zones), allowing for the specified service load spectrum. This document generalizes a large scope of experimental studies for typical welded joints that allowed determination of the admissible range of nominal stresses at regular loading for each of them:

$$[\Delta\sigma] = \frac{\mathrm{FAT} f_1(R) f_2(N) f_3(\delta) f_4(T)}{\gamma_M}, \qquad (2)$$

where FAT is the joint class or admissible range for a given joint based on $2\cdot10^6$ cycles of regular loading (constant parameters of loading cycle) at $f_1 = f_2 = f_3 = f_4 = \gamma_M = 1$; $f_1(R)$ is the coefficient of the impact of loading cycle asymmetry; $f_2(N)$ is the coefficient allowing for limited fatigue; $f_3(\delta)$ is the correction for adjacent element thickness; $f_4(T)$ is the correction for working temperature of joint operation; γ_M is the safety factor.

In the case of allowing for the load spectrum of 10 regular cycles in keeping with the norms [11] structure fatigue life can be determined from the condition of accumulated damageability not exceeding a unity:

$$\sum_{j=1}^{10} \frac{n_j}{N_j} \leq 1, \qquad (3)$$

where n_j is the number of j-th cycles with range $\Delta\sigma_j$; N_j is the fatigue life limit at regular loading with range $\Delta\sigma_j$ for j-th element of the spectrum:

$$N_j = C \left(\frac{\mathrm{FAT} f_1(R) f_3(\delta)}{\Delta\sigma_j \gamma_M} \right)^m; \qquad (4)$$

$C = 2\cdot10^6$, $m = 3$ at $N < 10^7$ cycles, at $10^7 < N < 10^9$ cycles $C = 1\cdot10^7$ and $m = 22$, or it can be assumed that the amplitude does not change [15].

If $n_j = Pv_j N_{\mathrm{spec}}$, where Pv_j is the fraction of j-th loading in the total loading on the base of N_{spec} cycles, then it follows from (3) that fatigue life limit for the spectrum is

$$[N_{\mathrm{spec}}] = \frac{1}{\sum\limits_{j=1}^{10} \frac{Pv_j}{N_j}}. \qquad (5)$$

Among the normative documents currently in force in Ukraine the most modern approaches to fatigue analysis of steel structure elements, including welded elements, are given in document [16]. According to these approaches, limit admissible cycle number N_j at calculation of steel structure accumulated damageability and at stresses σ_i is determined as follows:

$$N_i = \frac{A_\rho}{\ln \left[\frac{2\sigma_i}{(1 - \rho_i) R_\rho} \right]} - B_\rho, \qquad (6)$$

where R_ρ is the design fatigue limit of the calculated cross-section; A_ρ, B_ρ are the parameters determined from the tables [16]. By design-technological features base metal, welded joints, high-strength bolted connections of elements and assemblies of the structure are divided into 7 groups, allowing for the impact of forces relative to design cross-section. Fatigue limit value R_ρ for element groups is given by the following formula:

$$R_\rho = \frac{2\sigma_{-1}}{2 - D_N(1 + \rho)} \left(1 - 1.63 \frac{S_{\sigma-1}}{\sigma_{-1}} \right). \qquad (7)$$

Values of parameters σ_{-1}, D_N, $S_{\sigma-1}$ in (7) are taken from the tables [16].

As reported by European developers the following standards are the most often used in design of load-carrying welded structures of railway vehicles [17]: TSI standard [18], British standard

prEN 12663-2:2007 [19] and Eurocode 3 standard, Pt 1.9 [20]. TSI specifies standard loads at testing of freight cars, as well as all the types of loads, which are applied to car structures in operation. In keeping with the requirements of prEN 12663, static loads applied to car structure are determined: horizontal and vertical loads, and the most unfavourable combination of horizontal and vertical loads. In calculation of dynamic strength of freight cars, dynamic load is taken in the range of ±30 % of the static one along the vertical, because of vertical loads, in keeping with TSI standard and prEN 12663. In fatigue analysis of car welded joints Eurocode 3 standard, Pt 1.9, is used.

It should be noted that the design and test loads specified by European standards, differ essentially from those accepted in Ukraine, Russia and other CIS countries. This is, primarily, related to railway track condition and operating conditions of railway cars. Therefore, in development of welded structures of load-carrying elements for FCBs it is highly rational to apply, alongside the norms currently in force, also the most recent achievements in the field of dynamics and strength of railway cars, as well as recommendations on welded joint fatigue resistance analysis.

Conclusion

On-going upgrading of freight car fleet determines the high demand for their bogies. As shown by railroad accident statistics, production of cast load-carrying elements of the bogies is characterized by a high degree of probability of internal defect formation and, therefore, by instability of strength values, particularly at cyclic loads. Therefore, development of all-welded load-carrying elements of FCBs, which will be more reliable and irreplaceable with those currently manufactured, is expedient. It should be further noted that fabrication of all-welded variants of bogie load-carrying elements does not require any expensive equipment as in casting production that makes element manufacture more affordable and lowers the dependence of car manufacturers on casting suppliers.

In order to develop a competitive welded solebar and bogie bolster, irreplaceable with the cast variant of the bogie of type 18-100, it is necessary to, first, increase the fatigue resistance of bogie elements; secondly, improve the accuracy of solebar manufacturing to prevent skewing of wheelset axles leading to rapid wearing of wheels; third, lower the weight and cost, and fourth, increase bogie element run between scheduled depot repairs.

Strength analysis of bogie elements should be performed in keeping with the norms currently in force, as well as allowing for the current world concepts, standards, norms and recommendations in the field of railway car dynamics, and methods of welded joint fatigue determination.

1. Sokolov, A.M. (2012) About formation of complex program of R&D on problem of fractures of solebars of freight car bogies. *Byul. Obied. Uch. Soveta OAO «RZhD»*, **3**, 3–11.
2. Pranov, V.A. (2012) *Increase in fatigue life of freight car bogies*: Syn. of Thesis for Cand. of Techn. Sci. Degree. Ekaterinburg.
3. Oganian, E.S. (2013) Conditions of safety service of cast parts of freight car bogies. *Byul. Obied. Uch. Soveta OAO «RZhD»*, **3**, 13–19.
4. Danilenko, S.S. (2004) *Investigation of stress-strain state of solebar of bogie 18-100 taking into account the technological dispersion of geometrical parameters of its section*: Syn. of Thesis for Cand. of Techn. Sci. Degree. Bryansk STU.
5. Monastyrsky, A., Bubnov, V., Kotenko, S. et al. (2012) Fracture of solebar of freight car bogie. Analysis of production technology, ways of defect elimination. *CADmaster*, **5**, 60–65.
6. Volkov, V.A., Chepurnoj, A.D., Bubnov, V.M. et al. *Two-axle bogie for freight car*. Pat. 2275308 Russia. Int. Cl. B61F5/38; B61F5/26; B61F5/12; B61F3/02. Publ. 27.04.2004.
7. Makhnenko, V.I., Garf, E.F., Rimsky, S.T. et al. (2006) Welded freight bogie bolster project. *The Paton Welding J.*, **4**, 2–8.
8. Dejneko, S.Yu., Prikhodko, V.I., Bondar, N.A. et al. *Two-axle bogie of freight car*. Pat. 2246416C2, Russia. Int. Cl. B61F5. Publ. 20.06.2004.
9. *http://*www.nvc-vagon.ru
10. Sharapov, A.A., Goloviznin, B.L., Malykh, N.A. et al. *Bogie of railway car, solebar and bolster of railway car*. Pat. 2373091C2 Russia. Int. Cl. B61F5. Publ. 20.11.2009.
11. (1996) *Standards for calculation and designing of railway car of Railroad Ministry of 1520 mm track (non self-propelled)*. Moscow: GosNIIV-VNIIZhT.
12. Boronenko, Yu.P., Orlova, A.M., Rudakova, E.A. (2005) *Designing of running parts of car*: Manual. Pt 2: Designing of two-axle freight bogies. St.-Petersburg UPS.
13. (2010) *Bolsters and solebar of cast two-axle bogies of freights for 1520 mm track, method of fatigue tests*. Moscow: VNIIZhT-NII vagonostroeniya.
14. (2010) *Bolsters and solebar of cast two-axle freight bogies for 1520 mm track, method of static strength tests*. Moscow: VNIIZhTNII vagonostroeniya.
15. (2006) Recommendations for fatigue design of welded joints and components. *IIW Doc. XIII-1965r14-03/XV-1127r14-03*.
16. *DBN V.2.6-163:2010*: Structures of buildings and constructions. Steel structures. Standards of designing, fabrication and assembly. 2nd ed. Kyiv: Minregionbud Ukrainy.
17. Zivkovic, M.V. (2011) Numerical analysis of welded joints of wagon constructions. *Zavarivanje i Zavarene Konstrukcie*, **3**, 101–106.
18. (2006) *TSI Standard*: Commission Decision of 28 July 2006 concerning the technical specification of interoperability relating to the subsystem rolling stock — freight wagons of the trans-European conventional rail system (notified under document number C(2006)3345).
19. *Pr EN 12663.2:2007*: Railway applications — structural requirements of railway vehicle bodies.
20. *Eurocode 3*: Design of steel structures. Pt. 1.9: Fatigue. Appr. 16.04.2004.

Received 30.07.2013

TECHNOLOGY FOR MANUFACTURE OF GAS-AND-OIL LINE PIPES USING HIGH-FREQUENCY METHOD OF WELDING AT COMPANY «Interpipe NMPP»

Yu.N. ANTIPOV[1], E.V. DMITRENKO[1], A.V. KOVALENKO[1], S.A. GORYANOJ[1], A.A. RYBAKOV[2], S.E. SEMYONOV[2] and T.N. FILIPCHUK[2]

[1]PJSC «Interpipe «Novomoskovsky Pipe Plant»
115 Suchkov Str., 51200, Novomoskovsk, Ukraine. E-mail: info@nmpp.interpipe.biz
[2]E.O. Paton Electric Welding Institute, NASU
11 Bozhenko Str., 03680, Kiev, Ukraine. E-mail: office@paton.kiev.ua

Considered are the technological peculiarities of current production of gas-and-oil line pipes of 159 to 530 mm diameter using high-frequency method of welding at PJSC «Interpipe NMPP». After modernization performed, preparation of welding edges of coiled strip is carried out by milling. Advanced structural-and-technological solutions are used for pipe welding and molding. Local heat treatment of a zone of longitudinal weld is introduced. A section was organized for complex non-destructive testing, including ultrasonic (pipe body and, in addition, weld metal, near-edge zones of welded joint and end section of the pipe), as well as magnetic particles testing of machined edges. Deposition of corrosion-resistant coating on external surface of the pipe is carried out. Information technologies and automated systems are used in regulation of production processes during quality control and tracking of pipes. Applied technology allows manufacturing of gas-and-oil line pipes of medium diameter in a wide range of grade schedule in accordance with the requirements of current domestic and foreign reference documents. High quality and safety of manufactured gas-and-oil line pipes are verified by the documents of authorized certification centers, as well as by the results of performed full-scale tests of pipe specimens before fracture. Pipes of «Interpipe NMPP» production are allowed for application in the systems of main gas-and-oil pipelines in CIS, as well as in far-abroad countries, by authorized accreditation bodies. 5 Ref., 5 Tables, 5 Figures.

Keywords: *gas-and-oil line pipe, medium diameter, production, technology, edge preparation, high-frequency welding, local heat treatment, non-destructive testing, schedule, specification, tests, certification, accreditation*

Production of gas-and-oil line pipes using high-frequency welding was organized at Novomoskovsk Pipe Plant («Interpipe NMPP» company) in 1965. Technological process of production mastered in that period was typical at application of high-frequency (HF) method of welding and lied in feeding of coil of up to 20 t weight, straightening, cutting out of end sections and joining of adjacent strips using butt welding machine, cutting of side edges by circular knifes, roll molding, welding (using induction heating, fusion and upsetting of the edges), removal of flash and division of «endless» pipe for specified lengths. Further, the welded pipes were subjected to 3D thermal flame treatment by normalizing mode, machining of edges, necessary finishing operation, NDT, mechanical and hydraulic tests.

For the last years, the Plant accumulated significant technological experience of production of gas-and-oil line pipes of medium diameter. Till 2005 more than 20 mln t of gas-and-oil line pipes of 159–530 mm diameter were manufactured using HF welding based on specifications and standards of former USSR and then RF, Ukraine and others countries, and they are operated in different systems of main pipelines.

Nevertheless, signs of obsolescence of the plant technology from advanced foreign analogues appeared in the 1990s of the last century under conditions of transfer to market relationships. Pipe production volumes decreased and world marketing of manufactured products became difficult. Some consumers had doubts as for safety of HF-welded pipes due to limited capabilities of accepted system of NDT.

Set of measures for significant technological modernization of production of HF-welded pipes was taken at «Interpipe NMPP» after 2005 in order to expand schedule, provide for the requirements of current world standards, reduce prime cost, further improve quality and safety, and, as a result, competitiveness of the pipe products. Modernizing of technological equipment was carried out considering advanced foreign experience and recommendations of the E.O. Paton Electric Welding Institute. Novel technological equip-

© Yu.N. ANTIPOV, E.V. DMITRENKO, A.V. KOVALENKO, S.A. GORYANOJ, A.A. RYBAKOV, S.E. SEMYONOV and T.N. FILIPCHUK, 2014

ment was delivered by enterprises of Austria, Great Britain, USA, Germany, France, Korea, Holland and Czech Republic.

Sections of a line of 159–530 mm pipe welding mill used for preparation of side edges, molding, welding and removal of external and internal burr were modernized and local heat treatment (LHT) of welded joint was introduced. Areas of current NDT and external corrosion-resistant coating of pipes were organized and automated information system was embedded. Production of inch series pipes of 355.9, 406.4 and 508 mm diameter was mastered and calibration of 530 mm diameter pipes was improved.

This paper considers current state, technological peculiarities, achievements and capabilities of production of HF-welded gas-and-oil line pipes at indicated enterprise.

Milling of the side edges of coil led strip was introduced after modernizing of technological equipment. Edge milling machine provides for cutting of a layer of metal of side edges for up to 10 mm width, which could have technological defects (flashes and cleavages after circular knifes treatment), as well as defects of metallurgical production (tears, laminations, split cracks). Also, treatment of edges by milling completely eliminates structural and geometrical inhomogenieties of the edge surface (plastic collapse, shear, cleavage), which have destabilizing effect on process of further welding.

Edge milling machine allows receiving accurate width of a strip along its whole length with allowable deviation ±0.25 mm, that provides for optimum width along the whole length, and, respectively, rises stability of bringing together of edges in a closed pass of welding stand. This improves weld quality and ensures accuracy of pipe geometry parameters. The edge milling machine is equipped with automatic strip-width gouge providing readings displaying.

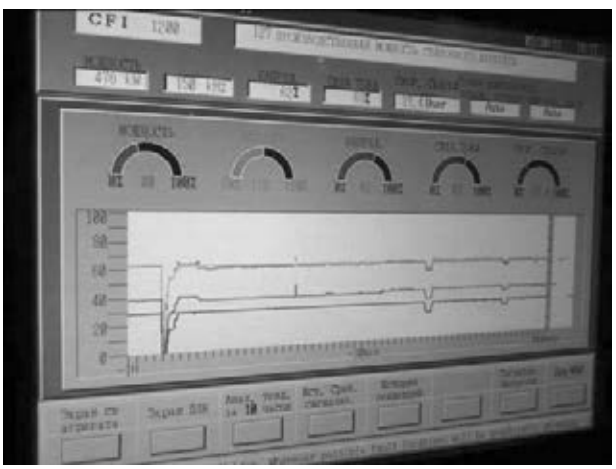

Figure 1. Control of parameters of HF welding of pipes

New welding generator, allowing pipe welding by currents of 150 kHz frequency, was installed instead of earlier applied 10 kHz current source. This permitted process stabilization and performance of welding in accordance with the requirements of foreign standards [1]. In addition, increased current frequency reduces HAZ and decreases depth of current penetration in the part. The generator is equipped with intelligent automatic diagnostics system, having capability of graphic displaying of the main welding process parameters in real-time mode, i.e. power takeoff, voltage, welding speed (Figure 1). Automatic control of the parameters of HF welding process during pipe manufacture is carried out based on control of metal temperature in a zone of edge surface melting using laser and fiber-optic device. Automatic devices allow significantly reducing negative effect of deviations from welding conditions on parameters of mode and weld quality.

Weld constricting five-roll stand is mounted in the welding zone. Such a structure provides for accuracy and stability of pipe geometry parameters due to application of two side, one bottom support and two near-edge rolls in the closed pass. In turn, the accuracy of pipe profile geometry in the welding pass ensures stability of one of the most important parameters of HF welding, namely, edge upsetting, as well as eliminates formation of «edge displacement» defect in pipe billet. The five-roll welding stand is equipped with the trimmers providing quality removal of outside and inside flash.

Installed computer system registers the results of ultrasonic testing of quality of removal of internal flash and thickness of wall in place of its removal in real-time mode (with print-out capability).

Technology of LHT of pipe welded joint at width of heating zone not less than 20 mm was introduced instead of volume one. New automatic medium-frequency induction units (Figure 2) were mounted. Normalizing mode during LHT provides for relieve of residual stresses and re-solidification of microstructure, that determine rise and stability of mechanical properties of the welded joint. Base metal properties in LHT remain virtually the same, technology of production of coiled stock provides its high quality indices.

Equipment of a line for heat treatment of pipe welds is equipped with systems of automatic regulation and control for stabilizing of heating temperature with ±20 °C accuracy, as well as radial tracking of position of welded joint in zone of regulation (±15°).

Indicated above automated systems for control, as well as regulation (stabilizing and regis-

tration) of parameters of industrial processes, based on application of current information technologies, are the integral part of a step system of technological and acceptance control of the pipes existing at the Plant.

Technological inspection includes:

- incoming inspection of coiled steel;
- visual inspection of pipe surface;
- NDT of welded joint integrity and quality of flash removal in a mill line;
- sampling of bend test specimens from start pipes at technological transfers (change of diameter, wall thickness, steel melting);
- continuous and periodic inspection of each step of process of pipe production by workshop and technical control department personnel, respectively.

Acceptance inspection provides for:

- NDT of pipe metal integrity by means of external examination and application of physical methods. New equipment for ultrasonic testing allows inspection of the whole pipe body (Figure 3). Additionally, ultrasonic testing of weld metal and adjacent to it near-edge zones, as well as pipe end sections is carried out. Surface integrity of pipe edges is evaluated by means of magnetic particle testing;
- check of pipe mechanical properties;
- metallographic inspection of welded joint after LHT;
- inspection of geometry parameters of pipe edges and body, including the areas of internal and external flash removal;
- hydraulic testing of pipes.

Automated system used for traceability, accounting of production and control of product quality was implemented. New equipment allows documentation of technological parameters of the pipe production process in reference to number of each pipe. Registration of diameter, wall thickness, steel grade, welding rate, takeoff power and temperature of edges in fusion zone, results of technological ultrasonic testing, temperature of welded joint heat treatment; results of hydraulic tests (pressure, time of soaking, strength evaluation), results of other acceptance tests (mechanical, chemical, non-destructive) is carried out.

Besides, the system provides for automation of the process of receiving of reliable and timely information on state of product production; revealing of mismatch of parameters of technological process, quality of products and taking of effective corrective actions; accumulation and processing of statistical data on quality of metal delivered into production and output products on different criteria; drawing of document for output products and quality certificates in paper and electronic forms.

Figure 2. LHT of pipe welded joint

Corrosion-resistant coatings are deposited over external surface of 114–530 diameter pipes, which had undergone full technological cycle and were declared valid during acceptance. Insulating materials are applied after performance of preliminary certification tests. Depending on customer requirements, corrosion-resistant coatings of different compositions are deposited:

- one-layer epoxy coating of up to 800 μm thickness;
- double-layer coating with application of adhesion layers and polyethylene at total thickness of the coating from 1.8 to 5.0 mm;
- three-layer coating based on ground (epoxy primer), adhesion and polyethylene layers. Total thickness of the coating makes from 2 to 5 mm.

Acceptance of pipes with coatings is carried out considering test performance according to specified technical requirements. Results of coating tests are registered in certificates of pipe quality.

Selection of suppliers of materials for corrosion-resistant coatings is carried out considering performance of wide complex of tests for the purpose of determination of indices of dielectric uniformity, adhesion to steel, area of cathode detachment, transient resistance, cracking resistance, resistant to temperature cycling etc. Pipes having technical characteristics of corrosion-resistance coatings, which correspond to the re-

Figure 3. System for ultrasonic testing of base metal and pipe welded joint

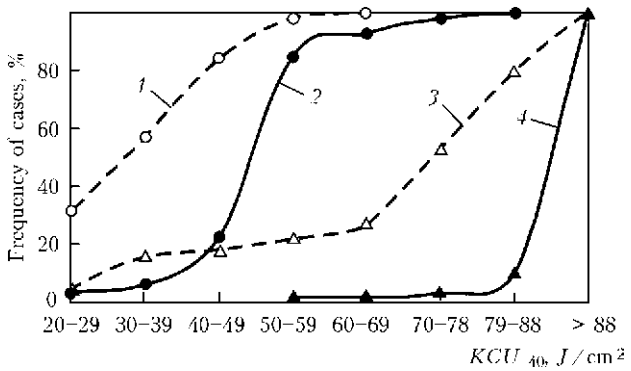

Figure 4. Frequency distribution of impact toughness *KCU* of base (*2*, *4*) and HF-welded joint metal (*1*, *3*) of pipes manufactured from steels with different fraction of carbon and impurities, wt.%: *1*, *2* — 0.18 C; 0.30 Si; 0.015 S; 0.019 P; *3*, *4* — 0.12 C; 0.49 Si; 0.004 S; 0.015 P

quirements of domestic or foreign standards, are manufactured by customer order.

Correspondence of Plant accepted scheme on maintenance and control of product quality to the requirement of current standards (ISO: 9001:2008, DSTU ISO 9001–2009, GOST R ISO 9001–2008, API Q1 specification, ISO 14001:2009) is verified by the documents of authorized certification centers of Ukraine, Germany, USA and RF.

Application of studied technical solutions allowed significantly expanding schedule of produced HF-welded pipes at providing their high service reliability. In recent years, Plant workshop for electric welding of pipes repeatedly manufactured gas-and-oil line pipes of 159–530 mm diameter of different grade schedule, including strength category from L245 to L415 on EN 10208-2, B and from X42 to X70 on API 5L PSL2 (now ANSI/API Spec 5L/ISO 3183:2007), and from K43 to K60 on standards or specifications of RF and Ukraine.

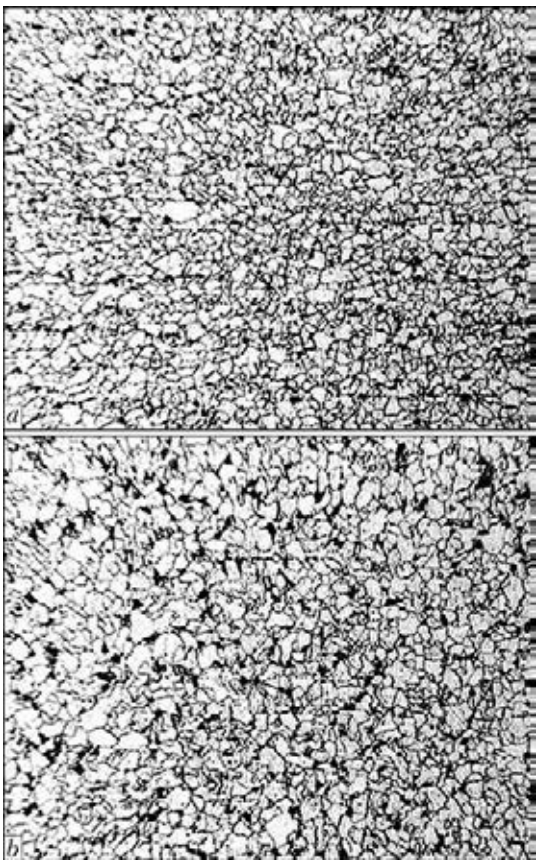

Figure 5. Microstructure (×200) of base (*a*) and welded joint metal (*b*) on K52 strength class pipe

Coiled strip of optimum technical characteristics (chemical composition, mechanical properties, microstructure, geometry, quality, rolled surface) is used for manufacture of gas-and-oil line pipes. Practice of pipe manufacture

Table 1. Results of tensile tests of pipe base metal

Design: pipe symbolic code	Steel grade, strength category, carbon equivalent, manufacturer	Dimension-type, (reference document)	σ_y, MPa	σ_t, MPa	δ_5, %
Standard:					
A1	20, K42, 0.29, OJSC MMK	426 × 6 (TU 14-3-377–99)	359–374 (367) / ≥245	503–508 (506) / ≥412	34–35 (34.5) / ≥23
A2	L360, MB, 0.33, OJSC «Severstal»	323.9 × 8 (EN 10208-2)	360–416 (425) / 360–510	478–537 (507) / ≥460	30–34 (32) / ≥20
Increased strength:					
B1	10G2FBYu, K60, 0.34, OJSC MMK	530 × 10 (GOST R 52079–2003)	537–540 (539) / ≥451	604–620 (612) / ≥590	27–29 (28) / ≥20
B2	X70, P_{cm} = 0.16, OJSC MMK	508 × 8.7 (API 5L PSL2)	493–500 (496.5) / 485–635	618–635 (626) / 570–760	33–34 (33.5) / ≥26
Cold- and corrosion-resistant: B	09GSF, K52, MB, 0.30, OJSC «Severstal»	325 × 9.5 (TU 1303-006.3-593377520–2003)	355–395 (375) / 353–510	620–635 (628) / ≥510	34–36 (35) / ≥20

Note. Here and in Tables 2–5, minimum and maximum values are given in a numerator, the average ones — in the brackets, and standard values of index — in a denominator.

verifies a relevance of application of steel with reduced content of carbon and impurities for improvement of toughness characteristics of base and welded joint metal (Figure 4) [2, 3]. Current technologies of metallurgical production allow obtaining of coiled stock of a necessary strength level with fine-grained structure at reduced content of carbon in steel [4, 5]. In particular, pipes of K52 strength class are manufactured from steel of 17G1S-U type with limitation on content of carbon (not more than 0.14 %). Microstructure of base and welded joint metal of pipe from indicated steel are shown in Figure 5.

Tables 1–4 show, as an example, data on technical characteristics of metal of different types of HF-welded gas-and-oil line pipes of current «Interpipe NMPP» production. Data characterizing technical indices of corrosion-resistant coating are given in Table 5. These examples verify that modernization of the enterprise process provided for the possibility of production of high-quality HF-welded pipes for various service conditions of the main gas-and-oil pipelines.

High working capacity of HF-welded pipes, manufactured on modernized mill, is confirmed by the results of full-scale hydraulic testing. The E.O. Paton Electric Welding Institute carried out the investigations of a branch pipe (using internal pressure), cut out from 530 × 8 mm pipe (17G1S-U steel), in a mode of low-cycle and further static loading up to failure. Tests, at in-

Table 2. Results of tensile and static bending tests of metal of pipe welded joints

Pipe symbolic code	σ_t, MPa	Bending angle, flattening
A1	556–564 (560) / ≥412	180° (no cracks) / Cracks are not allowed
A2	493–536 (514) / ≥460	Flattening (no cracks) / Cracks are not allowed
B1	595–637 (598) / ≥590	180° (no cracks) / Cracks are not allowed
B2	620–638 (629) / 570–760	Flattening (no cracks) / Cracks are not allowed
C	595–637 (598) / ≥510	180° (no cracks) / Cracks are not allowed

Note. Grade of steel and pipe dimension-type in Tables 2–4 correspond to those in Table 1.

Table 3. Results of impact toughness tests of base metal and metal of pipe welded joints

Pipe symbolic code	Impact toughness index	Base metal		Impact toughness of welded joint metal
		Impact toughness	Portion of tough fracture, %	
A1	KCU_{-40}, J/cm^2	60–73 (65) / 34.3	N/D	55–83 (73) / 24.5
A2	KV_0, J	120–298 (209) / ≥40	Same	45–96 (70.5) / ≥40
B1	KCV_0, J/cm^2	205–283 (248) / 24.5	100	53–180 (91) / 24.5
	KCU_{-40}, J/cm^2	217–250 (233) / 34.3	100	25–133 (70) / 24.5
B2	KV_0, J	127–140 (132) / ≥27	N/D	40–44 (41) / ≥27
	KV_{-20}, J	47–57 (53) / ≥27	Same	29–32 (31) / ≥27
C	KCV_{-50}, J/cm^2	135–190 (163) / 59	85–95 (90) / 50	230–250 (240) / 59

Note. Impact tests for pipes of up to 377 mm diameter are carried out on longitudinal specimens.

Table 4. Results of corrosion resistance tests of 09GSF steel pipes (pipe symbolic code C)

Rate of total corrosion, mm/year	Hydrogen cracking, %				Resistance to stress sulfide-induced cracking (at $\sigma_{th}/\sigma_{0.2} \geq 0.7$)
	Base metal		Welded joint metal		
	CLR	*CTR*	*CLR*	*CTR*	
0.327702 / ≤0.5	0/≤6	0/≤3	0/≤6	0/≤3	No fracture / Without fracture of specimens

Note. Here *CLR*, *CTR* are the coefficients of length and thickness of crack, respectively; σ_{th} — the stress during testing of specimens on resistance to sulfide-induced cracking.

Table 5. Results of tests of corrosion-resistant coatings of pipes manufactured on TU U 27.2-05393139-017:2008

Dimension-type, mm	Coating structure, material (manufacturer)	Coating thickness, mm	Dielectric uniformity, kV	Impact strength, J/mm, at T, °C	Adhesion to steel, N/cm, at T, °C
219 × 7.0	Double-layer, Trizolen 200U adhesive (Germany), Alcudia 380N polyethylene (Leuna Euro–Kommerz GmbH)	2.7 / 2.0	No breakdown (at U = 18.5 kV) 5 kV per 1 mm of thickness	8.7/6, −40 ± 3 7.1/5, 20 ± 5 5.2/3, 60 ± 3	150/70, 20 ± 5 80/30, 60 ± 3
530 × 8.0	Three-layer, Corro-Coat EP-F2002 HW epoxy powder (Jotun Powder Coatings, Czech Republic); Coesive L 8.92.8 adhesive (Materie Plastiche Bresciane, Italy), Luxene HDPE 3450 polyethylene (Same)	3.4 / 2.2	No breakdown (at U = 22.5 kV) 5 kV per 1 mm of thickness	17.5/6, −40 ± 3 14.8/5, 20 ± 5 7.4/3, 60 ± 3	166/100, 20 ± 5 115/50, 60 ± 3

itial stage of loading, were carried out on the basis of 10,000 cycles at 0.5–0.9 MPa pressure (loading frequency was 2 cycles per minute). Further, the pipe failed in a course of single loading. Pipe specimens withstood cyclic loadings without formation of cracks and leakages. It was determined in the process of static test that pipe metal yield began at 120 kgf/cm^2 (11.8 MPa) pressure. Failure pressure made 172 kgf/cm^2 (16.9 MPa) that 2.64 times exceeded service pressure. The fracture took place in a middle part of the specimen at 125 mm distance from the pipe weld.

Similar tests were carried out at Central RSI of Shipbuilding Technology (Moscow). Tested 530 × 10 mm size pipe of K60 strength category withstood 10,000 cycles of loading at 90 kgf/cm^2 (8.83 MPa) maximum value of internal hydraulic pressure, that corresponds to the conditions of pipeline continuous duty. Then, the pipe was tested until fracture, which took place along base metal at 223 kgf/cm^2 (21.9 MPa), that created loading at the level of base metal tensile strength.

Specimens of base and welded joint metal of pipes with increased corrosion resistance, manufactured from 09GSF and 13KhFA grade steels, were successfully tested by special organizations, namely Samara Engineering Center (RF) and Research-Tecting center «Kachestvo» (Dnepropetrovsk, Ukraine). At that, resistance to hydrogen and stress sulfide-induced cracking, as well as total corrosion rate, were evaluated. Indicated pipes are used for construction of commercial fields of OJSC TNK and others companies.

Possibility of manufacture of the pipes at the level of requirements of current world standards, providing of high operation capacity and ensuring of the guarantees of pipe quality and reliability served a basis for receiving of accreditation by the enterprise from authorized bodies, including USA, EU and RF, and rights for delivery of their products in the countries of near and far abroad for construction of main gas-and-oil pipelines.

Conclusions

1. Modernizing of technological process allowed «Interpipe NMPP» expanding schedule of HF-welded pipes manufactured for main gas-and-oil pipelines considering the requirements of current standards to their quality. In recent years, the Plant has mastered production and carries out regular deliveries of gas-and-oil line pipes of 159–530 mm diameter of different strength level (with standard ultimate strength up to 588 MPa) and designation (conventional design, cold- and corrosion-resistant) in accordance with the requirements of EU, USA, Ukraine, RF and other countries' standards. The Plant was granted a right by authorized centers of accreditation to delivery of the pipes for systems of main gas-and-oil pipelines, including in the far-abroad countries and RF.

2. Improved guarantees of stability in quality of HF-welded pipes are provided based on application of current technological equipment, complex of technological and acceptance control, as well as implementation of information technologies. Corresponding technical level of product quality management is verified by the documents from authorized international and domestic certification centers.

1. *ANSI/API Spec. 5L/ISO 3183:2007*: Specification for line pipe. Ed. 44. 1 Oct. 2007. Eff. data 1 Oct. 2008.
2. Antipov, Yu.N., Dmitrenko, E.V., Kovalenko, A.A. et al. (2009) Increase in service life of high-frequency welded pipes for main gas-and-oil pipelines. *Problemy Prochnosti*, **5**, 147–153.
3. Rybakov, A.O., Semenov, S.E., Filipchuk, T.M. et al. (2009) Increase of reliability of pipes for main pipelines. In: *Problems of service life and safety of structures, constructions and machines*. Kyiv: PWI, 383–387.
4. Denisov, S.V., Molostov, M.A., Stekanov, P.A. et al. (2008) Development of production technology of coiled stock from low-alloy steels for electric-welded pipes. *Stal*, **7**, 65–68.
5. Morozov, Yu.D., Zikeev, V.N., Filatov, N.V. (2009) Development of coiled steels for electric welded (HFC) gas-and-oil, casing and pump-and-compressor pipes of higher strength, cold and corrosion resistance. *Metallurg*, **10**, 58–60.

Received 06.11.2013

RESISTANCE BUTT WELDING OF CONCRETE REINFORCEMENT IN CONSTRUCTION SITE*

P.N. CHVERTKO, N.D. GORONKOV, N.A. VINOGRADOV, S.M. SAMOTRYASOV and **V.Yu. SYSOEV**
E.O. Paton Electric Welding Institute, NASU
11 Bozhenko Str., 03680, Kiev, Ukraine. E-mail: office@paton.kiev.ua

Considered are the issues of joining of concrete reinforcement bars in construction site using resistance butt welding (RBW). Pilot tests of developed technology for RBW of concrete reinforcement bars and equipment for its realizing were carried out directly in the construction site. It is shown that application of RBW in construction site provides for high economic effectiveness, rises construction efficiency and significantly reduces number of rejected joints. 7 Ref., 8 Figures.

Keywords: *concrete reinforcement bars, mobile complex for resistance butt welding, cast in-situ reinforced concrete, resistance butt welding*

Conditions of current construction of buildings from cast in-situ reinforced concrete require elongation of the reinforcement bars directly in construction site. This, first of all, is caused by application of reinforced concrete structures of more than 12 m (maximum length of reinforcement manufactured by metallurgical plants) and efficient use of metal stock. Different methods of welding of the reinforcement, mainly arc ones [1], are widely used in building and repair of reinforced concrete structures and constructions. Manual and semi-automatic arc welding as well as puddle-arc one found the widest distribution among these methods.

It should be noted that resistance butt welding (RBW) is widely used in addition to indicated methods at the plants and concerns, which manufacture precast reinforced structures. Today, this process is one of the leading methods for manufacture of reinforcement butt joints using technology of low-waste processing of bars under stationary conditions.

RBW process is characterized by high stable quality of welded joints and high efficiency. Application of RBW allows making full-strength joints, in comparison with base metal, that significantly increases safety and service life of reinforced concrete structures and provides for high efficiency. The welding process takes place in automatic mode, combining assembly and welding operations in one cycle, and requires no auxiliary consumables (electrodes, welding wire, fluxes, gases etc.) [2]. At that, welders' qualification has no special requirements.

Mechanical tests of the welded joints showed that they completely fulfil the requirements of DSTU 3760:2006 and GOST 10922–90 [3, 4]. A

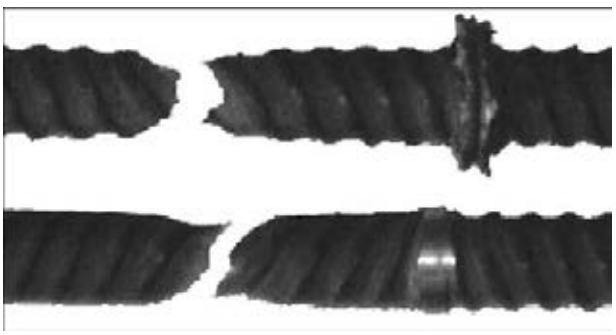

Figure 1. RBW joints of reinforcement after tensile testing

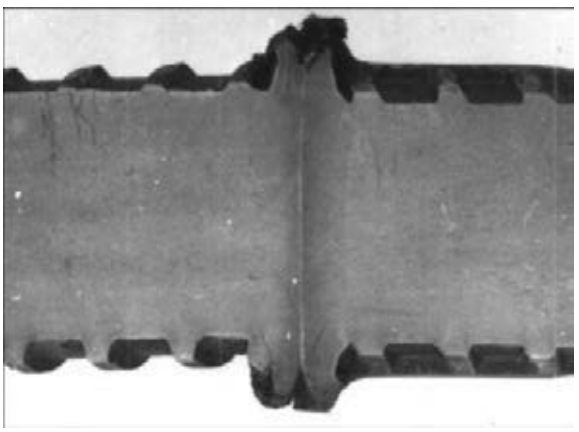

Figure 2. Macrosection of HAZ metal of RBW joint on reinforcement bar of A500 class

*Based on materials of work made in scope of program «Problems of life and safety of service of structures, constructions and machines». Kyiv: PWI, 2012, p. 468–472.

© P.N. CHVERTKO, N.D. GORONKOV, N.A. VINOGRADOV, S.M. SAMOTRYASOV and V.Yu. SYSOEV, 2014

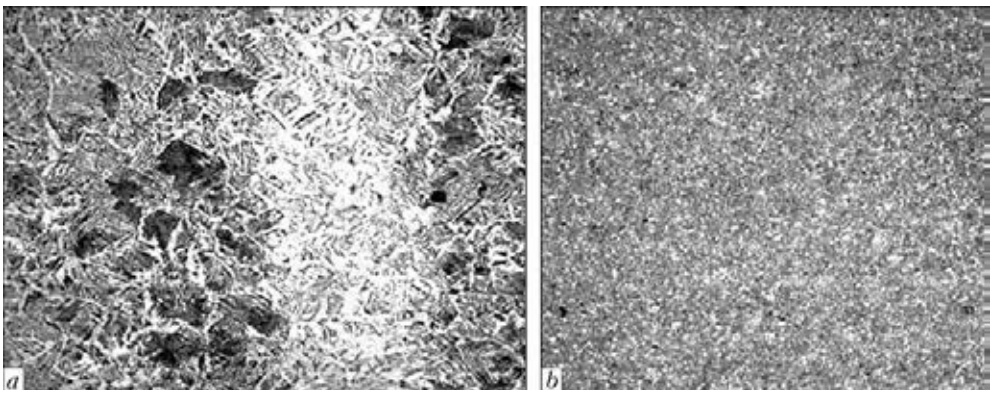

Figure 3. Microstructure (×100) of RBW joint on reinforcement bar of A500 class (*a*) and base metal (*b*)

failure takes place out of the welding zone in specimen tension (Figure 1).

Using of RBW of reinforcement provides for uniform heating of metal of zone of further deformation during upsetting (formation of welded joint). HAZ has small extension [5, 6].

Figure 2 shows a macrosection of HAZ metal reinforcement welded joint made using RBW, and Figure 3 depicts the microsections of RBW joint and base metal of the reinforcement.

Aim of this work lies in development of a line for RBW of reinforcement in construction site.

Present experience of development of technologies and special equipment for RBW of rails and pipes in field conditions allowed using this process for joining of concrete reinforcement bars under semi-stationary conditions directly in construction site. The E.O. Paton Electric Welding Institute developed the technologies of RBW of concrete reinforcement bars and pilot sample of mobile complex for realizing of these technologies directly in construction site. Modernized machine K813, earlier developed at the E.O. Paton Electric Welding Institute, was used in pilot samples of the complex. This development can be widely used in construction of commercial and residential buildings, bridges, trestleworks and other objects. Performed metallographic investigations

Figure 4. Structures of reinforcement cases of Podolsky bridge crossing over Dnieper River (*a*), bearers of VIP-sector of NSC «Olimpijsky» (*b*) and trestlework of terminal D of Borispol airport (*c*) (Kiev)

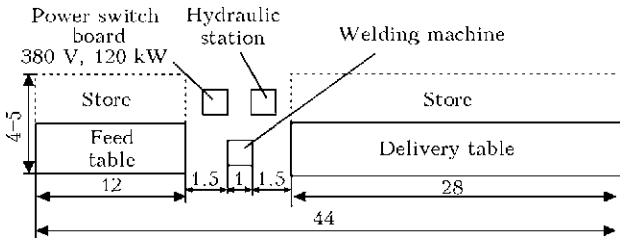

Figure 5. Scheme of line for welding of concrete reinforcement bars in construction site

Figure 6. Suspension RBW machine K813 adjusted for reinforcement joinig in construction site

and mechanical tests of reference industrial specimens showed that quality of the welded joints completely correspond to the requirements of acting reference documents [3, 4].

Requirements to special-purpose equipment are manly determined by the conditions of its operation. The equipment should be mobile, compact, have minimum possible electric capacity and maximum protection from environment. Application of mobile resistance butt machines during assembly is sufficiently difficult considering the complex structures of reinforcement cages of bridge crossings, trestleworks etc. (Figure 4). However, development of special mobile equipment for welding of reinforcement continues at present time.

A technological process for production of long reinforcement in construction site is developed in addition to the creation of such equipment. Prototypes of sites and lines for performance of indicated works were tested and manufactured. Figure 5 shows a scheme of typical line. Different variants of positioning of auxiliary equipment are

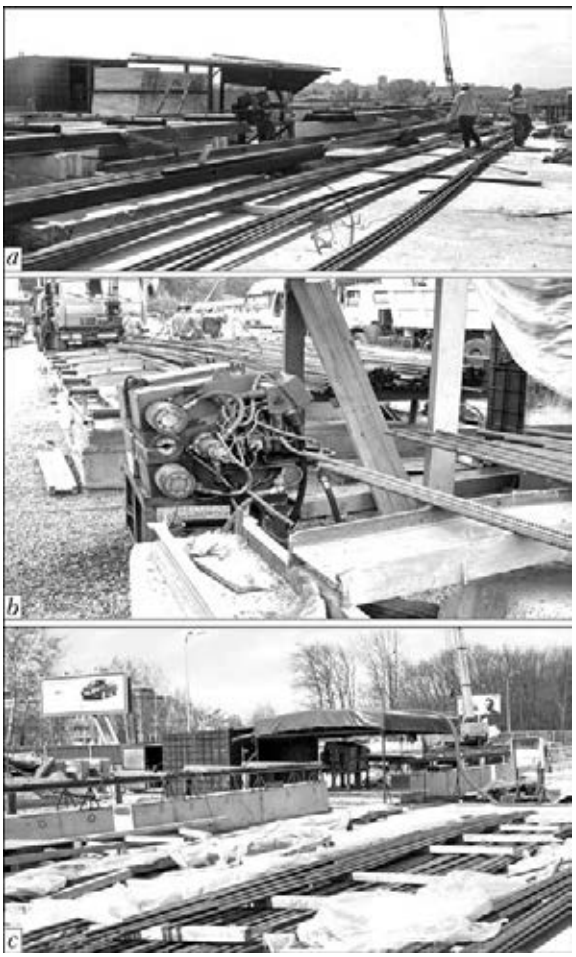

Figure 7. Prototypes of line for reinforcement welding in construction site (*a–c* — same as in Figure 4)

Figure 8. Objects and construction sites, where pilot tests of technology and prototypes of equipment were carried out (*a–c* — same as in Figure 4)

possible in the scheme depending on production conditions.

Since RBW methods received the widest distribution, all the experiments were carried out using modernized welding machine K813 (Figure 6) as base equipment.

The results of pilot tests of prototypes of reinforcement welding lines are shown in Figure 7.

Figure 8 shows the objects and construction sites, where pilot tests of technology and prototypes of equipment were carried out.

Conclusions

1. Quality of arc-welded joints on reinforcement bars depends, to significant extent, on welder qualification and conditions of storage of auxiliary consumables. Process efficiency is low, time of welding of one joint makes approximately 30 min.

2. RBW is carried out in automatic mode and requires application of no auxiliary welding consumables. At that, welders' qualification has no effect on quality of welded joints. Process efficiency is sufficiently high, time of welding of one joint does not exceed 1 min.

3. Application of RBW in construction site in the case of large number of welded joints (for example, hundred thousands to millions of welded joints are made at one bridge crossing) provides for high economic effectiveness, increases efficiency of construction and significantly reduces number of rejected joints.

4. Results of carried out pilot tests of the developed technology for RBW of concrete reinforcement bars and equipment for its realizing directly in construction site indicate the prospects of further development of given direction.

1. Brodsky, A.Ya. (1961) *Welding of reinforced concrete structures*. Moscow: Gosstrojizdat.
2. Kuchuk-Yatsenko, S.I. (1992) *Flash-butt welding*. Kiev: Naukova Dumka.
3. (2007) *DSTU 3760:2006*: Reinforcing bars for reinforced concrete structures. General specifications. Kyiv: Derzhspozhyvstandart.
4. (1990) *GOST 10922–90*: Reinforcing and embedded welded products, welded joints of reinforcing and embedded products of concrete structures. General specifications. Introd. 01.01.91. Moscow: Standart.
5. Chvertko, P.N. (2010) Flash-butt welding of reinforcement bars of A400S–A600S classes in construction of structures of monolithic reinforced concrete. *The Paton Welding J.*, **8**, 25–28.
6. Kugushin, A.A., Uzlov, I.G., Kalmykov, V.V. et al. (1986) *High-strength reinforcing steel*. Moscow: Metallurgiya.
7. Degtyaryov, I.A. (1965) *Welding in production and assembly of reinforcing structures*. Moscow: Energiya.

Received 21.01.2014

REASONS OF STRESS CORROSION FAILURE OF ERECTION GIRTH JOINT OF MAIN GAS PIPELINE

A.A. RYBAKOV[1], **L.V. GONCHARENKO**[1], **T.N. FILIPCHUK**[1], **I.V. LOKHMAN**[2] and **I.Z. BURAK**[2]
[1]E.O. Paton Electric Welding Institute, NASU
11 Bozhenko Str., 03680, Kiev, Ukraine. E-mail: office@paton.kiev.ua
[2]PJSC «Ukrtransgaz»
9/1 Klovsky Spusk, 01021, Kiev, Ukraine. E-mail: press@utg.ua

Considered are some issues of stress corrosion failure of metal of main gas pipeline under operation. It is shown that, except for conventional orientation of stress corrosion cracks in longitudinal direction, the defects of such a type can propagate in transverse direction relatively to axis of the gas pipeline. Found transverse stress corrosion cracks, including ones passing through the whole thickness of the pipe wall, were formed in a zone of girth weld, joining 1420 mm diameter pipes of K60 strength class. Defective zone of 800 mm length was located from both sides of the weld and propagated at approximately 60 mm width from fusion line. Failure surface in zone of defects has specific step nature as a result of coalescence of finer semi-elliptical cracks, nucleated in different planes being displaced relatively to each other. The cracks are mainly characterized by rounded tips, that is typical for stress corrosion defects, formed as a result of anode metal dissolution. Failure of girth welded joint of the pipeline, except for corrosion factors, was promoted, to significant extent, by additional stresses typical for process of pipe assembly during performance of «tie-in». Information of this paper can be used during performance of diagnostic operations on main pipelines. 7 Ref., 1 Table, 9 Figures.

Keywords: *stress corrosion failure, main gas pipeline, crack orientation, welded pipes, strength class, girth welded joint, reasons of formation*

Today, stress corrosion cracking (SCC) of metal is one of the main and most frequent reasons of failure of main pipelines. Damages of such a type are the cracks formed on external surface of the pipelines in areas with failure of insulation coating under effect of corrosion-active media and stress-strain factor under conditions of cathode polarization.

Consequences of failure of the gas pipelines due to SCC (SCC-failure) are sufficiently impressive. Figure 1 shows, as an example, the trench and fragments of 820 mm diameter pipeline after SCC-failure spread at 40–50 m.

Main external sign, used for determination of origin of cracks due to SCC (SC-cracks), is presence of colonies of cracks, oriented as a rule in longitudinal direction, on the external surface of the pipes. Work [1] studied different cases of the stress corrosion damages of main pipelines and preferred development of SC-cracks in the longitudinal direction was underlined, however, a possibility of curving of their orientation due to bend or shrinkage of gas pipeline (Figure 2) is noted. SC-cracks are found in a base metal as well as in a zone of pipeline joints welded at plant. In the most cases, they are detected in low part of the pipe section, close to longitudinal welds, including in a fusion line.

As is well-known, initial stage of stress corrosion damaging lies in formation of a corrosion pitting, which further transforms in the semi-elliptical cracks [2–4]. Conditions for joining (coa-

Figure 1. Stress corrosion failure of main gas pipeline of 820 mm diameter (*a*) and fragments of failed pipes (*b*)

© A.A. RYBAKOV, L.V. GONCHARENKO, T.N. FILIPCHUK, I.V. LOKHMAN and I.Z. BURAK, 2014

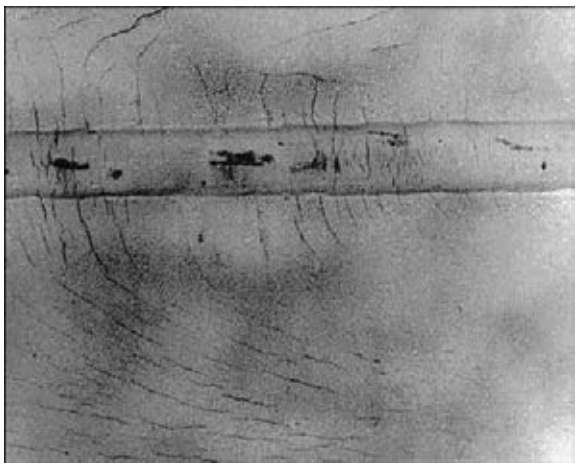

Figure 2. Effect of stress distribution in pipe metal on character of location of SC-cracks [1]

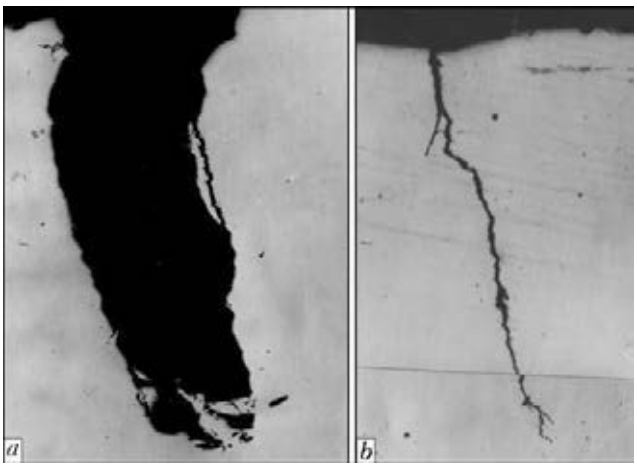

Figure 3. SC-cracks in metal of gas line pipe formed as a result of anode dissolution (a — ×20) and hydrogen cracking (b — ×100)

lescence) of neighbor, closely located cracks, formation of main crack and further failure of the gas pipeline are created in course of defect development.

In accordance to current representations, SCC can propagate on two mechanisms, namely local anode dissolution and hydrogen cracking [4–7]. If the first mechanism is realized, electro-chemical process is localized on the surface of metal and its intensive dissolution takes place in a crack tip. Such cracks, as a rule, are characterized by wider opening, presence of corrosion deposits and their tip has blunt form (Figure 3, *a*). In the second case, diffusion of hydrogen in a metal lattice is performed under effect of stresses and corrosion media. More acute tip, transcrystalline nature of propagation and some splitting (Figure 3, *b*) are typical for the cracks of this type.

Several accident of the gas pipelines, caused by stress corrosion defects, took place in Ukraine. Figure 4 shows appearance and fracture of the specimens with SC-cracks, cut out from the pipes of «Urengoy–Pomary–Uzhgorod» gas pipeline, failed in May, 2007. Similar failures on this gas pipeline were registered in May 2003 and in December 2007. In all described cases, SC-cracks and failures of gas pipeline were also oriented in longitudinal direction.

Local gas leakage and its ignition was detected during operation of main gas pipeline «Progress». Series of the through-wall defects was found in a zone of girth welded joints during test drilling of this section of gas pipeline. The girth weld in defective section was made by «tie-in» and it joints double-weld 1420 mm diameter pipe with 15.7 mm wall thickness of K60 strength class, manufactured at Khartsyzk Pipe Plant, to single-weld pipe of the same diameter with 15.4 mm wall thickness and X70 category of foreign delivery (Figure 5). Metal of both pipes was of similar chemical composition (the Table) and me-

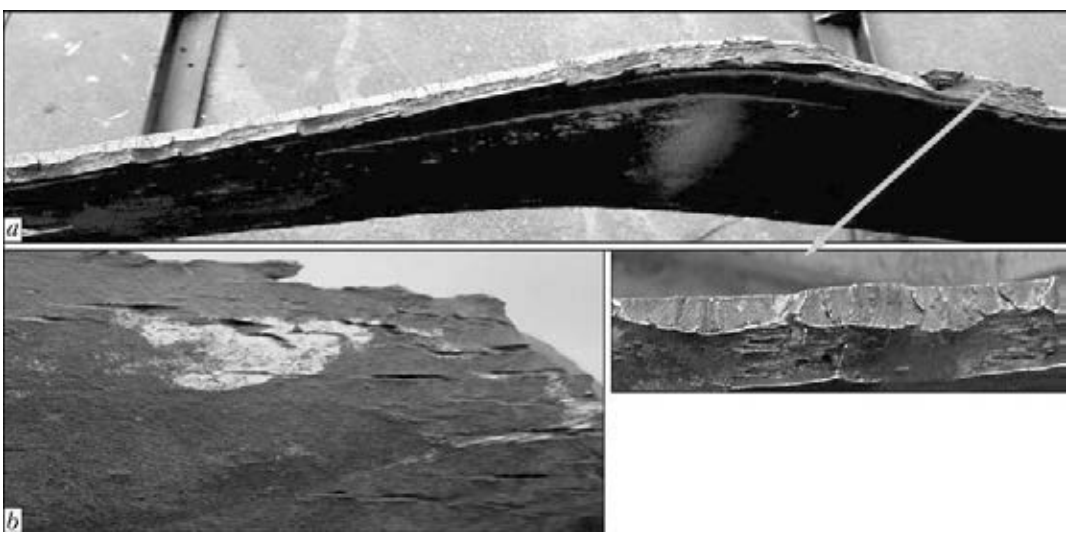

Figure 4. Fragments of failure of 1420 mm diameter gas pipeline with SC-cracks: a — fracture of specimen with crack of 470 mm length and 6.8 mm depth; b — colony of transverse macrocracks in zone of failure on pipe metal surface

chanical properties. It can be assumed based on this that role of metallurgical factor in formation of these SC-cracks is minimum.

The pipeline in failure section was covered by strip polymeric insulation, which was damaged in the place of defect location.

Damage zone with crack-like defects (through-wall and surface ones) was located across the pipe axis and along the girth welded joint at around 800 mm length from both sides of the weld (Figure 6). Area of location of defective section in the girth joint on a route corresponded to 5–7 h of conventional dial. Width of the section with cracks, starting from the fusion line in direction of the base metal, made around 60 mm from each side of the weld.

Two different zones can be clearly observed on fracture of through-wall cracks after their opening, namely zone of defect formation from the side of external pipe surface, and zone of the final rupture on its internal side. Figure 7 shows fractures of the through-wall cracks in different sections. Failure surface in the crack zone has specific step nature, typical for defect, formed as a result of coalescence of smaller semi-elliptical cracks, nucleated in different, displaced relatively to each other, planes. Corrosion deposits are observed on the surface of cracks. The metal

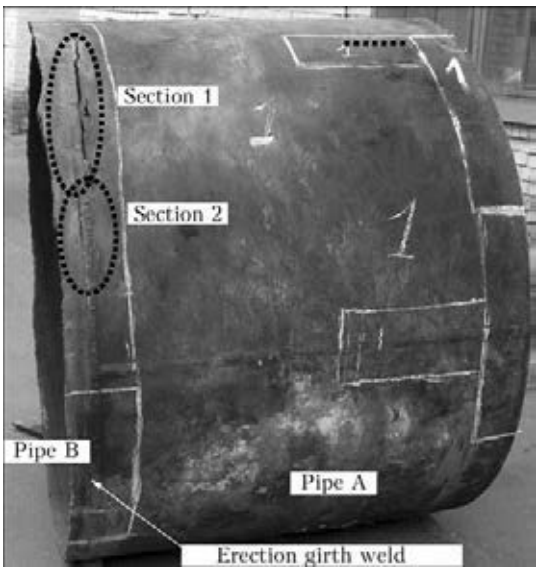

Figure 5. General appearance of failed erection girth joint and sections with maximum accumulation of cracks

in the zone of final rupture failures on tough mechanism.

External surface of both pipes nearby girth weld was damaged by relatively shallow corrosion spots and pitts that verify information about damage of insulation coating.

Multiple cracks of different depth, namely from surface ones to those passing through significant part of the wall thickness (Figure 8, *a*,

Chemical composition of pipe base metal, wt.%

Place of sampling	C	Mn	Si	S	P	Al	Ni	Mo	Ti	V	Nb
Pipe A	0.101	1.45	0.272	0.004	0.012	0.031	0.04	0.03	0.004	0.06	0.027
Pipe B	0.119	1.48	0.357	0.003	0.016	0.034	0.05	0.03	0.005	<0.02	0.028

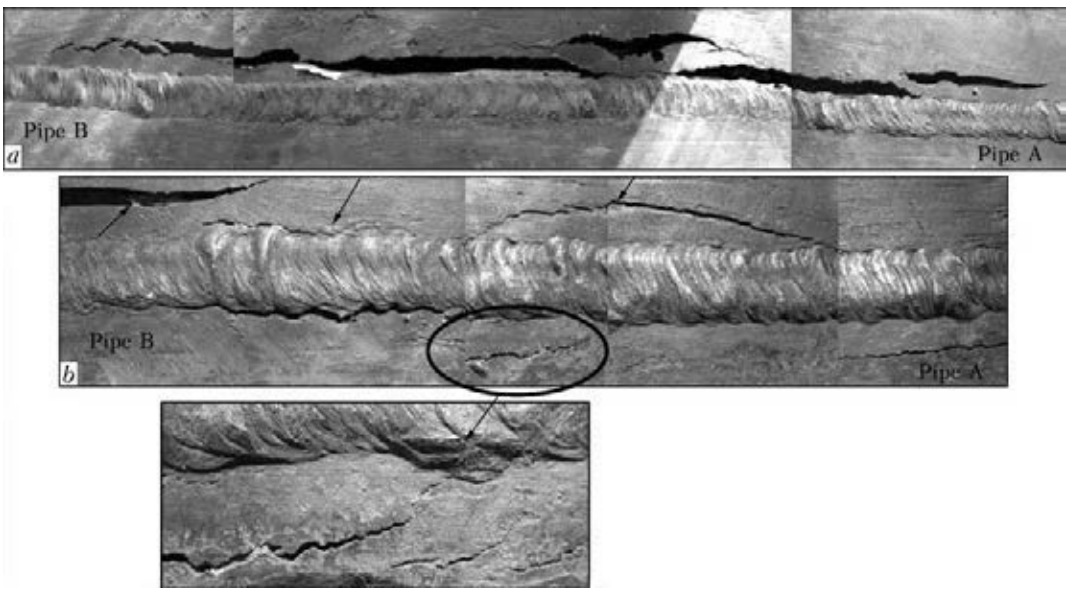

Figure 6. Sections of erection girth joint (see Figure 5) with maximum accumulation of cracks (arrows show crack location): *a*, *b* — sections 1 and 2, respectively

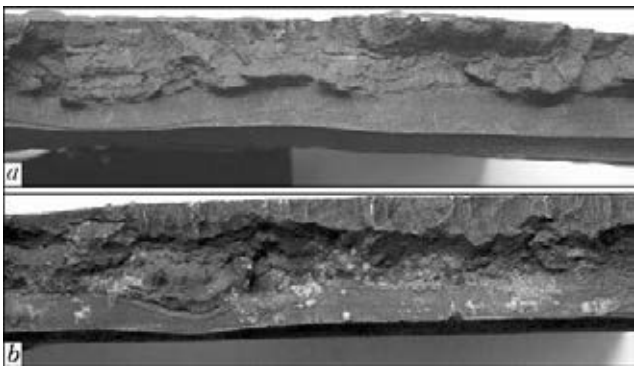

Figure 7. Nature of failure surface (through-wall crack)

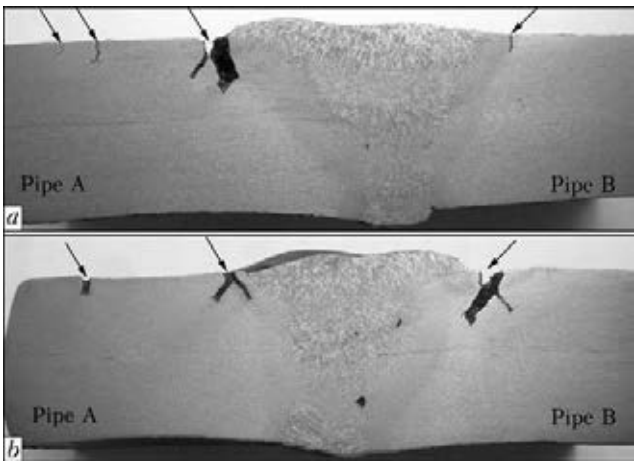

Figure 8. Transverse macrosections of girth welded joint in damage zone (location of cracks indicated by arrows)

b) were registered in the metal of damaged zone of both pipes, as was shown by investigations of macro- and microsections. The cracks have relatively wide opening with rounded tips (see Figure 3, *a*). In the most cases, they are located along the girth weld in a plane normal to pipe generatrix or at around 45°.

Thus, the investigated defective section includes all the signs typical for SCC-failure of gas pipeline metal, i.e. presence of corrosion damages on the external surface of pipe metal, colonies of semi-elliptical cracks of different length and mainly with rounded tips and corrosion deposits, and step nature of fracture of the main cracks, giving evidence of process of coalescence of separate defects etc.

Girth weld of the studied joint was made by manual metal arc welding with some (maximum up to 2 mm) displacement of pipe edges in radial direction, that does not exceed a limit set by SNiP III-42–80 (not more than 3 mm). The girth weld from internal side of the pipe was parformed with significant lack of penetration of root layer up to 3 mm (it is well-known that no lack of

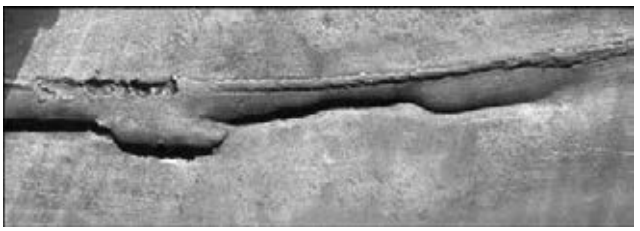

Figure 9. Internal surface of the pipe in damage zone

penetration of root part of erection weld in pipeline of 1000 mm diameter and more is allowed). At that, presence of indicated defects, in this case, was not exactly the reason of girth weld fracture.

It can be assumed that SCC-failure of girth welded joint of the gas pipeline, besides the corrosion factors, was promoted, to significant extent, by additional stresses, typical for process of pipe assembly during «tie-in» performance. It is indirectly verified by significant plastic strain of the metal in formation of through-wall defects, which can be seen in Figure 9 showing internal surface of the pipe in defective section.

Thus, the case was considered when SCC of the girth erection joint became the reason of main gas pipeline failure. Difference of this failure from the earlier investigated lies in SC-crack development in transverse direction relatively to the pipe axis.

In the authors' opinion, this information will be useful for the specialists working in oil-gas field during performance of diagnostic operations on the main gas pipelines.

1. (2006) *Stress corrosion cracking of pipes of main pipelines*: Atlas. Ed. by A.B. Arabej, Z. Knoshinsky. Moscow: Nauka.
2. Sutcliffe, J.M., Fessler, R.R., Boyd, W.K. et al. (1972) Stress corrosion cracking of carbon steel in carbonate solution. *Corros. NASE*, 28(**8**), 313–317.
3. Polyakov, S.G., Rybakov, A.A., Bekker, M.V. et al. (2004) Peculiarities of stress corrosion cracking of main pipelines. *Fiz.-Khimich. Mekhanika Materialov*, **4**, 376–380.
4. Chviruk, V.P., Polyakov, S.G., Gerasimenko, Yu.S. (2007) *Electrochemical monitoring of men-caused media*. Kyiv: Akademperiodika.
5. Kryzhanivsky, E.I., Nykyforchyn, G.M. (2011) *Corrosion-hydrogen degradation of oil-and-gas pipelines and its prevention*: Manual. Vol. 1: Principles of evaluation of pipeline degradation. Ed. by V.V. Panasyuk. Ivano-Frankivsk: Iv.-Fr. NTUNG.
6. Eadie, R.L., Szklarz, R.E., Sutherby, R.L. (2005) Corrosion fatigue and near-neutral pH stress corrosion cracking of hydrogen sulfide. *Corrosion*, 61(**2**), 167–173.
7. Liu, Z.Y., Li, X.G., Du, C.W. et al. (2008) Stress corrosion cracking behavior of X70 pipe steel in an acidic soil environment. *Corrosion Sci.*, 50(**8**), 2151–2257.

Received 08.11.2013